

CMOS Sensors and Polarimetric Studies on the Sun

Von der Fakultät für Elektrotechnik, Informationstechnik, Physik
der Technischen Universität Carolo-Wilhelmina zu Braunschweig

zur Erlangung des Grades eines Doktors
der Naturwissenschaften (Dr. rer. nat.)

genehmigte Dissertation

von Kamal Sant

aus Topri, Indien

eingereicht am 03.08.2022

Disputation am 28.09.2022

1. Referent: Prof. Dr. Sami K. Solanki
2. Referent: Prof. Dr. Karl-Heinz Glaßmeier

Druckjahr: 2022

Abstract

Imaging spectropolarimetry is the measurement of the intensity of light as a function of position, wavelength and polarisation. It allows utilising most of the information carried by light. It is, therefore, the optimal remote sensing technique for solar astronomy as it allows to derive information about the stratification of temperature, velocity and the vector magnetic field in the solar atmosphere.

The complex and highly dynamic magnetic field configuration at the smallest spatial scales plays a vital role in the understanding of the global magnetic properties of the Sun. These structures can be resolved in principle with the newest generation of solar telescopes, but the challenge here is to overcome the image blurring caused by atmospheric seeing. The combination of adaptive optics and post-factum numerical reconstruction techniques is very successful in that respect for pure imaging observations. But an application to spectropolarimetry poses additional challenges, one of which being the non-availability of science-grade electronic image sensors that simultaneously fulfil the requirement for a large number of pixels (5-50 Megapixel), frame rates of order 100 Hz, and the fidelity required for precision polarimetry.

The presented work studies various response irregularities of fast, large-format active pixel sensors for machine vision applications and how they can be calibrated to meet demanding scientific requirements. A generic test bench for sensor characterisation was developed, calibration schemes tailored for three different sensors, used in various instrumentation projects at Max-Planck-Institute for Solar System Research (MPS), are presented. It is demonstrated that non-linearities as large as a few per cent can be suppressed to a level well below one per cent, suitable for spectropolarimetry with a precision of 10^{-3} .

A study of the general properties of sunspots is presented as an example case of the use of solar polarimetry in studying the solar atmosphere. Although the data gathered is not from the calibrated cameras, it shows the usability of polarimetry, the need for high-speed CMOS sensors, and the designed calibration scheme.

Sunspots are a very active field of research for solar spectropolarimetry, and many aspects of the structure of sunspots are still not understood. For example, it is unclear why there is such a sharp boundary between the dark umbra and the brighter penumbra within sunspots. It has been reported that this boundary occurs at a canonical value of the strength of the vertical magnetic field, which does not depend on the size of the spot. However, it is still an open question whether this critical field strength is indeed responsible for the onset of magneto-convection in the penumbra.

Here, we use spectropolarimetric inversions of sunspots observed with Hinode to critically reassess the properties of the umbra-penumbra boundary and the outer boundary of the penumbra. We derive azimuthal averages of various observables along these boundaries for spots of different sizes and at different optical depths. In addition, it is not yet clear how sunspot structure varies between spots of different sizes. We address this by computing azimuthally averaged radial profiles of various observables for sunspots of different sizes.

We can confirm previous observations that the azimuthally averaged vertical magnetic field assumes a constant value at the umbra-penumbra boundary. However, this is only the case at the central node of the inversion ($\log \tau = -0.9$). We find that the strength of the magnetic field increases with spot size at the top node of the inversion. Similarly, the dependence of the averaged temperature on the spot size changes across the atmosphere. This is probably due to the changing appearance of the penumbral filaments at the different atmospheric layers.

The radial profiles show the expected dependence on spot size in the umbra and the inner penumbra. Larger spots are cooler and exhibit stronger magnetic fields than smaller ones. However, there is no significant dependence of the radial profiles on spot size in the outer penumbra. This resemblance between spots of different sizes is particularly strong for the Evershed flow. It supports previous results that penumbral filaments are remarkably uniform between spots of different sizes.

Zusammenfassung

Bildgebende Spektropolarimetrie misst die Intensität von Licht als Funktion von Position im Bildfeld, Wellenlänge und Polarisationszustand. Dies erlaubt es fast den gesamten Informationsgehalt von Licht zugänglich zu machen und ist die Methode der Wahl für astronomische Fernerkundung, insbesondere in der Sonnenbeobachtung, da so Informationen über die Schichtung von Temperatur, Geschwindigkeit sowie Richtung und Stärke des Magnetfelds in der Sonnenatmosphäre gewonnen werden können.

Kleinskalige, hochdynamische Magnetfelder spielen eine Schlüsselrolle für das Verständnis der globalen magnetischen Aktivität der Sonne. Diese Strukturen können mit den aktuellen Sonnentelaskopen im Prinzip aufgelöst werden, allerdings muss hierzu der störende Einfluss der Erdatmosphäre, das Seeing, überwunden werden. Hier werden für rein bildgebende Anwendungen mit dem kombinierten Einsatz von adaptiver Optik und nachträglichen numerischen Bildrekonstruktionsverfahren ausgezeichnete Ergebnisse erzielt. Aber für eine direkte Anwendung auf spektropolarimetrische Messungen besteht eine der zusätzlichen Schwierigkeiten darin, dass Kameras, welche gleichzeitig die Anforderungen an eine hohe Auflösung (5-50 Megapixel), hohe Bildraten im Bereich von 100 Hz, und die für Präzisionspolarimetrie notwendige Wiedergabetreue erfüllen, praktisch nicht erhältlich sind.

Die vorgelegte Arbeit beschäftigt sich mit der Frage, wie Unregelmäßigkeiten im Antwortverhalten von großformatigen und schnellen Active-Pixel Sensoren, wie sie typischerweise für maschinelle Bilderfassung eingesetzt werden, charakterisiert und so kalibriert werden können, dass sie hohen wissenschaftlichen Anforderungen genügen. Im Rahmen der Arbeit wurde ein Teststand für Sensorkalibration entworfen und aufgebaut. Es werden Kalibrationsprozeduren vorgestellt, die auf drei Bildsensoren zugeschnitten sind, welche am Max-Planck-Institut für Sonnensystemforschung für verschiedene Instrumente eingesetzt werden. Es wird gezeigt, dass durch diese Kalibration die Nicht-Linearität der Sensoren von einigen Prozent auf weit unter ein Prozent reduziert werden kann, was polarimetrische Messungen mit einer Präzision im Bereich von 10^{-3} ermöglicht.

Als Beispiel für die Anwendung von Spektropolarimetrie wird hier eine Studie über Sonnenflecken vorgestellt. Es wurden zwar nicht die im Rahmen dieser Arbeit kalibrierten Kameras verwendet, trotzdem zeigt die Studie den Nutzen von Polarimetrie auf sowie den Bedarf für extrem schnelle CMOS-Kameras und für das entwickelte Kalibrationsschema.

Die Erforschung von Sonnenflecken ist ein sehr aktives Forschungsgebiet für Spektropolarimetrie. Viele Aspekte der Struktur von Sonnenflecken sind noch nicht verstanden. Zum Beispiel ist es noch unklar, warum es einen so scharfen Übergang zwischen der Umbra und der Penumbra gibt. Beobachtungen deuten darauf hin, dass dieser Übergang bei

einem bestimmten Grenzwert des vertikalen Magnetfeldes auftritt, welcher nicht von der Größe des Sonnenflecks abhängt. Es ist aber noch eine offene Frage, inwiefern dieser Grenzwert des Magnetfeldes für das Einsetzen von Magnetokonvektion in der Penumbra verantwortlich ist.

Hier verwenden wir spektropolarimetrische Inversionen von Sonnenflecken, die auf Hinode-Daten basieren, um die physikalischen Eigenschaften der Umbra-Penumbra Grenze und der äußeren Grenze der Penumbra besser quantifizieren zu können. Wir bestimmen die Mittelwerte verschiedener physikalischer Größen entlang dieser Grenzen für Sonnenflecken unterschiedlicher Größe und bei verschiedenen optischen Tiefen. Daneben untersuchen wir, ob die großskalige Struktur von Sonnenflecken von ihrer Größe abhängt. Hierzu berechnen wir radiale Profile für verschiedene Sonnenflecken, also wie physikalische Größen von der Entfernung zum Zentrum des Sonnenflecks abhängen.

Wir können vorherige Studien bestätigen, nach denen das vertikale Magnetfeld nicht von der Größe des Sonnenflecks abhängt, wenn es entlang der Umbra-Penumbra Grenze gemittelt wird. Allerdings ist dies nur bei der mittleren Node ($\log \tau = -0.9$) der Inversion der Fall. In der obersten Node der Inversion ist das so gemittelte Magnetfeld für große Sonnenflecken größer als für kleine. Auch bei der Temperatur tritt ein solches Verhalten auf, wenn sie auf diese Weise gemittelt wird. Die Ursache hierfür ist vermutlich, dass penumbrale Filamente in den verschiedenen Schichten der Sonnenatmosphäre unterschiedlich aussehen.

Die radialen Profile zeigen wie erwartet, dass große Sonnenflecken kälter sind und ein stärkeres Magnetfeld aufweisen als kleinere Flecken. Allerdings ist dies nur in der Umbra und in der inneren Penumbra der Fall. In der äußeren Penumbra gibt es keine signifikanten Unterschiede zwischen Sonnenflecken verschiedener Größe. Besonders stark ist diese Ähnlichkeit beim Evershed-Fluss. Dies ist im Einklang mit vorherigen Studien, laut denen penumbrale Filamente sehr einheitlich sind und nicht stark von der Größe des Sonnenflecks abhängen.

Preface

The thesis is a combination of two different projects. (1) The characterisation and subsequent calibration of non-linearities of CMOS sensors, with the goal of increasing polarimetric accuracy. (2) A study of penumbral properties of sunspots. The first chapter is a small introduction to the overall work, with Chapter 2 introducing Sunspots and putting down the basis for using the next chapter, which is an introduction to polarimetry. Chapter 3 is an introduction to polarimetry and provides some insight into how camera non-linearity affects Solar polarimetry. Chapter 4 is an introduction to imaging sensors and describes the various sensor abnormalities. Chapter 5 describes the calibration setup and is needed to understand the rest of the work. The results for the camera characterisation are presented in Chapter 6. Chapters 3-6 provide an independent read and can be considered as one project. Chapter 7 is the paper (in preparation) on the study of Sunspots and primarily concerns the second project. It is mostly independent of the rest of the material presented, except Chapter 3 on polarimetry, which can be considered a common link between the two projects.

Appendix 1 covers the data computation and storage limitations of the calibration project. Appendix 2 describes the control software and presents an overview of its use for data collection.

Appendix 3 relates to the second project and covers the individual spots used in the project.

Contents

Abstract	i
Zusammenfassung	iii
Preface	v
List of Figures	xi
1. Introduction	1
2. General Properties of Sunspots	3
2.1. Structure of Sunspots	4
2.2. Thermal Properties of Sunspots	4
2.3. Magnetic Properties of Sunspots	4
2.4. The Penumbra	5
2.5. The Evershed Flow	7
2.6. The Umbra-Penumbra Boundary	8
3. Polarimetry	9
3.1. Introduction to Polarimetry	9
3.2. Solar Polarimetric Instruments	12
3.3. Need for High-Speed Large Format Cameras	14
3.4. Simulating the effect of Camera Non-Linearity on Polarimetry	15
4. An Introduction to Electronic Imaging Sensors	19
4.1. Light Sensors	19
4.2. Imaging Sensors	20
4.2.1. Passive Pixel Sensors (PPS)	20
4.2.2. Active Pixel Sensors (APS)	21
4.2.3. Analog to Digital Converter (ADC)	22
4.3. Non-Linearity in Imaging Sensors	24
4.3.1. Pixel Non-Linearity	24
4.3.2. Pixel Cross-Talk / Scene Dependent Behaviour	25
4.4. Noise and its Sources	27
4.5. Additional Sensor Problems	28
5. Calibration Setup for CMOS Imaging Sensors	29
5.1. The Parameter Space	29
5.2. Study of Targets	35
5.2.1. Masking Sensor Edges	36
5.2.2. Triangular Target	36

5.2.3.	Bar Target	38
5.2.4.	Multiple Light-Level Deductive Targets	41
5.3.	Setup	41
5.3.1.	Light Source	43
5.3.1.1.	Changing Current	44
5.3.1.2.	Pulse Width Modulation	44
5.3.1.3.	Phase Shift	46
5.3.2.	Trigger Box	48
5.3.3.	The Camera	48
5.3.4.	Mechanical and Cooling Elements	49
5.4.	An Alternative Setup	49
6.	Camera Characterisation Process and Results	51
6.1.	CAM1	53
6.1.1.	Preliminary Characterisation CAM1	53
6.1.1.1.	Slanted Edge Target	53
6.1.1.2.	Parallel Bar Target	55
6.1.2.	Results Calibration Targets	57
6.1.2.1.	Calibration Using Deductive Targets	58
6.1.2.2.	Calibration using the Independent Illumination Setup	60
6.2.	CAM2	67
6.3.	CAM3	75
6.4.	Schemes of Camera Calibration and Data Correction.	76
6.4.1.	Standard, Non-linearity Map w.r.t Integration Time, and Gain Maps	76
6.4.2.	Basic, Pixel by Pixel Non-Linearity Map w.r.t Light Level, and Gain Maps	76
6.4.3.	Banding Correction	76
6.4.4.	Calibration With Respect to Light Level, Row Average and Siblings	77
6.4.5.	Defective Pixel Map, Correction	78
6.5.	Discussion	78
7.	Results: General Properties of Sunspots	81
7.1.	Introduction	81
7.2.	Observations and Data Analysis	82
7.3.	Results	86
7.3.1.	Physical Properties at Umbra-Penumbra Boundary With Respect to Area of the Umbra	86
7.3.2.	Physical Properties at Outer Penumbra Boundary With Respect to Area of the Spot	86
7.3.3.	Physical Properties Across the Penumbra for Sunspots of Different Sizes	91
7.3.4.	Flow Profile Across the Penumbra	96
7.4.	Discussion	98
	Summary	101
	A. Data Storage Requirements	105

B. Controls and Experiment Time Requirements	107
C. Sunspots	111
Bibliography	113
Index	123
Acknowledgement	125
Curriculum vitae	127

List of Figures

2.1.	A complex sunspot observed by Hinode	3
2.2.	Minimum umbral intensity with respect to the umbral radius	5
2.3.	Maximum magnetic field strength with Minimum umbral intensity	6
2.4.	Structure of penumbral filaments	7
3.1.	Data mapping and accumulation techniques for multi-dimensional data	13
3.2.	Simulation scheme for studying the general effect of camera non-linearities	15
3.3.	Input Stokes parameters for the SUSI simulation	16
3.4.	Comparison of output Stokes parameter	17
3.5.	Comparison of stokes parameters: The green profiles showing the difference from the input for 0.2% row average dependence.	18
4.1.	A flow diagram showing the different stages of light sensing	19
4.2.	Basic schematics of a column parallel ADC	21
4.3.	The timing diagram for the MRSS and MRMS ADC architecture	23
4.4.	Quantisation step increase in a MRMS ADC	24
4.5.	Scene dependence example	27
5.1.	Parameter space covering row average and light level	31
5.2.	Qualitative illustration of target space covering row average and siblings	32
5.3.	Qualitative illustration of Two peak Row-histograms	33
5.4.	Qualitative illustration of Row histogram for two and three-level deductive targets	34
5.5.	Target space covering row-average and siblings	35
5.6.	Example targets	36
5.7.	Qualitative illustration of a Triangular target on a uniform illumination	37
5.8.	Qualitative illustration of a Triangular target on a gradient illumination	37
5.9.	Parallel Bar test	39
5.10.	Parallel Bar and 2 Sticks test	40
5.11.	An array of three light level targets	40
5.12.	Camera Characterisation Setup	42
5.13.	Illumination control of a pixel	43
5.14.	Time series for two different runs of the LED	45
5.15.	Frame averaged camera counts as a function of time after thermal stabilisation	45
5.16.	Illumination control using phase shift between LED and camera	46
5.17.	Time series for a run with 1/2 phase shifting mode	47
5.18.	Schematics of calibration setup containing a LED matrix as illumination source	50
6.1.	Flow diagram for the data processing	52
6.2.	Slanted target projected on Cam1, Ratio with uniform illumination	54

6.3. Slanted target projected on Cam1, Difference with fully illuminated frame	55
6.4. Parallel Bar test for CAM1	56
6.5. Example image showing the calibration region in test target image for calibration	58
6.6. Histogram of the pixels in the calibration region marked by the black rectangle in figure 6.5	59
6.7. Calibration region selected for testing	61
6.8. Complete target space with three different illuminations of the calibration region	61
6.9. Three dimensional data space	62
6.10. Two dimensional projections of the covered parameter space	63
6.11. Variation of counts in a pixel with respect to row average and siblings	63
6.12. Comparison of output to input before calibration, under different illumination scenes, CAM1	64
6.13. Comparison of output to input after correction, under different illumination scenes, CAM1	65
6.14. Comparison between different states	66
6.15. Example images for a fully illuminated sensor, and slant target	67
6.16. Averaged row profiles for dark and illuminated images, CAM2	68
6.17. Left and right shielded pixels and selected columns for Figure 6.18. Columns 10, 20, 30, 50 on the left edge and columns 2038, 2040, 2044, 2047 on the right edge.	69
6.18. Deviation of counts in the dark bands in the fully illuminated sensor	70
6.19. Deviation in the dark bands in the triangular target image, CAM2 flat illumination	71
6.20. Deviation in the dark bands in the triangular target image with respect to the row number, CAM2 gradient illumination	72
6.21. Deviation in the dark bands in the triangular target image with respect to the row average, CAM2 gradient illumination	73
6.22. Banding correction CAM2	74
6.23. Triangular target comparison for CAM3	75
7.1. Methods of defining distance contours in the spot	82
7.2. Continuum intensity (a,b,c) maps of a small, a medium and a large spot, respectively. The contours show the inner and the outer penumbra boundary.	83
7.3. Magnetic field Maps for small, medium and large spots	85
7.4. Magnetic field strength and Bz with respect to umbral area at umbra boundary	87
7.5. Inclination and temperature at the umbra-penumbra boundary	88
7.6. Magnetic field strength and Bz with respect to spot area at outer penumbral boundary	89
7.7. Inclination and Temperature at outer penumbral boundary	90
7.8. Magnetic field strength and Bz across the penumbra	92
7.9. Magnetic field strength across the penumbra for the central node	93
7.10. Vertical component of the magnetic field strength across the penumbra for the central node	93
7.11. Inclination and Temperature across the penumbra	94

7.12. Inclination across penumbra, along major and minor axis	95
7.13. Temperature across penumbra, along major and minor axis	95
7.14. Example image showing contours, and the region used for averaged plots.	96
7.15. LOS velocity across the spot	97
B.1. Main control panel for the Calibration setup	107
B.2. Control Panel while the calibration setup is running	108

1 Introduction

Light is one of the few things we receive from far away objects, and a measure of it gives us the information we seek about those far away objects. The most basic measure is the total intensity of the received radiation and its variation over time. The next thing is to look at the available spectrum of the received light, which is done by dispersing it using some dispersive element and looking at its time variation. A final property we can measure for a light packet is its polarisation giving rise to the field of polarimetry. Measuring the spectrum and polarisation means we know what happens to light as it passes through different mediums. Meaning that we know something about the place of origin of radiation, the path it travelled to us through, and finally, at the point of measure.

Let us start with the point of origin; the frequency and polarisation of the emitted light depend on the physical environment (temperature and the magnetic field). Moreover, it would change as it passes through different mediums. Thus, if we can make an educated guess about the emitting environment and medium the light passed through, we can make a model of the atmosphere and compare the parameters generated from the model with the measured parameters. Furthermore, a few iterations to the model to match the generated parameters with the measured ones can lead us to a realistic model of the atmosphere of the emitting source; this is the current state of solar-polarimetry. We try to do that for different physical features of the Sun; in our case, we primarily study the sunspots, revealing the physical structure of spots. We study how the magnetic field and the temperature vary across the spot and look at the plasma flow across the penumbra. Building these models of spots gives us the required information for making models for the overall atmosphere of the Sun.

However, making these comparisons requires correctly measuring the spectrum and the polarisation. That means we have accurate sensors, but there are always limits to the manufacturing processes and the conditions in which these sensors will work. The only way to have accurate sensors is to calibrate them. In our case, we would primarily be dealing with imaging sensors. Ground-based solar polarimetry problems introduce some limitations on these sensors' operating speed. Unfortunately, no cameras on the market satisfy these scientific requirements, thus leading us to investigate the problems with the available cameras. One of the significant problems with these cameras is the problem of cross-talk and noise. However, calibrating or correcting comes later; we first need a setup to investigate all the problems (electronic as well as thermal) with the sensors. Doing that requires that we already know something about the architecture and working of these imaging sensors. However, no manufacturer on the market would want to share that information (the electronic architecture). Thus we require a setup that can also investigate

this architecture for different sensors.

Correcting for these effects and checking if these corrections work is the next stage. It not only requires the development of new cameras which correct for the observed effects but also computational techniques that can work as an alternative in case we use these cameras with non-linearities. There has been much development in the computational department, using neural networks for image recognition and colour correction and all the fancy features we would find in the camera application of a modern phone. The only problem is that most of this development has taken for applications where the camera/sensors work at a signal level much above the noise floor, which is not the case for solar polarimetry. The development in camera manufacturing has allowed us to make cameras with a much larger density and complexity of pixels. While still keeping a decent frame rate, for example, more than 10 fps (frames per second) for a camera having more than 50 mega-pixels. However, the level of cross-talk and other non-linearities has increased as well. Thus we need a setup that addresses these problems. We also discuss the limitations (computational and data storage) of this project and the future outlook of the calibration setup.

2 General Properties of Sunspots

The variation of the magnetic field and temperature across the solar photosphere gives rise to several visible structures at different scales. The first classification that can be done is based on the intensity, whether the visible structure is brighter (faculae, for example) or darker (sunspots, for example) than the mean quiet Sun. The features having a lower intensity than the surrounding quiet Sun can also be grouped by size and by the physical properties which they exhibit. The two most prominent ones are the pores and sunspots, differentiated by the fact that sunspots show a prominent fanning out of the magnetic field, giving rise to the penumbra, which is missing in the pores. This chapter is a small introduction to some of the physical properties of a sunspot.

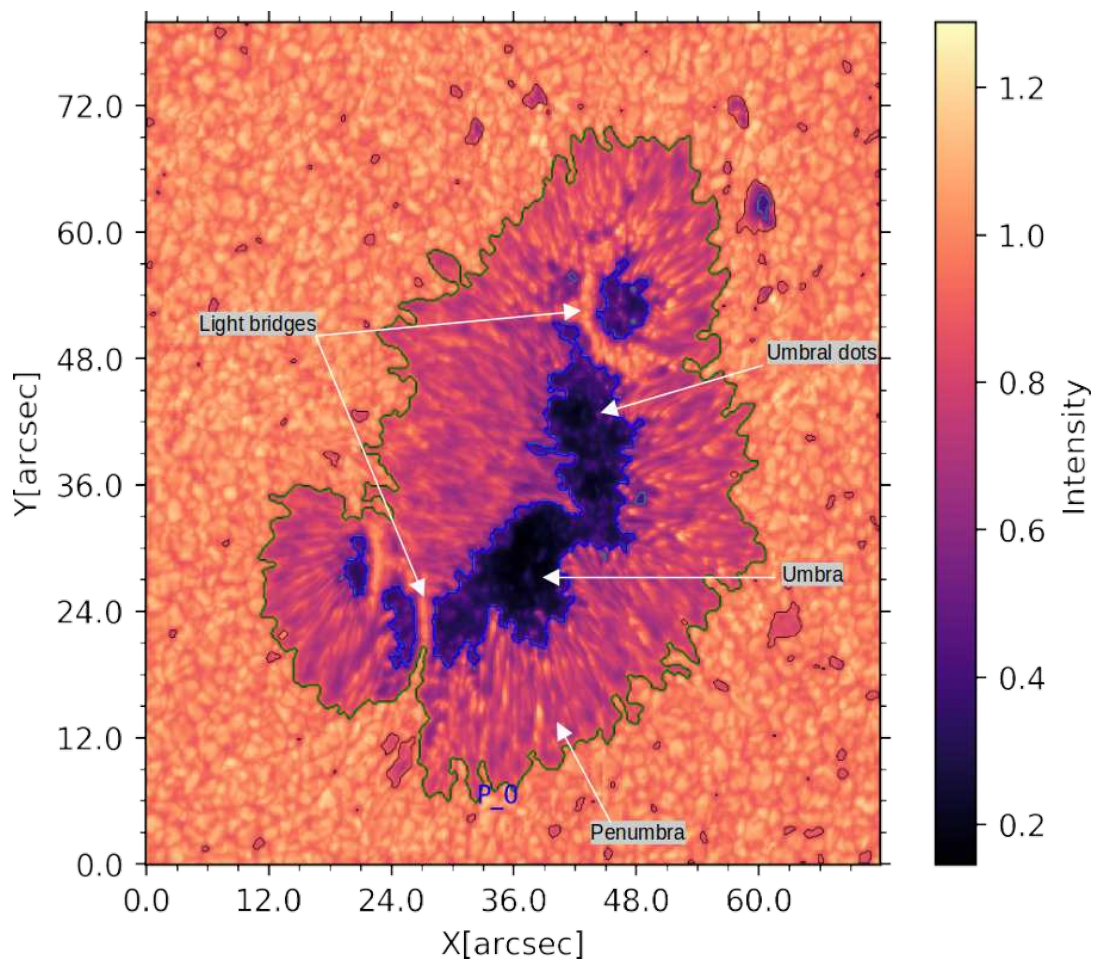


Figure 2.1.: A complex sunspot observed by Hinode on 2007.05.04 at a distance of 37° from the disk centre, NOAA number 10953.

2.1. Structure of Sunspots

Sunspots are extended regions on the Sun with a strong magnetic field. This magnetic field concentration means a new balance must be established between the gas and magnetic pressure. This means that a region with a larger magnetic field concentration will have less plasma and a lower temperature than the surrounding region, as the convection will be suppressed in regions of a stronger magnetic field. The visible manifestation of this concentration on the solar photosphere are dark regions, the sunspots. Sunspots have diameters ranging from 1 to 20 Mm (Bogdan et al. 1988). Extensive introductions to sunspots can be found in Solanki (2003) and Borrero and Ichimoto (2011).

A simple spot has mainly two parts, the umbra and the penumbra. The umbra is the region containing the concentrated magnetic field and is mostly devoid of plasma. The second is the penumbra, signifying the fanning out of the magnetic field and plasma flow. As the size of the spot increases, more complex structures, like light bridges, may form. Certain finer structures like umbral dots can be seen with increasing image resolution within the umbras, as marked in figure 2.1.

2.2. Thermal Properties of Sunspots

Sunspots are significantly darker than the quiet Sun. The umbra reaches only 10 – 30 % of the mean continuum intensity of the quiet Sun ($I_{C,QS}$). It is surrounded by the brighter penumbra, which exhibits 75 – 85 % of the intensity of the quiet Sun. The intensity increases monotonically from the center of the umbra to the outer boundary of the spot. It shows a sharp increase at the boundary between the umbra and the penumbra (Keppens and Martinez Pillet 1996, Mathew et al. 2003, Tiwari et al. 2015). The temperature decreases with height across the spot (e.g., Tiwari et al. 2015).

The umbral brightness and the mean brightness of sunspots substantially decreases with increasing radius of the spot (Brandt et al. 1992, Beck and Chapman 1993, Chapman et al. 1994, Mathew et al. 2007, Kiess et al. 2014). The intensity of the umbra shows a non-linear inverse relation with the radius of the umbra, where the slope is steeper for the smaller umbrae, and it becomes less steep for larger umbrae, as can be seen in figure 2.2 made for spots in cycle 24 by Kiess et al. (2014).

2.3. Magnetic Properties of Sunspots

The magnetic field in the umbra ranges from 1800 G to 3700 G (Livingston 2002, Kiess et al. 2014), with larger spots having stronger magnetic fields strength (e.g., Kopp and Rabin 1992, Livingston 2002, Rezaei et al. 2012, Schad 2014, Watson et al. 2014, Kiess et al. 2014, Rezaei et al. 2015). Here, the maximum field strength and the minimum umbral intensity are inversely related (see figure 2.3), (Kopp and Rabin 1992, Kiess et al. 2014, Rezaei et al. 2015). The strength of the magnetic field drops as we move to the

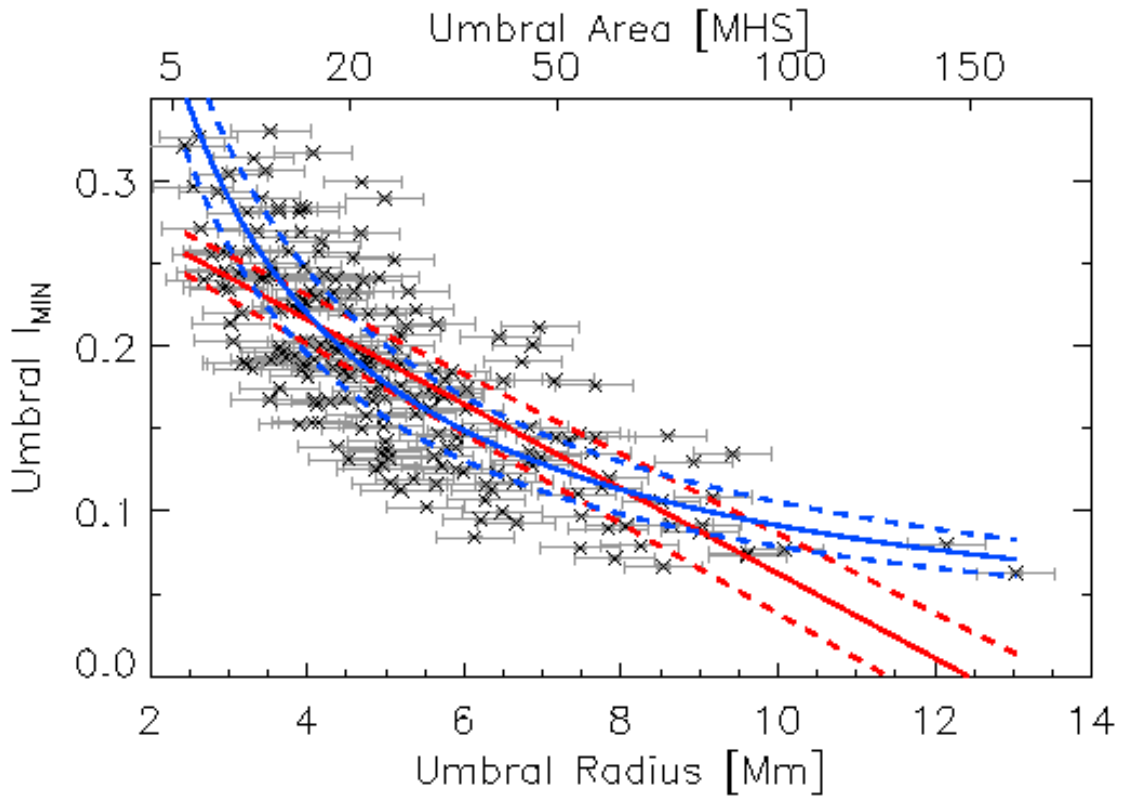


Figure 2.2.: The minimum umbral intensity with respect to the umbral radius. Where the red and the blue lines show a linear and power law fit, with the dashed lines showing the one-sigma confidence level for the fits, for more details (see Kiess et al. 2014, Table 1).

periphery of the spot (Lites and Skumanich 1990, McPherson et al. 1992, Solanki et al. 1992, Balthasar and Schmidt 1993, Hewagama et al. 1993, Keppens and Martinez Pillet 1996, Rueedi et al. 1998, Westendorp Plaza et al. 2001b, Mathew et al. 2003, Borrero et al. 2004, Bellot Rubio et al. 2004, Sánchez Cuberes et al. 2005, Langhans et al. 2005, Borrero and Ichimoto 2011, Tiwari et al. 2015, Joshi et al. 2017). The strongest field is mostly seen in the dark regions of the umbra, and is primarily vertical. As we move outward, the field becomes more and more horizontal, with the inclination of the magnetic field ranging between $20 - 30^\circ$ at the centre of the umbra and increasing to $80 - 90^\circ$, as we move from the centre of the spot to the edges. The magnetic field strength decreases monotonically with height (e.g., Tiwari et al. 2015, Joshi et al. 2017). Thus, the magnetic field fans out with height. Beyond the outer boundary of the sunspot, it overlies field-free gas and forms a canopy structure (Solanki et al. 1992, 1994).

2.4. The Penumbra

The mean penumbral intensity ranges between $0.75 - 0.85$ of the mean continuum intensity, where it decreases linearly with the spot area in the given range (see Mathew et al. 2007, Figure 13). The penumbra has a non-homogeneous structure consisting of both penumbral filaments and spines. Spines are essentially a continuation of the umbra. They

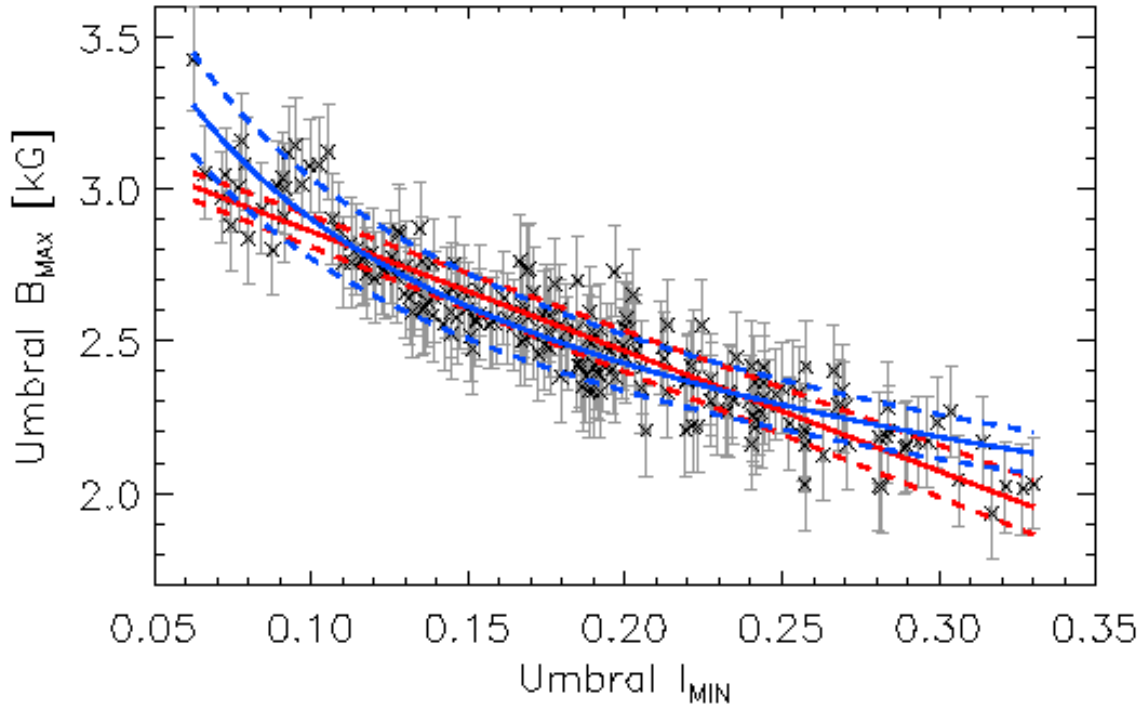


Figure 2.3.: Maximum magnetic field strength with Minimum umbral intensity. Figure adapted from Kiess et al. (2014).

are dark and exhibit a strong, almost vertical magnetic field (Lites et al. 1993). Penumbra filaments, on the other hand, have more horizontal magnetic fields. Spines and penumbra filaments are interlaced with each other, which is referred to as interlocking comb structure (Title et al. 1993, Solanki and Montavon 1993, Lites et al. 1993, Tiwari et al. 2013).

The penumbra filaments are long, elongated structures with a length of 2 – 8'' and a width of about 0.8'' (Tiwari et al. 2013). There is evidence that penumbra filaments are a result of magnetoconvection, both from observations (Scharmer et al. 2002, Bellot Rubio et al. 2005, 2007, Langhans et al. 2007, Rimmele 2008, Bharti et al. 2010b) and from simulations (Scharmer et al. 2008, Zakharov et al. 2008, Rempel et al. 2009, Rempel 2011, Rempel and Cheung 2014). The emerging picture of penumbra filaments is presented in Fig. 2.4, which shows the observables for an ensemble average over several individual penumbra filaments (Tiwari et al. 2013). The penumbra filaments can be separated into a head, a body, and a tail. The head is bright (brighter than the main body of the filaments and brighter than the surrounding spines anyway) and exhibits a strong, almost vertical magnetic field of umbral polarity and strong upflows that can reach several km/s. The head is followed by the body of the penumbra filament, in which both the magnetic field and the flow are almost horizontal along the central axis of the filaments. The tails of the penumbra filaments show strong downflows, and the magnetic field is close to vertical, but with the polarity being opposite to the one of the umbra.

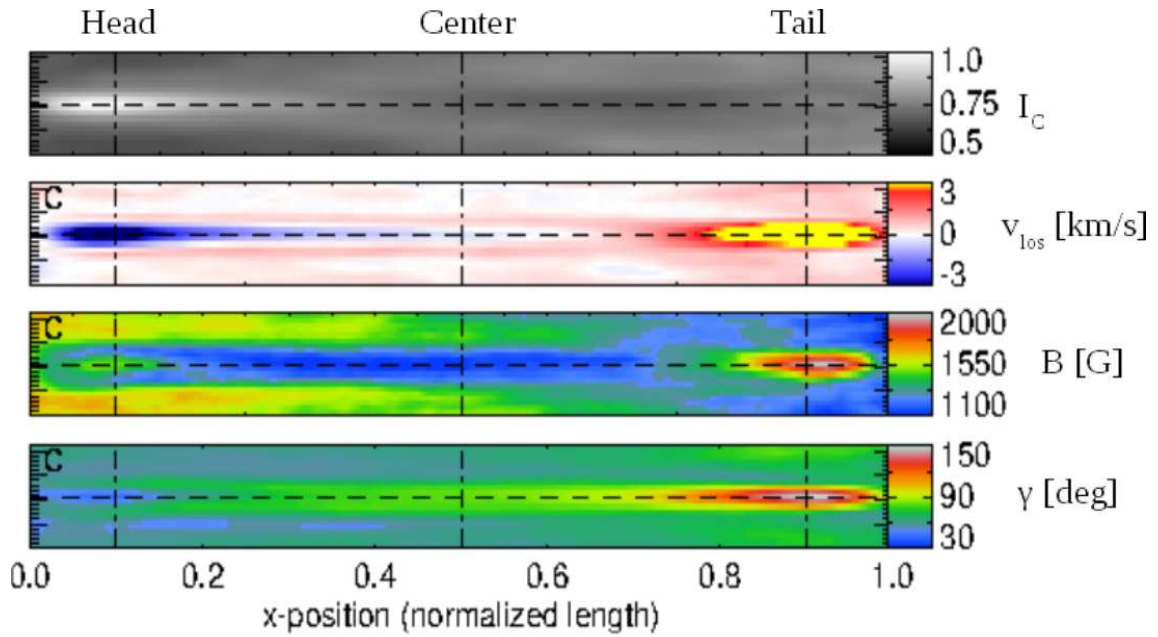


Figure 2.4.: Structure of penumbral filaments. From top to bottom: continuum intensity, Doppler velocity, the strength of the magnetic field, and inclination of the magnetic field. The observables are derived from an ensemble average of several penumbral filaments. Figure adapted from Tiwari et al. (2013).

Rucklidge et al. (1995) modelled the transition process from pores to sunspots as a bifurcation process, with the penumbra forming as the inclination of the outer edge of the flux tube exceeds a certain threshold. The active accumulation of more magnetic flux in the pores leads to a larger inclination at the outer boundary of the pore and leads to penumbra formation (Rucklidge et al. 1995, Leka and Skumanich 1998, Schlichenmaier et al. 2010). The other model of the penumbra is based on the premise that the overlying magnetic field in the chromosphere can trap the newly emerging flux in the photosphere and prevent it from becoming vertical (Leka and Skumanich 1998, Lim et al. 2013).

2.5. The Evershed Flow

When located close to the limb, spectral lines in the penumbrae of sunspots show blueshifts at the side of the penumbra that points towards the disk centre and redshifts at the side that points toward the limb. These shifts of spectral lines are due to a radial outflow in the penumbra, the Evershed flow (Evershed 1909). The Evershed flow consists of the horizontal flow along individual penumbral filaments, as described above. Depending on the viewing angle, the Evershed flow has flow velocities of several km/s, reaching even supersonic velocities in some cases (Wiehr 1995, del Toro Iniesta et al. 2001, Bellot Rubio et al. 2004, Borrero et al. 2005). Penumbral filaments exhibit downflows at their tails, and most of the Evershed flow returns below the solar surface at these locations (Westendorp Plaza et al. 1997, 2001a). A small part of the flow, however, continues in the canopy of the sunspot (Solanki et al. 1994).

2.6. The Umbra-Penumbra Boundary

The umbra-penumbra boundary is often defined as $0.5 I_{QS,C}$, where $I_{QS,C}$ is the mean continuum intensity in the quiet Sun. The exact boundary may vary with values and methods used to define it, but the important point is that there is a boundary region that may be defined from 0.4 to $0.6 I_C$ in the visible spectral range. This region is marked by a steep increase in intensity and temperature. And a similar transitioning effect was suspected for the magnetic field. Much of the work on boundary fields was presented by Jurčák (Jurčák et al. 2015, 2018, 2020), where it is claimed that the umbra penumbra boundary, defined at $0.5 I_C$, corresponds to a constant value of the vertical magnetic field of 1867 G. Although the value was obtained using height independent inversions and can only be understood as a mean over heights, this came to be known as the Jurčák criterion. Similar studies by other authors showed a similar constant, albeit different value. Schmassmann et al. (2018) found it to be 1693 G, while Lindner et al. (2020) found that the contours of the intensity and of B_z matched well at 1787 G. However, Benko et al. (2018) found that decaying spots do not have a constant B_z at the umbra boundary. Jurčák already saw this behaviour to some extent in Jurčák et al. (2018). A threshold was applied to the minimum spot size and was explained by saying that those small spots are still in the process of formation and the Jurčák criterion holds for the stable phase of the spots, not in the evolutionary state. Löptien et al. (2020) used height-dependent inversions and found different fixed values of continuum intensity gave an invariance of B_z at different nodes of the inversion. He also found the Jurčák criterion to be failing for small spots. Here it was explained that the constant value of B_z at $0.5 I_{QS,C}$ is caused by the brightness dependence of penumbral filaments on the spot size. Further studies using height-dependent inversions are needed to get a clearer picture of the physical quantities at the umbral boundary.

Although much work has been done on the finer structure of the spots, there are many open questions, and some debates are still not settled. And that is the context we would like to place this work being done on the calibration of the imaging sensor. With bigger telescopes and newer and more efficient spectropolarimeters being made, it becomes critical to have imaging sensors free of artefacts. We will look at how the sensor non-linearities affect polarimetry and how to correct them.

3 Polarimetry

3.1. Introduction to Polarimetry

To get as much information from light as possible, we need to know its intensity, direction of travel, time of arrival, wavelength, and polarization. For solar observations, the direction of travel of detected light is given by the pointing of the telescope and time of arrival is determined by the shutter of the detector. The other three properties are more fundamental and will mainly be presented here.

The energy flux density carried by an electromagnetic wave across a surface is given by the Poynting vector,

$$\mathbf{S} = \frac{c}{8\pi} \mathbf{E} \times \mathbf{H} \quad (3.1)$$

This equation leads us to the polarization tensor, or the coherency matrix, where the diagonal elements are real, and off-diagonal elements are complex, as given in the equation below:

$$\mathbf{C} \equiv \begin{pmatrix} \langle E_x(t)E_x^*(t) \rangle & \langle E_x(t)E_y^*(t) \rangle \\ \langle E_y(t)E_x^*(t) \rangle & \langle E_y(t)E_y^*(t) \rangle \end{pmatrix} \quad (3.2)$$

Here, for the case of quasi-monochromatic light, the components can be described by

$$E_x(t) = [\xi_x(t)e^{i\phi_x(t)}] e^{-2\pi i\nu_0 t} \quad (3.3)$$

It is essentially a monochromatic plane wave of frequency equal to its mean frequency (ν_0); the complex amplitude gets modulated with time. This leads to

$$\mathbf{C} = \begin{pmatrix} \langle \xi_x^2(t) \rangle & \langle \xi_x(t)\xi_y(t)e^{i\phi(t)} \rangle \\ \langle \xi_x(t)\xi_y(t)e^{-i\phi(t)} \rangle & \langle \xi_y^2(t) \rangle \end{pmatrix} \quad (3.4)$$

with $\phi(t) \equiv \phi_x(t) - \phi_y(t)$.

The Stokes formalism describes this coherency matrix in terms of real measurable quantities. The elements of the Stokes vector are real linear combinations of the coherency matrix:

$$\begin{aligned} I &\equiv \kappa(\mathbf{C}_{11} + \mathbf{C}_{22}) = \kappa(\langle \xi_x^2 \rangle + \langle \xi_y^2 \rangle), \\ Q &\equiv \kappa(\mathbf{C}_{11} - \mathbf{C}_{22}) = \kappa(\langle \xi_x^2 \rangle - \langle \xi_y^2 \rangle), \\ U &\equiv \kappa(\mathbf{C}_{12} + \mathbf{C}_{21}) = 2\kappa\langle \xi_x \xi_y \cos\phi(t) \rangle, \\ V &\equiv i\kappa(\mathbf{C}_{21} - \mathbf{C}_{12}) = 2\kappa\langle \xi_x \xi_y \sin\phi(t) \rangle. \end{aligned} \quad (3.5)$$

Here κ is a dimensional constant. Thus \mathbf{C} can be written in terms of the standard Pauli matrices as

$$\mathbf{C} = \frac{1}{2\kappa}(I\sigma_0 + Q\sigma_1 + U\sigma_2 + V\sigma_3) \quad (3.6)$$

where I,Q,U and V are just the coefficients of the linear expansion. From the binding conditions of \mathbf{C} ,

$$\text{Tr}(\mathbf{C}) \geq 0, \quad \det(\mathbf{C}) \geq 0 \quad (3.7)$$

we arrive at

$$I \geq 0, \quad \text{and} \quad I^2 - Q^2 - U^2 - V^2 \geq 0 \quad (3.8)$$

respectively.

The special case ($Q = U = V = 0$) describes the case of completely unpolarized light. The other cases describe partially polarised light. The polarization vector is defined as

$$\mathbf{p} \equiv \left(\frac{Q}{I}, \frac{U}{I}, \frac{V}{I} \right)^T \quad (3.9)$$

with the superscript T denoting the transpose. The magnitude of \mathbf{p} gives one the degree of polarisation:

$$0 \leq p = \frac{\sqrt{Q^2 + U^2 + V^2}}{I} \leq 1, \quad (3.10)$$

where p is between p=0, completely unpolarized light and p=1, completely polarized light. Grouping all the Stokes parameters into a four-vector gives us the resulting Stokes vector.

$$\mathbf{I} \equiv (I, Q, U, V)^T. \quad (3.11)$$

Transformation of Stokes vector

As the light passes through an optical element, the Stokes vector is transformed, where the optical element can be considered as imparting a linear transformation \mathbf{M} . Thus the resulting Stokes vector can be written as

$$\mathbf{I}' = \mathbf{M}\mathbf{I}, \quad (3.12)$$

$$\begin{pmatrix} I' \\ Q' \\ U' \\ V' \end{pmatrix} = \begin{pmatrix} M_{00} & M_{01} & M_{02} & M_{03} \\ M_{10} & M_{11} & M_{12} & M_{13} \\ M_{20} & M_{21} & M_{22} & M_{23} \\ M_{30} & M_{31} & M_{32} & M_{33} \end{pmatrix} \begin{pmatrix} I \\ Q \\ U \\ V \end{pmatrix} \quad (3.13)$$

where \mathbf{M} is the Mueller matrix. And if light encounters an optical train with optical elements in the order (i=1,2,3..n) the final Mueller Matrix is given by

$$\mathbf{M} = \mathbf{M}_n \mathbf{M}_{n-1} \dots \mathbf{M}_2 \mathbf{M}_1 \quad (3.14)$$

with \mathbf{M}_i being the Mueller matrix of each element.

Measurement of Polarization

The Stokes vector (polarization) measurement requires a linear analyzer and a retarder. The analyzer is an element that maximizes the transmittance of light along a preferred optical axis and minimizes along the orthogonal axis. The linear retarder is an element that introduces a phase lag between the two axes. The measurement of the optical axis and phase provides complete polarization information. However, given that any optical sensor only measures energy, we need a combination of measurements to derive the Stokes vector, as shown below.

The components of the electric field vector after passing through an analyser and retarder are given by, respectively,

$$E'_x = E_x \cos(\theta) \quad \text{and} \quad E'_y = E_y \sin(\theta) \quad (3.15)$$

$$E'_x = E_x \quad \text{and} \quad E'_y = E_y e^{i\delta}, \quad (3.16)$$

where θ is the angle from the x axis, and δ is the imparted phase lag, when x is the fast axis of the retarder. Thus the final electric vector after it passes through a retarder and an analyser is given by,

$$E_\theta(t; \delta) = E_x \cos(\theta) + E_y \sin(\theta) e^{i\delta} \quad (3.17)$$

with the mean intensity given by,

$$I_{mean}(\theta, \delta) = \langle E_\theta(t; \delta) E_\theta^*(t; \delta) \rangle, \quad (3.18)$$

$$I_{mean}(\theta, \delta) = \langle E_x E_x^* \cos^2 \theta + E_y E_y^* \sin^2 \theta + \frac{1}{2} E_x E_y^* \sin(2\theta) e^{-i\delta} + \frac{1}{2} E_x^* E_y \sin(2\theta) e^{i\delta} \rangle. \quad (3.19)$$

Using the Stokes parameters as defined in Equation 3.5 we obtain,

$$\begin{aligned} \langle E_x E_x^* \rangle &= 1/2(I + Q), \\ \langle E_y E_y^* \rangle &= 1/2(I - Q), \\ \langle E_x E_y^* \rangle &= 1/2(U + iV), \\ \langle E_x^* E_y \rangle &= 1/2(U - iV), \end{aligned} \quad (3.20)$$

allowing to express the mean intensity as a linear combination of Stokes parameters:

$$I_{mean}(\theta, \delta) = \frac{1}{2}(I + Q \cos(2\theta) + U \cos(\delta) \sin(2\theta) + V \sin(\delta) \sin(2\theta)) \quad (3.21)$$

Hence by varying θ and δ we can determine the Stokes parameters as

$$\begin{aligned} I &= I_{mean}(0, 0) + I_{mean}(\pi/2, 0), \\ Q &= I_{mean}(0, 0) - I_{mean}(\pi/2, 0), \\ U &= I_{mean}(\pi/4, 0) - I_{mean}(3\pi/4, 0), \\ V &= I_{mean}(\pi/4, \pi/2) - I_{mean}(3\pi/4, \pi/2). \end{aligned} \quad (3.22)$$

The above equations only give a set of possible measurements. Many other linear combinations of measurements can reveal the same Stokes vector, and the set of measurements

used is called the modulation scheme required for polarimetric measurements. And the simplest modulation will happen in time, meaning that we make a measurement of intensity at one polarimetric configuration, change it, and make a second measurement, thus requiring us to take a set of images. For further details on polarimetry we refer to *Principles of Optics* (Born and Wolf 2019) and *Introduction to Spectropolarimetry* (del Toro Iniesta 2003).

It needs to be stressed that polarimetry (of visible light) is a differential photometric measurement: the polarimetric signal is derived from the difference of individual measurements, thus any effect that causes a photometric variation between the individual measurement will result in a polarimetric signal, regardless of the true nature of that variation. Characterisation and calibration of systematic photometric errors, in particular non-linearity and electronic cross talk between picture elements (pixels), inherent to high-speed electronic image sensors used for instrumentation in solar physics, is the topic of this thesis.

3.2. Solar Polarimetric Instruments

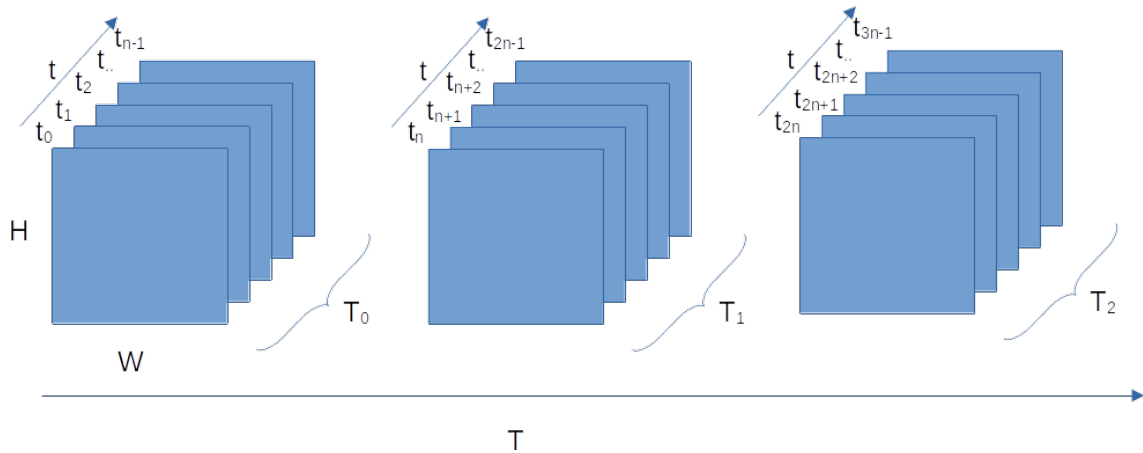
Here we discuss the very basic principle of spectrometric instruments, and how camera non-uniformity (variation of pixel to pixel response) and pixel non-linearity (inherent light response non-linearity of the pixel) enter into the recorded data.

Even for the simple case where we do not consider the polarimetric signal we have a three dimensional data cube, two dimensions (x and y) for the spatial information, and one for wavelength (λ). This information needs to be mapped onto a two-dimensional sensor. Figure 3.1a shows a basic scheme for collecting multi-dimensional data using a two-dimensional sensor. Data collected at time T_0 corresponds to one spectropolarimetric data cube. Figure 3.1b shows the different data mapping techniques (spatial and wavelength). The polarimetric information is typically recorded as a modulation in time, and contained in one of the frames along t .

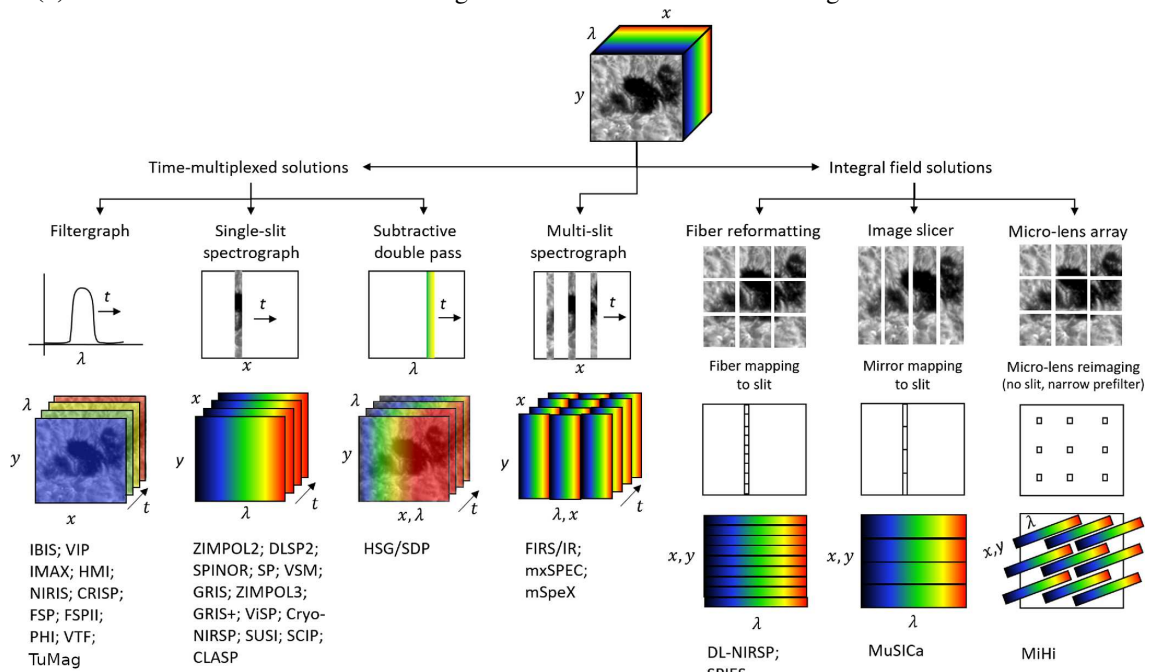
Filtergraphs The complete spatial information (both dimensions x and y) is mapped onto the sensor, while we need to scan for the wavelength (λ) information in time (t).

Let us look at the role of camera non-linearity here. For simplicity, we shall consider the pixel non-linearity (as described in section 4.3.1). As each pixel samples intensity as a function of filter position to obtain the spectrum, a non-linear response of the pixel will modify the shape of the spectrum (spectral lines becoming deeper or shallower). All pixels have a slightly different response, and this camera non-uniformity plays a role when we want to compare wavelength data for two pixels. Now all of this is for the timestamp T_0 , for comparison of this with any other timestamp we will need to consider both the non-linearity and non-uniformity.

Spectrographs The spectrum for one spatial dimension is mapped onto the sensor, and the scanning is done for the remaining spatial dimension. The spectrum from a narrow slit is dispersed onto the image sensor (as can be seen in the second subfigure (from the left) for figure 3.1b).



(a) Data collection scheme for collecting a multi-dimensional data set using a two dimensional sensor.



(b) Data mapping techniques, for the spectral and spatial data. Figure adapted from Francisco and Feller (2019)

Figure 3.1.: Data mapping and accumulation techniques, for multi-dimensional polarimetric data.

For time stamp T_0 the non-uniformity of the sensor effects the recorded spectrum for one spatial element, and it also makes it uncomparable for the spatial dimension (y) recorded in one frame (recorded at t_0) itself. The pixel non-linearity gets manifested into the spectrum recorded as we scan along the second spatial dimension in time (along t). For any kind of comparison of one spatial element at T_0 to any other time stamp, both the non-uniformity and non-linearity will come into play.

Integral Field Solutions From the camera point of view, an integral field unit is the same as a spectrograph, just that the sensor area is being shared for both the spatial and wavelength information. And practically, it is still the spectra being mapped onto the sensor, and hence for one frame (at t_0) it is mainly the non-uniformity that comes

into play, for the data of one spatial element. But any comparison with a second frame needs to account for the pixel non-linearity.

Thus even without pixel cross-talk, the pixel non-linearity and the camera non-uniformity affect the collected data, with the non-linearity affecting inter-frame measurements and the non-uniformity affecting the intra-frame measurements. The basic pixel non-linearity and the non-uniformity can be accounted for using some of the standard calibration techniques (dark + flat correction) and per-pixel non-linear calibration with respect to the light illumination. The difficulties arise when inter-pixel cross-talk becomes substantial because then the response of a single pixel no longer depends on the number of collected photo-electrons and the properties of that pixel alone but also on the number of electrons captured in all other pixels (or a subset of these). In this case, the response of each pixel becomes scene dependent.

3.3. Need for High-Speed Large Format Cameras

The primary need for high-speed cameras arises from the fact that we must compensate for atmospheric seeing in ground-based observations. One of the ways to compensate for atmospheric seeing is to take snapshots at a rate faster than the change in the atmosphere. Alternatively, use adaptive optics, which corrects atmospheric seeing. However, here too, the principle is to correct before it changes and hence requires a high-speed sensor to detect the wavefront. The bottom line is gathering the information in the wavefront before it changes significantly, or we will have smearing/blurring. Most telescopes use adaptive optics these days, and in solar physics, in particular, a combination of adaptive optics and numerical image restoration (see van van Noort et al. (2005)) is routinely used for imaging applications.

Conventional spectropolarimeters, shown in the left branch in figure 3.1b need to scan in the spatial or wavelength dimensions to get the complete spectral information at each point in the telescope's field of view. In addition, we would also need some modulation schemes for polarimetry, as mentioned in section 3.1. This means we must take multiple images to acquire the full information. Thus, the time needed to sample the wanted information determines the amount of evolution we can see on the Sun. The only way to reduce the time to obtain such information boxes is to map more than two dimensions on the image sensor. This requires suitable optics to map both spatial dimensions and the wavelength on a two-dimensional sensor and sets much-increased requirements on the number of pixels the sensor needs to provide, as for the instruments shown in the right branch of the flow diagram figure 3.1b. Given that the readout time would increase with the number of pixels, these cameras must have a high readout speed or allow for readout during integration, thus increasing the duty cycle and decreasing the photons lost between the frames. Here duty cycle refers to the ratio of exposure time to total frame time; we aim for it to be higher than 90%.

The light level non-linearity in most commercial cameras is typical of the order of 5% of the camera illumination. Good ones will bring it down to below 1%; the industrial cameras would leave it at about 10% of the illumination at the nominal light level. These

values are often specified by the manufacturer or can be obtained by a quick linearity test of the camera. However, the use case of the camera determines the required value. Sadly we do not have manufacturers who would manufacture cameras specifically for our use case, where we require large format sensors with high-speed readout (preferably a global shutter camera with 100 fps). Hence, we must select one of the commercially available cameras and calibrate it to a level suitable for the scientific use case. The main goal of the thesis, in a sense, is to see if this is possible.

Now let us see why camera non-linearity is such a massive problem in solar polarimetry or even spectrometry. The main reason is the negative spectrum; the spectral lines are seen as a dip in the nominal intensity, commonly referred to as the absorption spectrum. This negative spectrum causes a few problems, the first of which is the contamination of the dark spectral lines by the light in the bright spectral region. The second is the camera non-linearity, mainly driven by the average illumination of the sensor, also affecting the dark spectral lines.

Thus, the camera's non-linearity will have a more significant problem in any camera application where the region of interest has a significantly lower intensity than the surrounding, as the average illumination drives the error. This problem is different from photon noise, which would increase with the light level falling onto the pixel. It becomes clear if we look at the resulting error as a fraction of the signal, for example, an error of 1 count when the pixel count is 5 and the same error when we have 100 counts for the pixel.

3.4. Simulating the effect of Camera Non-Linearity on Polarimetry

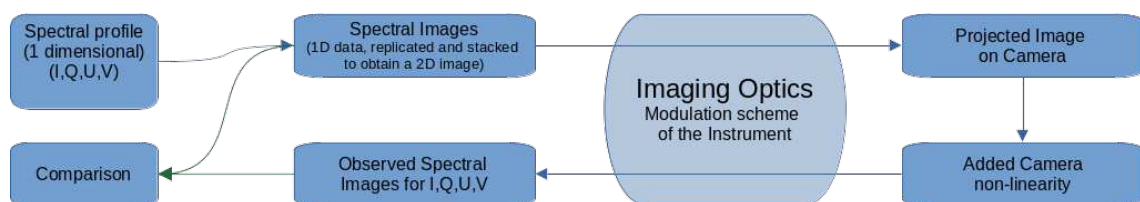


Figure 3.2.: Simulation scheme for studying the general effect of camera non-linearities.

To get an impression of the impact of sensor non-linearity on polarimetric measurements, we carry out tests with a simulated (ideal) instrument and synthetic spectropolarimetric data. Specifically, we try to simulate the effect of the camera non-linearity on the polarimetric accuracy of the Sunrise Ultra-violet Spectropolarimeter and Imager (SUSI) (Feller et al. 2020). SUSI is an upgrade of the Sunrise Filter Imager used for the Sunrise I and II flights (Gandorfer et al. 2011, Solanki et al. 2010, Barthol et al. 2011, Solanki et al. 2017).

SUSI is a dual-beam spectropolarimeter assembled at MPS. The cameras used in the instrument are marked as CAM2 in the results section, and some of the observed non-linear effects are described there. We start with a raw spectrum and generate spectral images

seen by the telescope. These images are then taken through the modulation scheme of the instrument to generate images as they would be projected onto the camera, where the spectrum is contained in one row. At this stage, a known camera non-linearity is added to these images. The thus generated images are then demodulated to get the spectrum images back and compared to the original spectrum images to get the effect of the camera non-linearity. The overall scheme of the simulation is shown in the figure 3.2.

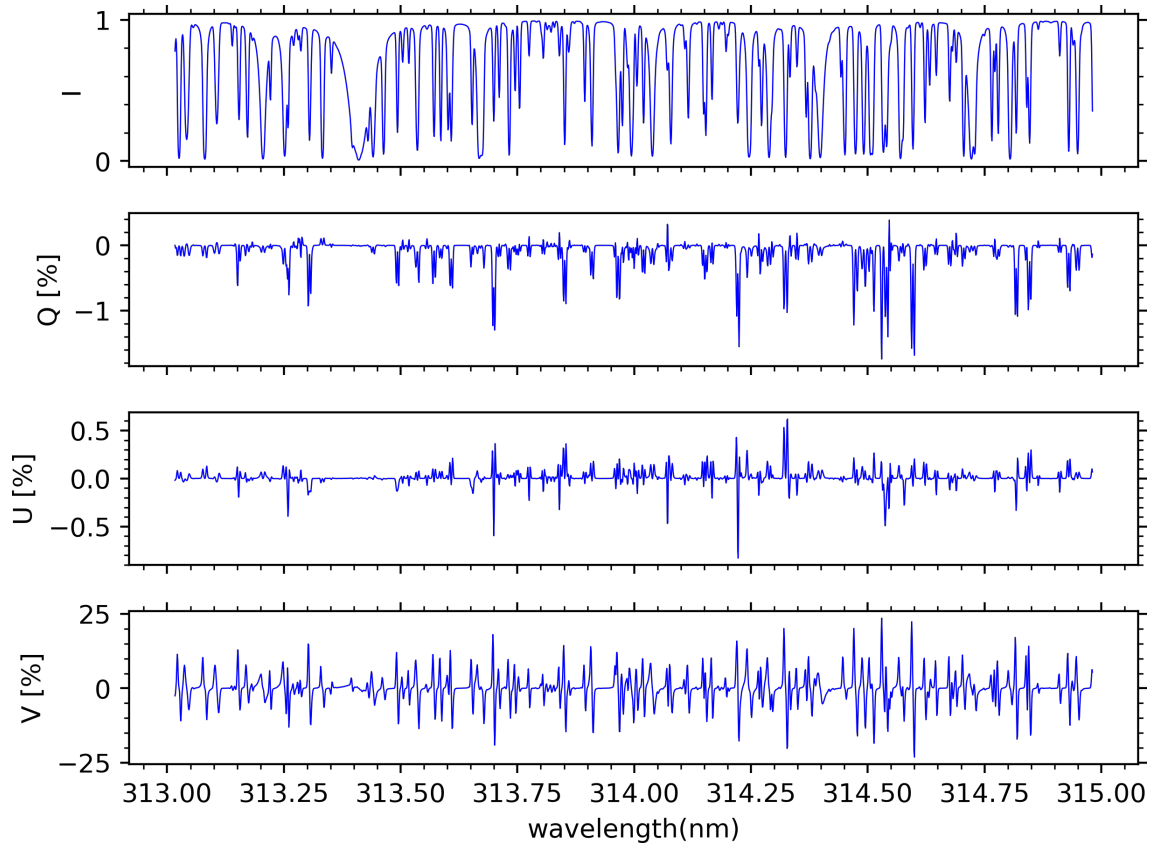


Figure 3.3.: Input Stokes parameters for the Simulation. The profiles are normalised to mean quiet-Sun intensity.

The general form of the added non-linearity is given by

$$Counts = f(LL) \times (1 + g(LL) + h(row\ average)) \quad (3.23)$$

where counts of the sensor are given as a function of the intensity of the light (LL) falling on the sensor, and a non-linearity component of this intensity, given by $g(LL)$ and the secondary non-linear component given by $h(row\ average)$. The spectral range we use is the same as used by Riethmüller and Solanki (2019) centered at 314.0 nm, and the input Stokes parameters for our simulations are shown in figure 3.3. In the simplistic case shown here for just the row average dependence the exact form used is given as,

$$Counts(out) = Counts + a \times row\ average \quad (3.24)$$

Figure 3.4 shows the difference of the Stokes parameters for the case of 2% row-dependence ($a=0.02$), in red and 0.2% in green ($a=0.002$). $g(LL)$ is not considered in this case, and only the row dependence given by $h(\text{row average})$ is used, considering that there is no other non-linearity affecting the camera count. The black profile is the input Stokes I. Figure 3.5, is just the appropriately scaled version of the green profile in figure 3.4. All profiles are normalised to the mean quiet-Sun intensity.

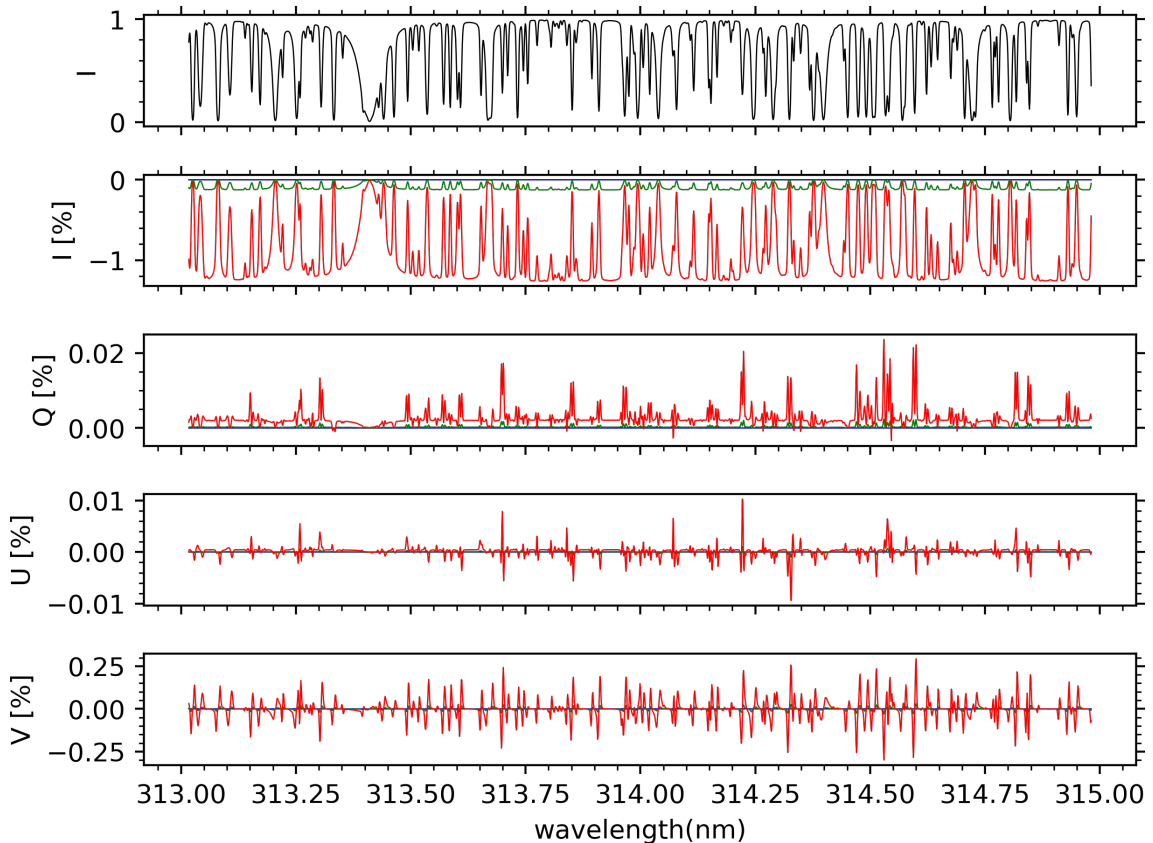


Figure 3.4.: Comparison of output Stokes parameter: The red profiles show the difference from the input for 2% camera non-linearity while the green profile shows the difference for 0.2% of row average dependence.

The outer bounds of difference from the input parameters (y-axis in figure 3.4 and 3.5) show the primary effect of the camera non-linearity, which corresponds to what Keller (1996) described for the case of no second-order term in the Intensity function ($f(x) = b \times x + c$). In this typical case, the false polarimetric signal goes as $0.1 \times a$. The exact camera non-linearity gives the details of the change in the spectrum. This simulation suffices to show the level of the false polarimetric signal for this first-order dependence on the row average. Further additional higher order terms mainly affect the shape of the profiles.

The practical significance of doing this simulation is to get an upper bound on the level of the non-linearities that are tolerable for a particular level of polarimetric sensitivity. In practice, we want to add the complete row average dependence, where the row average

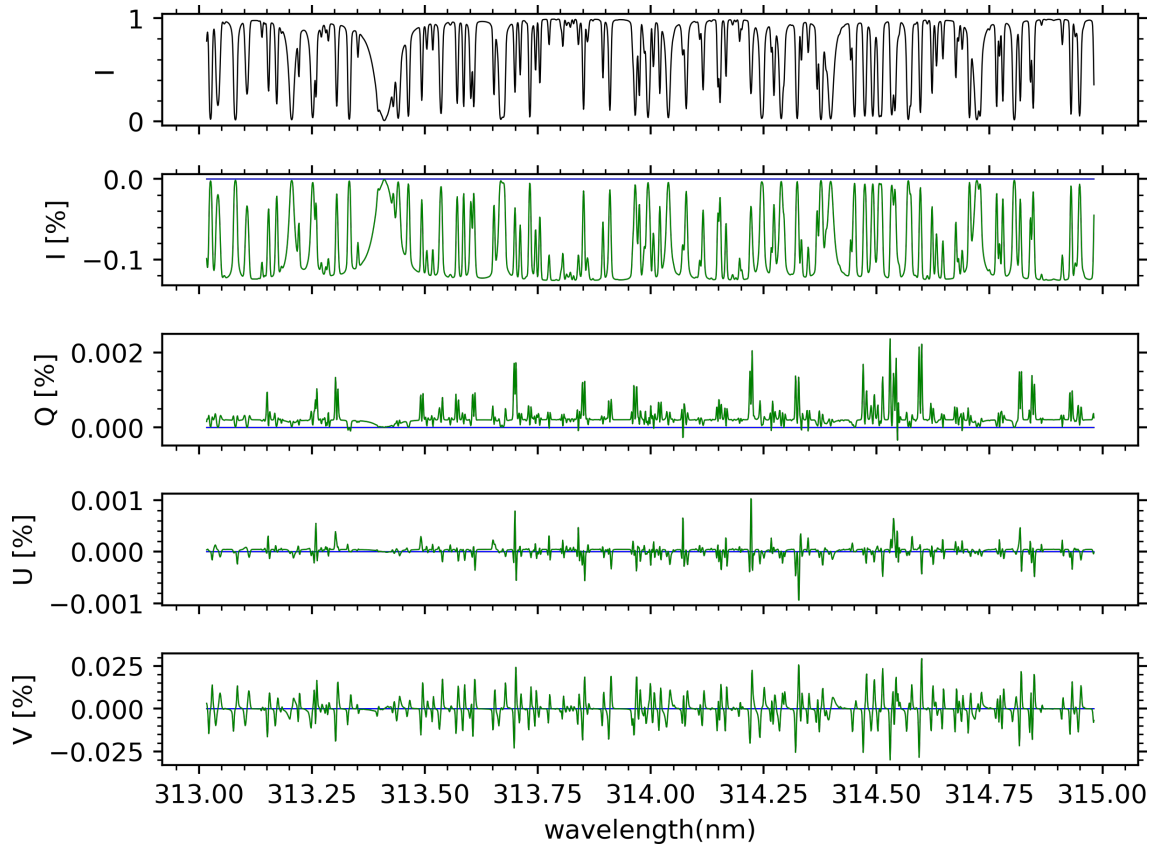


Figure 3.5.: Comparison of Stokes parameters: The green profiles showing the difference from the input for 0.2% row average dependence.

dependence is obtained from doing basic tests using the Triangular Target as described in section 5.2.2. From the first order analysis, we can easily see that to achieve a polarimetric sensitivity of 10^{-3} in units of the continuum intensity, the camera non-linearity (pixel non-linearity and the row dependence) has to be lower than 0.5%.

The sensors provided by the manufacturer have a non-linearity, an order of magnitude higher than the required value. The relevant results are given in section 6.2. Doing these simulations, including all the relevant mechanical effects, we realised that although the camera is a limiting factor in reaching the desired polarimetric sensitivity, other mechanical effects like wobble and jitter in the instrument will take precedence and often limit the sensitivity to 10^{-3} of the signal.

4 An Introduction to Electronic Imaging Sensors

4.1. Light Sensors

The basis of detecting any radiation is its interaction with matter. We can track the electromagnetic oscillations in the microwave and the radio wave regime using an antenna. However, as the frequency increases, making antennas to track electromagnetic oscillations becomes challenging. Thus some other property of light needs to be used. For the visible region of the spectrum, it has been the property of light to initiate the breakdown of chemical bonds that helped develop the plate and the film cameras. The photoelectric effect led to the development of the first Charge-Coupled Devices (CCDs) (Janesick and Blouke 1995, Burke et al. 2007). If we go higher on the energy scale, we encounter the Thompson and the Compton effect and going higher on the scale; pair production is used for radiation detection. These effects have been studied extensively and used as diagnostics for a long time, opening independent fields dealing with them.

We shall be focusing on the visible part of the light-matter interaction. Here too, our primary focus would be on what happens after the light-matter interaction. For example, in the case of the photoelectric effect, reading and localisation of the charge that the incoming photons generate is the part that interests us. This localisation leads to image formation.



Figure 4.1.: A flow diagram showing the different stages of light sensing.

One of the simplest electronic light sensors using the photoelectric effect as its basis is a photo-diode. A diode, by definition, is an electronic element allowing the flow of current in only one direction. Most commonly used diodes these days are manufactured using semiconductors, and these are prone to the generation of charge carriers when light falls on them. Thus for regular diode use, we might want to block the light falling onto the diode, but this also allows for the making of a sensor to measure the intensity of the incident light, as the number of charges generated is proportional to the light illumination of the diode. Thus a photo-diode is a reverse-biased p-n junction. An array of such junctions was the basic principle of initial passive pixel sensors. Figure 4.1 shows the different stages, from photon collection to the final digital signal for a typical light sensor.

4.2. Imaging Sensors

4.2.1. Passive Pixel Sensors (PPS)

Passive pixel sensors are those where the pixel performs one function: converting the incoming photons to charge. Once a certain amount of charge is collected, it is transferred along the rows or columns until it reaches one corner for readout. The main point is that the readout units are not integrated with the sensing units. The potential wells (pixels) are formed by applying an external voltage to p-doped metal oxide semiconductors, thus forming small capacitors. These hold the generated charge; at the end of the charge collection, this charge must be taken off the sensor chip for readout, which is only possible at the physical boundaries of the chip. This restriction means that only a limited number of readout units can be attached and introduces some restrictions on the readout of the sensor. No single pixel can be read out individually. For example, if the readout unit is attached at one of the edges (say vertical edge), then to read a pixel in the centre of the row, all other pixels between that pixel and the readout unit have to be read first.

Thus the time needed to capture an image can be divided into two parts, the photon collection period (integration time or exposure time) and the time needed for the readout of the sensor. The speed of analogue to digital converters (ADCs), and the time needed for charge transfer, determine the readout time. The incremental fashion of readout means that a physical shutter must block the light while we read the sensor to ensure there is no illumination of the pixels while we transfer the charge. This need for a physical shutter introduces a waiting time until all the pixels are transferred and read.

The simplest way to reduce this waiting time is to use faster electronics. The other option is to mask a specific region of the sensor and transfer the generated charge to these masked regions for temporary storage, allowing charge collection in the uncovered region and reading of the covered region simultaneously. The shutter is needed only for transferring the charge in the sensing pixels to the storage pixels. Moreover, we can remove the shutter if the time needed to shift the charge to the storage region is much smaller than the exposure time, thus increasing the charge collection time compared to readout time. We can arrange the masked region to maximise usability for a specific purpose. The most common types of maskings are,

Frame Transfer CCDs: half of the sensor region is masked and dedicated for charge storage. The transfer time must be much less as compared to the integration time or we will have smearing.

Interline CCDs: each alternate column in the sensor matrix is masked. Some bit of the resolution is sacrificed to gain speed (frame read speed). For the same set of readout electronics the smearing of the image is much less, but the read time is longer as compared to frame transfer sensor.

Frame interline: half of the sensor region is masked, in addition to the alternate columns in the sensing region. This tries to solve the smearing and the readout speed problem at the same time.

4.2.2. Active Pixel Sensors (APS)

As the name suggests, the pixels are more complex and can typically convert the generated charge to a voltage at the pixel level. That voltage can be read later (in the readout units at the boundaries), thus allowing reading while integration (charge collection). A critical function of the readout units, charge to voltage conversion, has been transferred to the pixels. Thus no charge needs to be moved, and each pixel can be individually indexed or readout, thus allowing for parallelism. The simplest one is column parallelism; all columns are read out in parallel. CMOS sensors (see Fossum 1997, Gamal and Eltoukhy 2005, and references therein) are an example of active pixel devices.

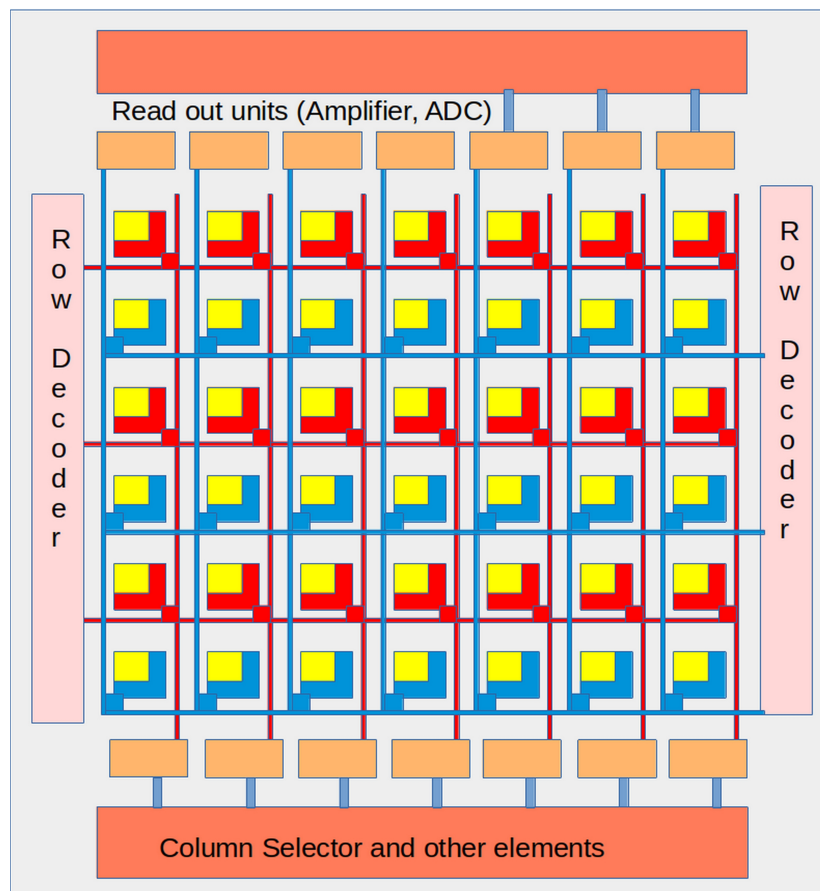


Figure 4.2.: Basic schematics of a column parallel ADC architecture for an active pixel sensor. The yellow regions are the photon collection sites, and the adjacent red and blue region is the accompanying electronics.

Figure 4.2 shows the schematics of a simple APS; the blue and red colours differentiate between the odd and the even rows. One set of pixels gets connected to the readout electronics located in the upper region of the chip, and the second set to the lower one. These two readout electronics will not be identical for typical sensors, leading to variations between odd and even rows. Furthermore, although all columns are read out in parallel, each has a different readout unit; hence, all columns will have a different response, and thus will give rise to additional fixed pattern noise often at a level higher than that reached by CCDs.

Shutter

For most applications, it is desired that the image sensor captures a true snapshot of the observed scene; that is, all pixels are exposed simultaneously and with the same exposure time. A mechanical shutter is required for image sensors with charge transfer to stop the light from falling on the sensor during the reading process and emptying the pixels, ensuring the same exposure time for all pixels. In CMOS sensors, we need to reset the pixels after they have been read. This process can be done on a row-by-row basis, commonly referred to as a rolling shutter. Alternatively, all pixels could be reset simultaneously, using a global shutter, before starting the integration for the next frame. Each functionality comes at the cost of the electronic complexity of the pixel. These two types of shutters have their own advantages and disadvantages:

Global shutter: all pixels have the same time information, would perform better for still image applications.

Rolling shutter: as different rows are reset at different times, the start and end of the charge collection are shifted for the rows. Thus each row has different time information. For typical use cases, this time shift in the rows is much smaller than the exposure time and the period between two consecutive frames; thus, all rows can be considered to have the same timestamp. For the same ADC architecture it will typically be faster as compared to a global shutter, and would perform better for video camera applications.

4.2.3. Analog to Digital Converter (ADC)

ADC architecture (see Leñero-Bardallo et al. 2014, for a review) is also an interplay between speed, accuracy, and complexity/size. If we had to use one ADC to read a complete sensor like in initial CCDs, then the ADC's speed and the charge transfer speed would effectively determine the maximum frame rate the sensor can achieve. Parallelism can help reduce the load on one ADC; thus, we can increase the frame rate for the same ADC speed. In the case of CMOS sensors, where there is no charge transfer across pixels, we can increase the frame rate by increasing the speed of the ADC. Below we describe some of the most general types of ADC used in image sensors. We describe the basic design of the ADC, not the electronic architecture required to achieve the final result.

Column-Parallel Single-Slope ADC The most straightforward way to convert an analogue signal to a digital signal is a voltage ramp generator coupled with a comparator and counter. A comparator compares the input voltage at its two input terminals and gives an output. The ramp generator generates a voltage, increasing with each clock cycle, and at each step, this ramp voltage is compared with the input signal. Once the ramp voltage goes over the input signal, the counting stops, which is the final digital signal.

Column-Parallel Two-Step Single-Slope ADC The digitisation process takes place in two steps (Hwang et al. 2013, 2014), coarse and fine. A fast ADC with a high ramp slope does the coarse digitisation. The thus obtained digital signal is converted back to analog; the difference between the converted and the original signal is treated as

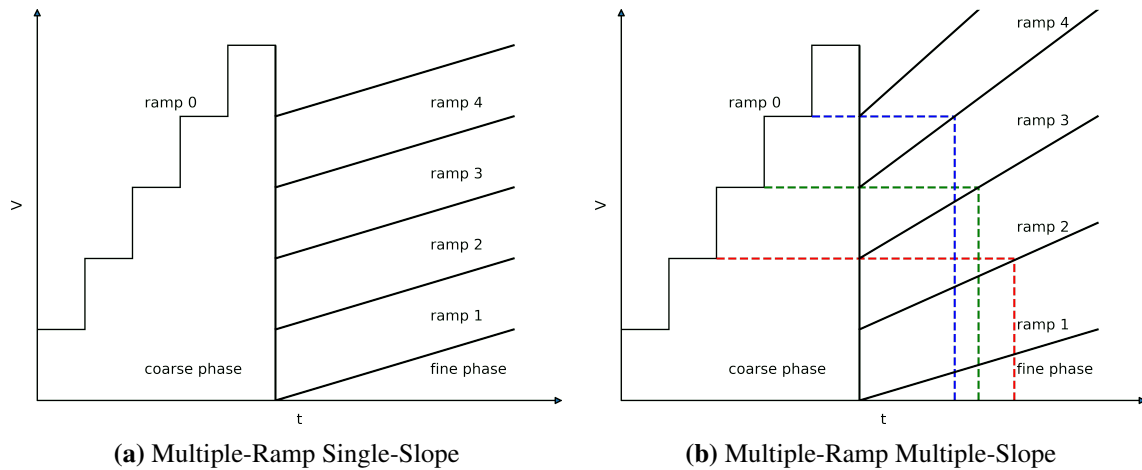


Figure 4.3.: The timing diagram for the MRSS and MRMS ADC architecture. The coarse phase is the same in both cases, a high-speed, high slope (value of the Least Significant Bit, step size for the ramp) ADC. The fine phase fills the gap between the steps with smaller steps (smaller slope, smaller LSB). MRMS uses ramps with slopes increasing with photon shot noise (Snoeij et al. 2007a).

the signal for the fine phase of digitisation. As the range of values to be digitised in the fine phase remains the same, a single voltage ramp and slope is used for conversions in the fine phase.

Column-Parallel Multiple-Ramp Single-Slope ADC (MRSS) Here too, the digitisation process takes place in two steps, coarse and fine. This one differs from the previous scheme because although all the ramps used in the fine step have the same slope, they have different starting and ending points. Depending on the output of the coarse step, an appropriate ramp is chosen for the fine conversion. Figure 4.3a shows the ramping structure for the respective ADC architecture (Snoeij et al. 2007a,b).

Column-Parallel Multiple-Ramp Multiple-Slope ADC (MRMS) In this case, the different ramps have different slopes (Snoeij et al. 2007b) that take advantage of the photon shot noise increasing with the increasing number of photons falling on the pixel. The slope of the voltage ramps is different depending on the signal level; the higher the signal, the higher is the slope of the voltage ramp being used for analog to digital conversion, figure 4.3b.

Figure 4.4 shows the comparison of the photon shot noise with the quantisation noise (see section 4.4) of the ADC. The quantisation noise increases with an increasing slope of the ramp. In terms of image quality this ADC would be comparable to MRSS, as long as the quantisation noise is lower than the photon shot noise, but would be faster. The time required for conversion in the fine step would decrease with the light level, as can be seen from the coloured vertical lines in figure 4.3b.

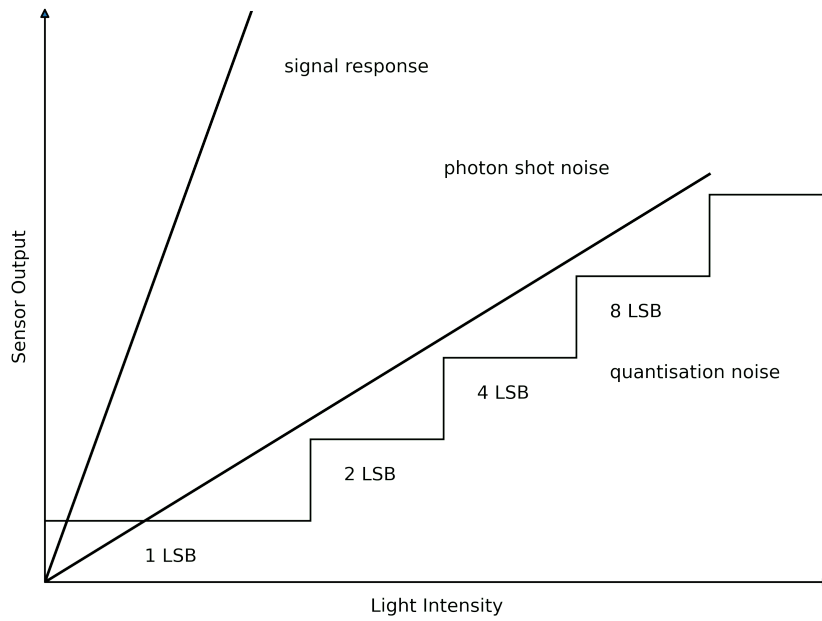


Figure 4.4.: Quantisation step increasing in a MRMS ADC, to take advantage of the increasing photon shot noise, (see section 4.4 and Snoeij et al. (2007a,b)).

4.3. Non-Linearity in Imaging Sensors

We can try to write a simple expression for the response of the pixel to the light illumination (ll) as

$$f(ll) = f_i(ll) + f_{pxnl}(ll) + f_{sc} + noise, \quad (4.1)$$

with,

$f_i(ll)$ denoting the linear component of the dependence on the light illumination for the pixel,

$f_{pxnl}(ll)$ the non-linear component of the light level dependence of the pixel,

f_{sc} denotes the pixel cross-talk.

Here we assume that some form of thermal stabilisation has been used to remove the temperature dependence, or else we would have contributions from a temperature function.

4.3.1. Pixel Non-Linearity

Pixel non-linearity is primarily because of the design of an individual pixel, related mainly to the photon to charge conversion and charge storage in the pixel. Writing a simple expression for the digital signal for a simple ADC we would have

$$DN(\text{Digital Signal}) = \text{floor}\left(\frac{g \times n}{V_{LSB}}\right), \quad (4.2)$$

where g is the gain term, n the number of photons falling onto the pixel, and V_{LSB} the voltage corresponding to the smallest value used for the ADC conversion.

Gain Non-Linearity The g term includes conversion gain (see Beecken and Fossum 1996, Bezawada et al. 2007, Bohndiek et al. 2008), a factor relating the number of electrons generated to the number of photons falling on the pixel, and all other gains before digitisation. This is similar for all pixels, but not the same, as although all pixels (photon collection area, and accompanying electronics) are made of the same material, the sensor wafer might not be homogeneous across the entire sensor. This gain term is non-linear, and for most sensor applications, we try to choose a regime where it is primarily linear, trying to maximise the practical range. However, for specific applications, it can be made non-linear, generally done to increase the system's dynamic range.

ADC Non-Linearity A simple ramp ADC should be linear by design, but not all electronic elements perform flawlessly. And some of these repeated, stable wrong counter steps contribute to a non-linearity in the scale developed for the ADC. While the non-repeatable, unstable steps contribute to the noise. An inherently non-linear ADC would be the MRMS, although it is still an accumulation of linear steps. All two-step or multi-step ADCs are an aggregation of these linear steps, and problems would occur where these steps meet. These regions are most prone to missing counts in an inadequately designed system and the regions with the most certain digital number for the signal in a carefully designed scheme.

4.3.2. Pixel Cross-Talk / Scene Dependent Behaviour

Pixel cross-talk is primarily an effect of the arrangement of the pixels and the resources they share. In the case of the initial CCDs, it was the charge blooming or overflow where the charge of one pixel would flow to the nearby pixels. In the case of APSs, it is the electronic cross-talk among the readout units. A study of similar effects in CCDs and its impact on astronomical data is presented by Boone et al. (2018).

This cross-talk is related to the arrangement of pixels or the readout units, and hence one of the primary steps when trying to determine this cross-talk is to try and determine the architecture of the sensor. As the arrangement of the pixels would give a specific directionality to these effects. For instance, if it is known that pixels along a row share specific resources, we can try to look at the scene dependence on a row-by-row basis, similar to what is done by Gamal et al. (1998) for Fixed Pattern noise (see section 4.4 for different kinds of noise). We will see this directionality in all sensors having column level parallelism.

Thus f_{sc} (pixel cross-talk) is in general a complicated function of all the pixels of the sensor. For a test pixel (pixel we intend to study, and calibrate) with constant illumination, it can be expressed as

$$\begin{aligned}
 f_{sc} = f_{sc}(ll, \text{row pixels}, \text{column pixels}) &= f_r(\text{row pixels}) + f_c(\text{column pixels}) \\
 &+ f_{r*c}(\text{row pixels}, \text{column pixels}) \\
 &+ f_{r*l}(ll, \text{row pixels}) + f_{c*l}(ll, \text{column pixels}) \\
 &+ f_{r*c*l}(ll, \text{row pixels}, \text{column pixels})
 \end{aligned} \tag{4.3}$$

for the case where resource sharing is along the two preferred directions, rows and columns, respectively. The different terms of the equation are:

$f_r(\text{row pixels})$ and $f_c(\text{column pixels})$ are just functions of the pixels in the same row and the column as our test pixel, respectively.

$f_{r*c}(\text{row pixels}, \text{column pixels})$ is a convoluted function of both row and column pixels at the same time. These are constant functions, independent of the illumination of the test pixels.

$f_{r*i}(ll, \text{row pixels})$ and $f_{c*i}(ll, \text{column pixels})$ are a convolution of the pure row and column pixel dependencies with the light level of our test pixel.

The last part, $f_{r*c*i}(ll, \text{row pixels}, \text{column pixels})$, would be a convolution of all three, the illumination of our pixel, and the row and column dependencies.

For most of the current sensors where each row is read at a time, having column level parallelism, the equation may be simplified to

$$f_{sc}(ll, \text{row pixels}, \text{column pixels}) = f_r(\text{row pixels}) + f_{r*i}(ll, \text{row pixels}). \quad (4.4)$$

The easiest way to look for scene dependent effects is to compare a uniformly illuminated sensor with a non-uniformly illuminated sensor. One point to clarify is that this is different from fixed pattern noise. Fixed pattern noise would not be seen in this comparison unless it has a dependence on illumination. In that case, it would be in the higher-order component of the fixed pattern noise. For diagnostics, the most straightforward approach we could come up with was to ignore the terminology and consider all of these sources as one, and everything would come up as different components of the fitting function.

An example of the comparison for the scene dependent behaviour has been shown in figure 4.5. We took an average of 100k images to make mean images, and then compare the mean images for the two cases. Panel (a) of figure 4.5 shows the average of the slant target while panel(b) displays the average of the flat illuminated frames. The gradient in the always illuminated region of the comparison image of slant over flat illumination, is the non-linear effect we intend to study.

Taking the cut along a column, for different light levels we get figure 4.5d, where the colours represent the corresponding row in the selected column in figure 4.5c. The lowest point of the coloured curves in the figure indicates the range of this non-linear effect to be up to around 2% of the average illumination.

In our case each column seems to have an independent ADC, and one row is read at a time. Thus it makes sense to describe the effect in terms of the properties of the row, and the value of the pixel. One of the simplest ways to take into account the statistics of the row is to consider the average value of the row, and something that relates the row characteristics to the pixel. The number of simultaneous conversions taking place i.e. the number of pixels having the same value, is one such parameter.

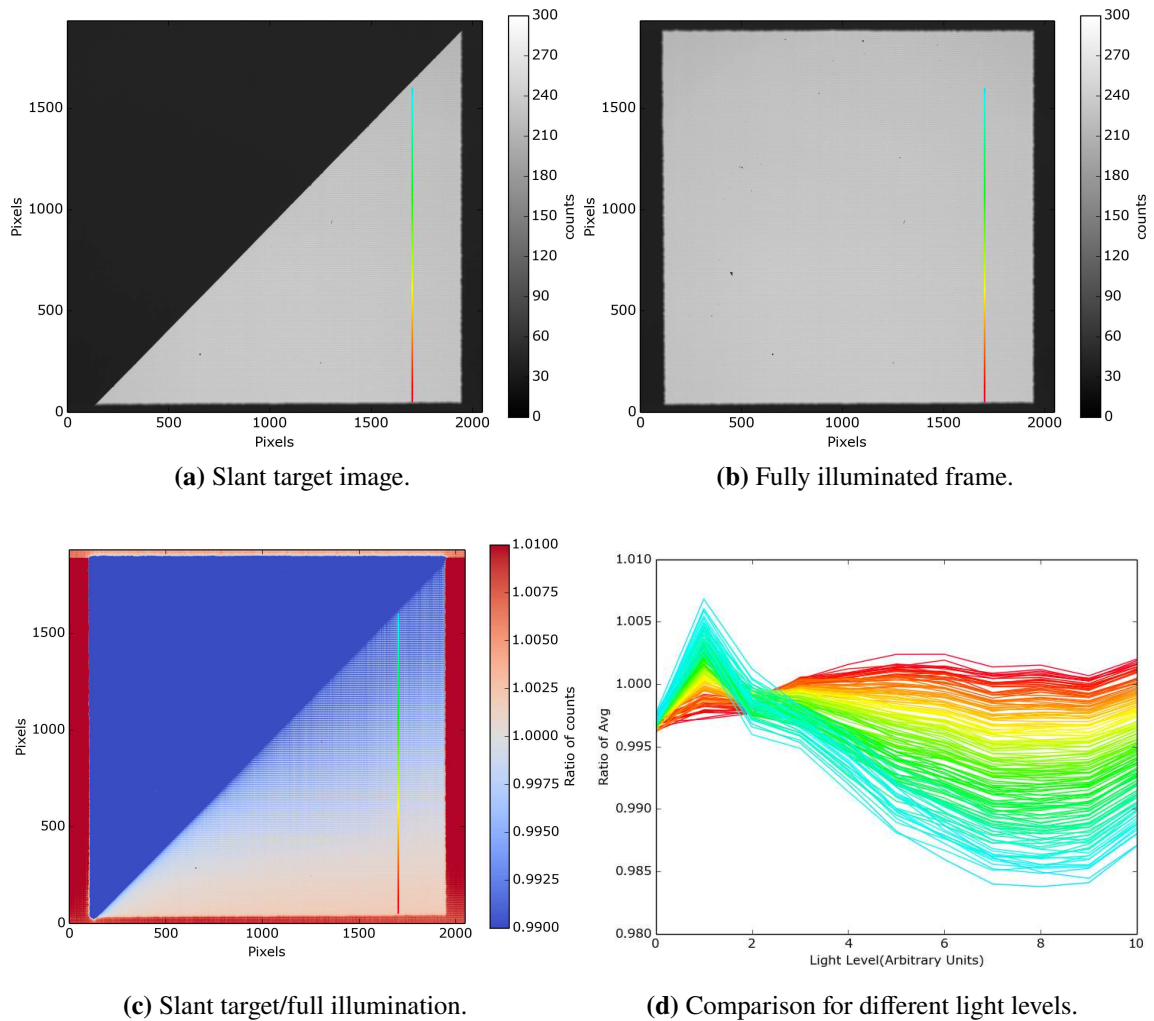


Figure 4.5.: Comparison of slant target with a flat illumination. Where (a) is the image of a slant target, (b) is the flat illumination for comparison, and (c) is the ratio of (a) and (b). The rainbow colour in (d) corresponds to the pixels in the vertical column as marked by the rainbow line in the (a), (b) and (c).

4.4. Noise and its Sources

Photon Shot Noise Even for a single light level the number of photons falling on a pixel will have a certain distribution, this is an inherent source of noise in any kind of light detection system.

Pixel reset noise Once a pixel has been read, or the charge has been converted to voltage for sensing, the pixel needs to be cleared of that charge. This process is never perfect, and hence the random left out charge adds to the signal in the next frame, thus adding to the noise in the pixel.

Thermal Flicker Even without photons falling onto the sensor there will be electrons generated in the sensor, and this will have a distribution of itself, adding to the noise.

Quantisation Noise Going from a continuous regime to a semi-continuous regime, in-

roduces an uncertainty to the value of the signal lying between two steps. This is unavoidable for any kind of ADC, thus counted as noise in the final digital signal.

Fixed Pattern Noise As suggested by the name it is a time independent pattern, formed on the sensor, mainly due to offset (device mismatch, dark signal non-uniformity) + photo response non-uniformity. Given that it is fixed in time, once known it can simply be removed. In Column parallel sensors, the most common manifestation is the vertical curtain fixed pattern, but given that photon response of each pixel is also a component, the vertical curtain is not the only manifestation.

4.5. Additional Sensor Problems

Intra Pixel Effects These are mostly related to where in the pixel, the centroid of the image of a point source lies. Most camera manufacturers try to circumvent this problem by putting a microlens array on the pixels; this maximises the effective area of photon collection for a pixel.

Intra Frame Time Variation Illuminate the sensor using a light pulse, with the pulse width smaller than the whole integration time. Shift this pulse in the integration time to change when the electron is generated in the pixel. For an ideal sensor, this shifting will not have any effect on the value of the sensor. However, when it does, it further adds to the complexity of the calibration process. For our purpose, we shall be neglecting it.

Inter Frame Variation Resetting the pixels was not perfect; thus, an imprint of the previous image is seen in the next. This is easy to identify, illuminate the sensor using a short light pulse, and then capture the time series of the frames.

We must account for all the problems mentioned above while using the cameras for scientific use cases.

5 Calibration Setup for CMOS Imaging Sensors

For an ideal imaging sensor, the value of a pixel depends only on the amount of light falling on the pixel. Thus the only parameter of importance would be the light level. The pixel's digital value (DN) could have a linear or non-linear monotonic dependence on the amount of light falling, but that would be the only parameter to be calibrated. Problems start to arise when the DN of a pixel depends on something other than the pixel's illumination. However, provided that the sensor response is at least stable and reproducible, we can attempt to characterise it carefully and use that information to apply post-factum corrections to the acquired data.

5.1. The Parameter Space

The relevant parameters that affect the pixel count (apart from the pixel illumination) are listed below.

Temperature of the sensor, and readout electronics.

Response stability of modern electronic circuits is mostly a matter of thermal stability. Therefore, a pre-requisite for this to be successful is a modification of the commercial camera packages with precise temperature control of any components upstream of and including the analogue to digital converters.

Average power consumption of the sensor.

The sensor requires power to operate. Voltage bias or potentials must be maintained to confine charge and for the ADCs to function. As the power consumption of the ADCs increase, the bias levels typically drop, resulting in a change in the DN of the pixel. We use the average value of a row as a proxy of this power consumption when a row is being read.

Cross-talk between pixels

The number of pixels having the same digital count in a row, hereafter also referred to as siblings is considered as a proxy for this pixel cross-talk. Here we consider that each row is read at a time, and the cross-talk is only between the pixels in a row.

The cameras characterised in this thesis are already equipped with a temperature stabilisation system, and only the last two parameters are considered variable parameters in the following text.

Before we go ahead and look at the parameter space, let us go through some terms that will be often used in the following text.

Calibration region or test region:

Is a part of the sensor we want to correct for the non-linearities.

Control region:

All of the sensor regions, except the calibration region, can be used to change the different parameters (row average and siblings). The parameters will be varied by changing the shape and illumination of the control region; this will be discussed in the following text.

Deductive targets:

These targets block a part of the incident light in certain areas of the sensor.

Additive targets:

These targets add more light (more than the calibration region) to the control region of the sensor.

Siblings or Number of simultaneous conversions:

Pixels having the same digital count in a row. In the following text, whenever we talk about changing the siblings, we essentially mean that we change the allowed number of siblings for a pixel.

Scene dependence:

The term scene dependence ideally would encompass all kinds of variations of different illuminations of the sensor; however, in this text, this term will refer to the row average and the siblings' dependence whenever we cannot separate the two.

Parameter Space Containing Row Average

The first scenario here is to add one more parameter to the light level, which is to consider the average power consumption of a sensor during readout. In the case of row by row readout, we take the average value of the row as a proxy for power consumption. The parameter space for a pixel, thus formed, is shown in figure 5.1.

The green region is always accessible; we can always decrease the row average while keeping a constant value for the test pixel simply by covering the other pixels in the row. Moreover, this is the regime that deductive targets can cover. For the simple case of a single deductive target (select anyone in figure 5.1), we go along one of the allowed lines as we change the light level. The slope of the lines is related to the number of pixels illuminated in a row, which gets fixed once we choose a deductive target.

In order to probe the blue region in this figure, we need to have additive targets, where we add extra light to the row, keeping the test pixel at a constant illumination. This allows us to have a row average larger than the pixel count. The lines in figure 5.1 correspond to one target, as shown in the subfigures, while we change the illumination in the calibration region. The figure is easy to understand once we select a target (sub-image in the figure)

and move along the x-axis in the figure.

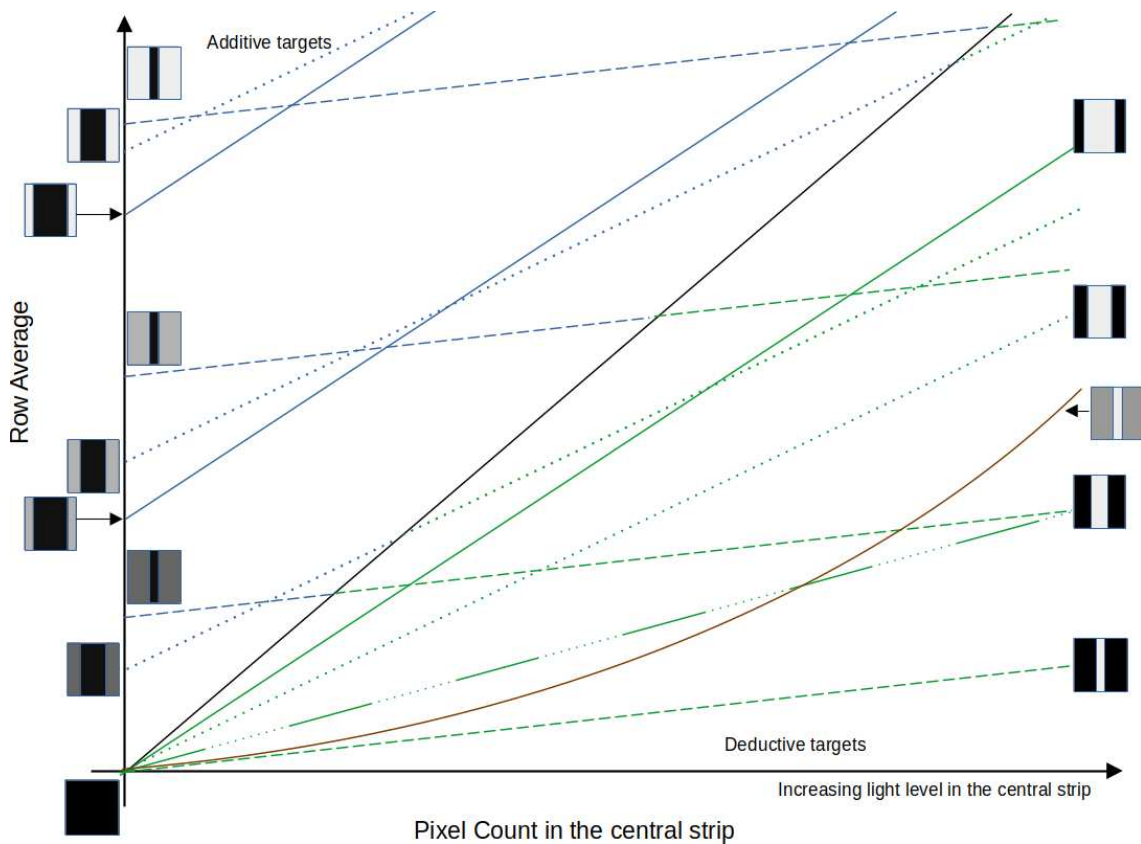


Figure 5.1.: Qualitative illustration of Parameter space covering row average and light level, **green** always accessible, **blue** only accessible using additive targets. The mini-figures show the target configuration, and different types of lines identify the respective slopes for the different targets as the light level is increased. The brown curve is for a target with 50% transmittance in the blocked region and is a representative curve for translucent targets.

Parameter Space Containing Row Average and Siblings

The second case is to add the third parameter, the number of simultaneous conversions for a pixel. We now have a three-dimensional parameter space comprising the light illumination, row average and the siblings. It is easier to look at two-dimensional cuts of the entire space; figure 5.2 shows one such two-dimensional cut for one light level. It shows the parameter space covered by the row average and the number of simultaneous conversions for a test pixel.

The region in green can be covered using deductive targets, while we need additive targets to cover the region in blue. The vertical line separating the two regions depicts the value of the pixels in the calibration region. The red region can never be accessed, whatever may be the target configuration. To see why this region is not accessible, let us choose one point in the red region. For simplicity, let it be a point with many siblings, high

on the Y-axis. Most of our pixels are in the calibration region (or, for simplicity, let us say they have the same illumination), determining the row average. Thus, the only possible values for the row average are those close to our test pixel and the vertical separation line or the simple case of a dark frame, which would be on the extreme left in figure 5.2. For an illumination without counts distribution in the calibration and control regions, the separation line between the accessible and not accessible regions (separation line between red and blue and red and green region) would be close to linear. This separation line would be non-linear for a non-homogeneous illumination or any illumination having a distribution.

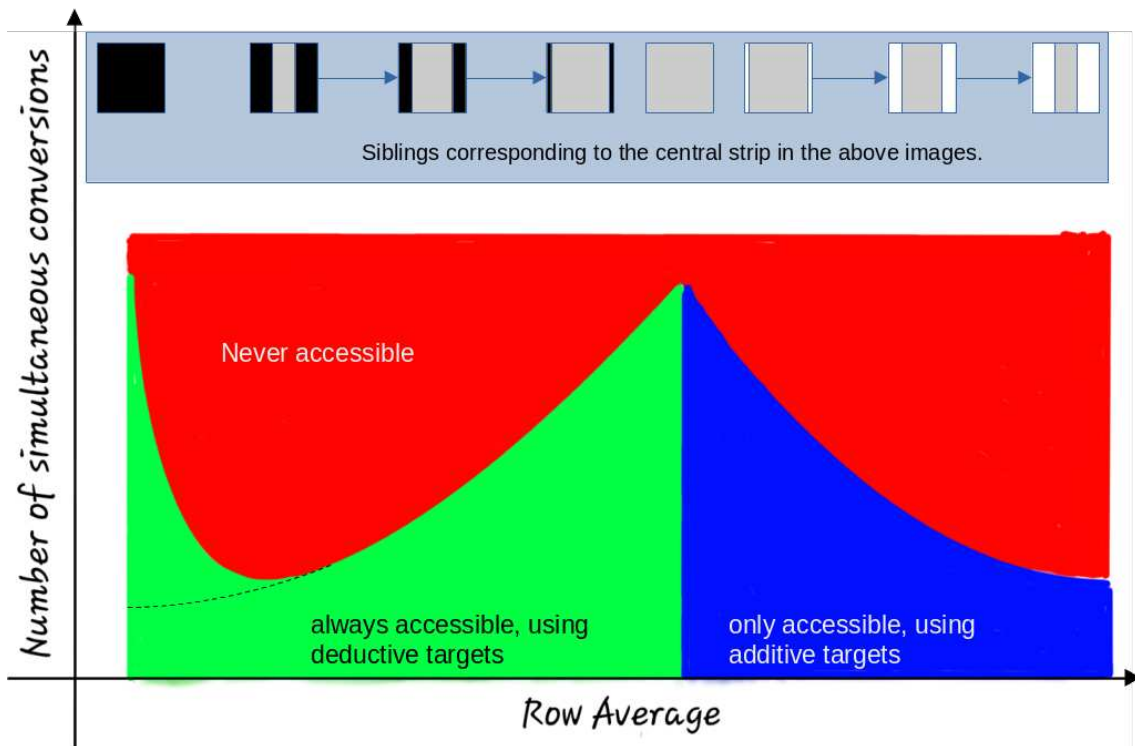


Figure 5.2.: Qualitative illustration of target space covering row average and the number of simultaneous conversions, with the green region being always accessible and the blue region only accessible using additive targets, as in Figure 5.1. While the red region is never accessed. The figure is a two-dimensional cut of the three-dimensional parameter space.

The fundamental problem with studying the dependence of the different parameters lies in the independent control of the parameters. Practically, it means how to control/change the row histogram while keeping a constant illumination for the calibration region. Changing the number of siblings in the calibration region is easy; cover a part of the calibration region and change the number of illuminated columns. The only problem is that it changes the row average as well. To keep the row average constant, we must control how many pixels in a row see a particular intensity.

As in figure 5.3, we can start with two different light levels illuminating the row or a two-peak histogram of the row (apart from the peak for masked pixels, shown in black).

The subfigures show the different scenarios for the histogram of a row under different illumination conditions. The first possibility is to move along the vertical columns in figure 5.3. The only thing possible there is to move pixels from one peak to the other, with the light level and the positions of the two peaks being fixed for all subfigures lying along a column. It means moving the pixels from the calibration region to the control region while the illumination remains unchanged. However, this simultaneously changes the row average and the number of siblings. The first column in figure 5.3 shows this behaviour for a simple deductive target. The peak for the non-illuminated region falls on the peak for the masked region (the portion of the row always non-illuminated, as described in section 5.2.1).

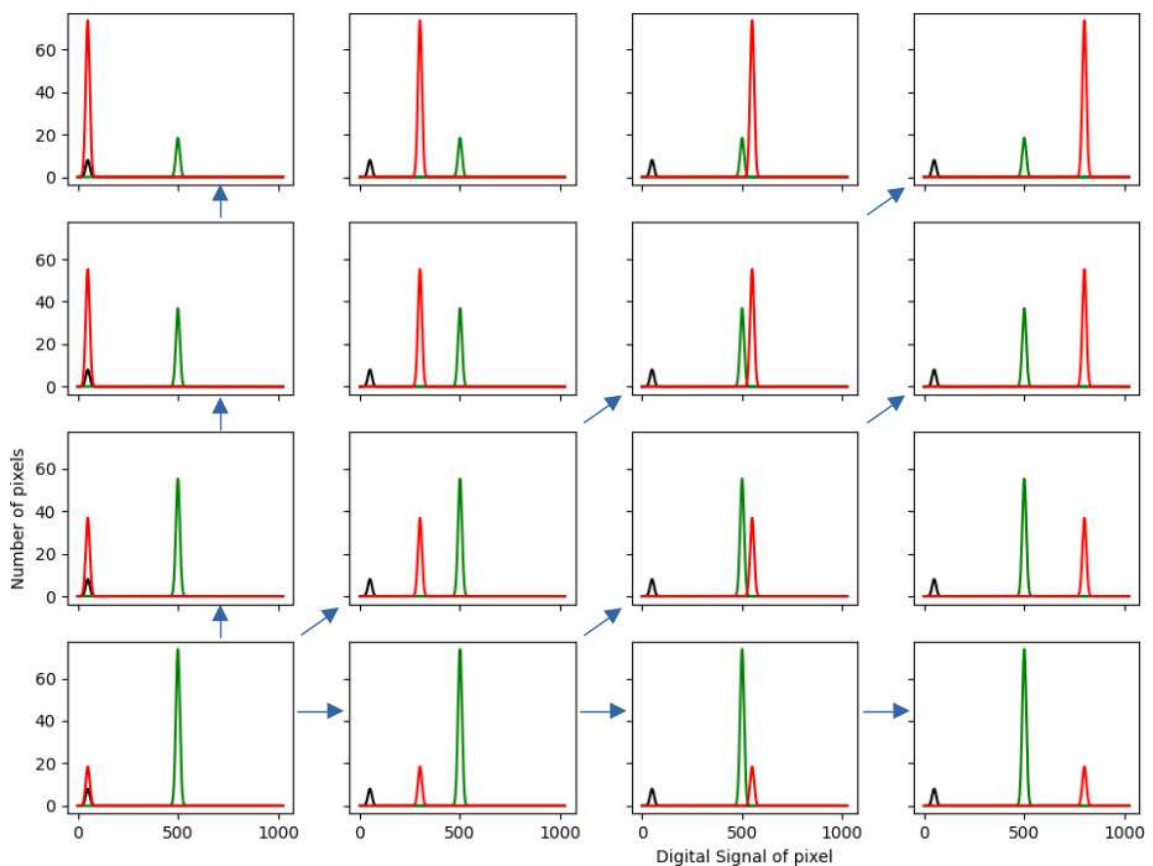


Figure 5.3.: Qualitative illustration of Two peak row-histograms, covering the entire parameter space. With peaks in the histogram corresponding to the calibration region in green, the control region in red, and the masked region in black. Moving horizontally in this figure, we change the row average, keeping the siblings in the calibration region fixed. While moving vertically, we change the number of simultaneous conversions in the calibration region. A diagonal movement left to right would vary the siblings independent of the row average.

To change the row average, keeping the siblings constant in the calibration region, we need to shift the peak for the control region (in the row histogram), as shown in the horizontal rows in figure 5.3, but that needs an independent illumination of each region (control and calibration region).

For deductive targets, the next possibility is to have three peaks in the histogram (or three levels of illumination); figure 5.4 shows this. We can keep the solid red peak unchanged and play with the two dashed red peaks in the histogram to change the row average. This keeps the number of siblings in the calibration region constant while we independently change the row average, possible with translucent deductive targets. One set of actual targets allowing this is shown in section 5.2.4, figure 5.11.

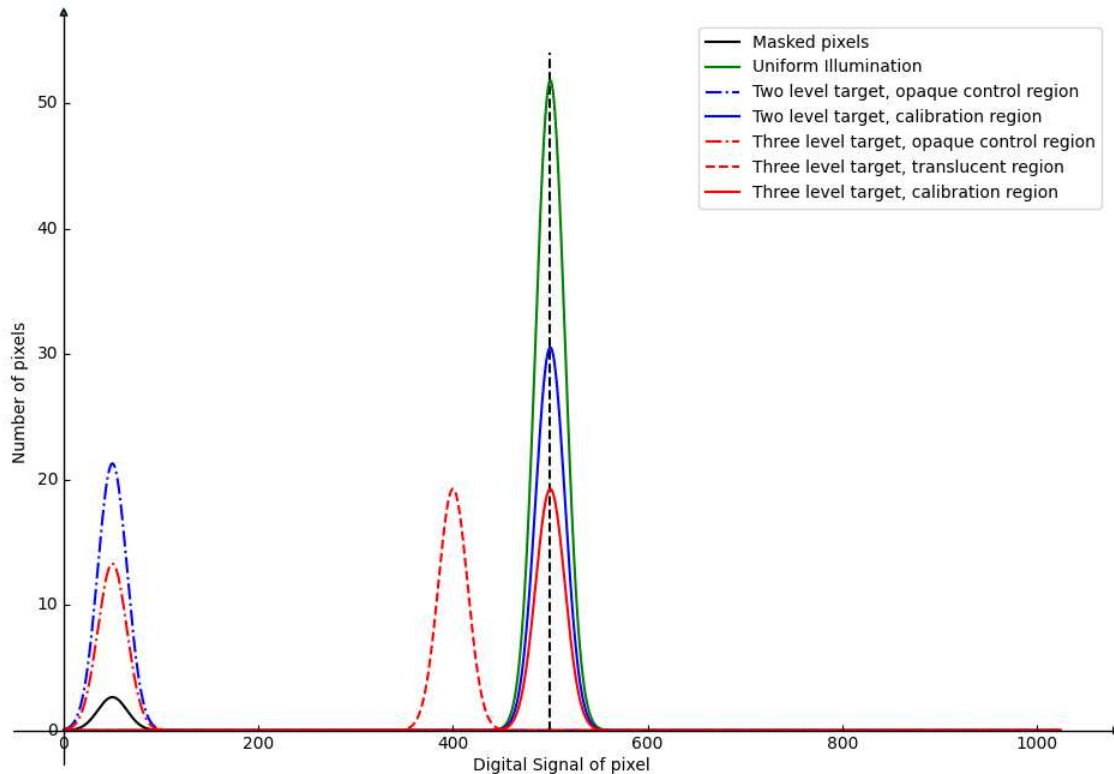


Figure 5.4.: Row histogram for two (blue profile) and three-level (red profile) deductive targets, with reference to a uniform row illumination (green profile).

However, being able to change the parameters independently does not mean that we can access the entire parameter space, and deductive targets only allow the flow of pixels (in the row-histogram) to the left of the peak for the calibration region. Thus only allowing row average lower than the count of the test pixel. This does not cover the cases shown in the two columns on the extreme right in figure 5.3.

Figure 5.5 shows all the target configurations required to cover the entire parameter space (except the red region) in figure 5.2 for one light level. The central strip in the mini-figures is the test region or the calibration region, and the side strips are the control regions. Ideally, we would like to make this target space as dense as possible, but data storage and analysis constrain what we can achieve. This target space is just for one light level, and for a complete calibration, we would have to do this for different light levels (the primary parameter). One can easily see that the time and storage needed for collecting this data are difficult to handle for a standard lab; some calculations are shown in Appendix A.

Furthermore, doing this for multiple cameras adds to the data volume.

Thus the main conclusion is that we need to change the row histogram, keeping the peak for the calibration region fixed in position, shape and size.

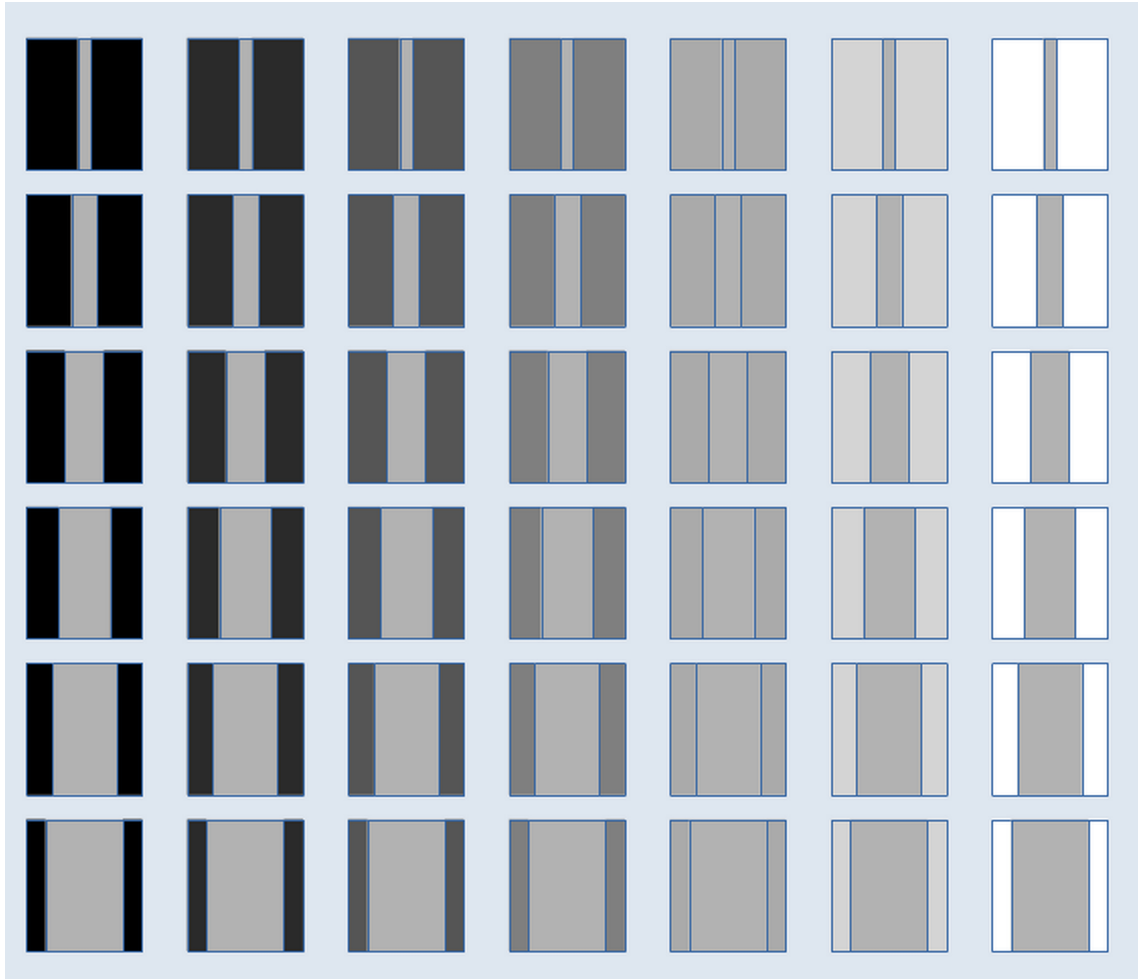


Figure 5.5.: Target space covering row average and siblings space for a single light level in the calibration region. The central region is the calibration region, and the outer flanks are used for control of the row average and siblings.

5.2. Study of Targets

The term target was used very restrictively in the above sections, considering we only had a single row in the sensor and wanted to calibrate it. The parameter space for a row can be accessed using a set of targets projected onto the camera sensor. We show specific physical targets and the information they provide about the sensor. Most of our targets are made of a plain sheet of anodised aluminium (standard light-shielding material used in the lab), as shown in figure 5.6. The reason for using a simple sheet of aluminium is that

it can be cut into any desired shape using a surgical knife, and primarily because we need the targets to be thin to avoid any reflections from the edges of thick targets.

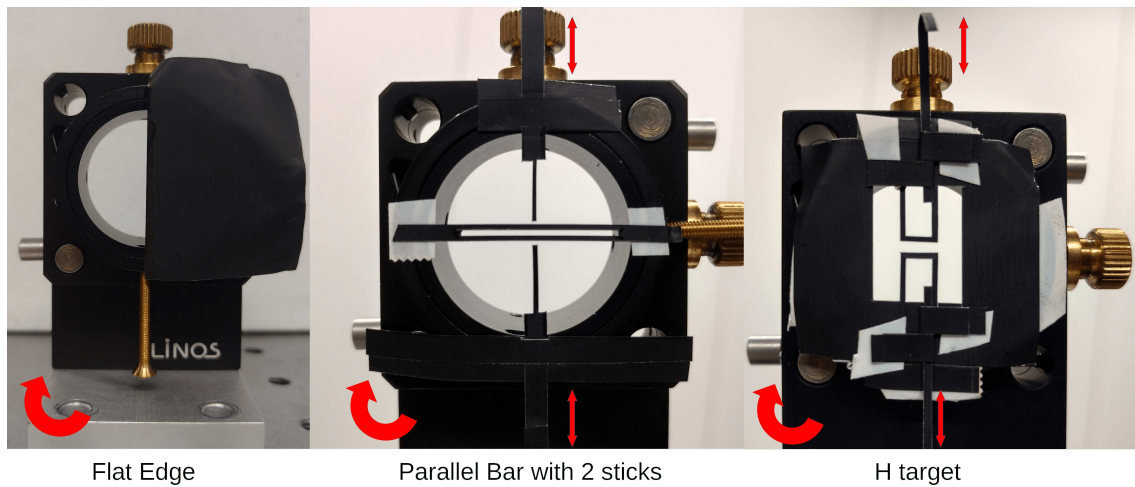


Figure 5.6.: Example targets; the red arrows indicate the movements or configurations allowed in the target.

5.2.1. Masking Sensor Edges

Although not strictly a target, this is essential for probing the camera. A mask is attached right in front of the sensor, shielding a certain number of pixels on all four sensor edges. These shielded pixels on the edges act as reference pixels to detect the change in the dark level due to the sensor illumination. As these pixels need to be always dark, the mask needs to be dark (opaque and non-reflective) and added as close to the sensor as possible and wide enough to provide some dark pixels even if stray light seeps along the edges of this mask. The ideal solution would be for the camera manufacturers to mask some working pixels while still allowing them to be read out. However, this will not solve the whole problem, as we potentially only read a part of the sensor to increase the frame rate (possible for CMOS sensors). These masked pixels at the sensor edges will not be read, so a configurable mask is needed. The right and the left masked pixels will be referred to as "bands" or "shielded pixels" in the following text.

5.2.2. Triangular Target

Triangular Target on Flat Illumination The triangular edge is one of the essential targets to project onto the sensor. The basic idea is to cover half of the sensor. Instead of covering the sensor vertically or horizontally, we cover it diagonally. Doing this has a slight advantage because we get the information about the prominent direction of the scene dependent nonlinearity. The complete test requires a set of flat illuminated and dark images for reference, which is the case for most studies that can be done by projecting targets onto the sensor.

We compare the target image with a flat illumination for the same light level (ratio or difference). If the gradient of the change (compared to the reference) in the always

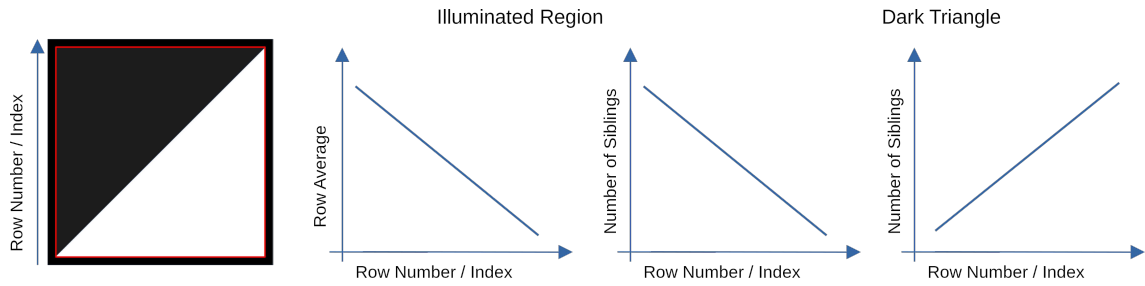


Figure 5.7.: Qualitative illustration of a Triangular target on a uniform illumination of the sensor, the red square on the images marks the region of interest. The two middle columns show the variation of the row average and the number of simultaneous conversions w.r.t the row number in the illuminated triangular region. The last column shows the variation in the number of simultaneous conversions in the dark triangle.

illuminated part of the sensor is mainly in the vertical direction, then it can be assumed that each row is read one at a time while the columns work in parallel. It will be the reverse if this gradient is mainly along the horizontal direction. If the gradient of the change from reference is mainly perpendicular to the edge of the triangular target, then either the target is not well focused on the sensor or some reflections from the target add into the always illuminated region. Hence, we recommend using non-reflective targets. If there is no dominant direction to the change, then either the readout is highly multiplexed, or the light level changed slightly during the measurement of the flats and the target.

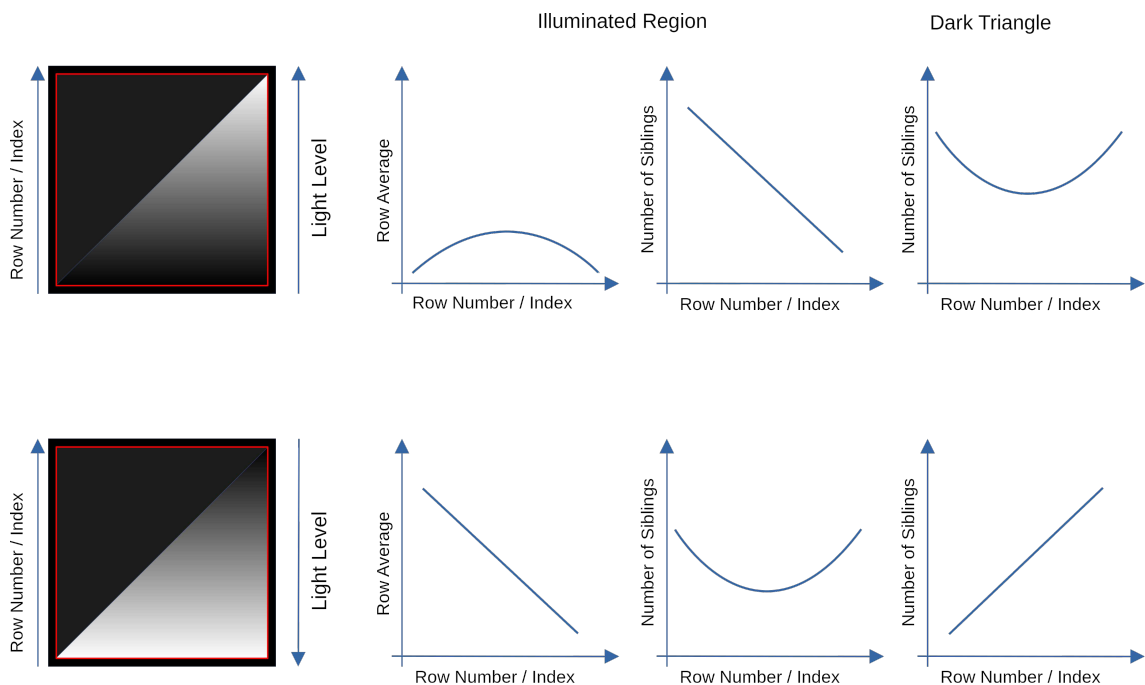


Figure 5.8.: Qualitative illustration of a Triangular target on a gradient illumination of the sensor, the red square on the images marks the region of interest. The two middle columns show the variation of row average and the number of simultaneous conversions w.r.t the row number in the illuminated triangular region. The last column shows the variation of the number of simultaneous conversions in the dark triangle.

Although a triangular target gives most of the information about directionality and the level of the cross-talk, the physical target can be rotated to cover half of the sensor vertically or horizontally to be sure that the gradients in the case of the triangular target area are actually due to cross-talk or nonlinearities.

Triangular Target on Gradient Illumination The point to note here is that the illumination does not need to have a gradient. A camera with a rolling shutter will show similar behaviour, as shown in figure 5.8. The figure shows the variation of the row average and the siblings in the two regions (bright and dark). And then, under the assumption that all rows or pairs of rows behave similarly, we can take the row number as a proxy of the light illumination and study the effect of sensor illumination on the count of the masked pixels as will be shown in section 6.2.

5.2.3. Bar Target

We project a dark bar onto the sensor. It can be vertical or horizontal depending on the primary direction of the scene dependent effect (determined using the triangular target). For the case of column parallelism, the dark bar is aligned parallel to the columns, vertical in this case, as in figure 5.9.

Projecting this target on the sensor means that each row has a similar illumination (and row histogram). Furthermore, given that the same set of electronics reads each alternate row, ideally, all alternate rows should show a similar scene dependent effect in the dark bands (shielded pixels). This is critical if we want to assume that all rows are similar. This assumption is not bad, given that most cameras on the market have the same set of electronics reading each alternate row and follow this architecture or its derived version.

The other thing to check is the ratio of the target image and the dark image in these dark bands (marked in yellow in figure 5.9). Ideally, the pixels in all the bands would show a similar ratio when compared to a dark image, but if that is not the case, then the sensor has some directionality issues in each row as well. We see this effect in the cameras used for SUSI, where the banding effect is different in shielded pixels on the left and the right edge of the sensor, see section 6.2.

Parallel Bar Target One of the extensions to the single bar target is using a target with multiple bars. The target should allow us to change the density of the bars. There are two tests that can be performed using such a target. Comparison of two targets having a different density of bars but having a similar row average, as in the left vertical panel of images figure 5.9. The second test is to keep the density of the bars fixed but to slightly shift the target perpendicular to the bars, as in the right vertical panel, figure 5.9. These two tests allow us to determine if there is any effect of the position of these dark bands on the counts of the test pixels (always having similar illumination conditions and can be bright or dark).

These targets are ideally a derivative of a more fundamental target, which is the projection of a diffraction and interference pattern on the sensor. The interference pattern from

a double slit is similar to the target shown in the bottom left panel of figure 5.9. Ideally, it would provide more accurate information, as the intensity profiles can be matched with the theoretically calculated ones. The only limitation is that the illumination setup requires a narrow band source capable of homogeneously illuminating the whole sensor.

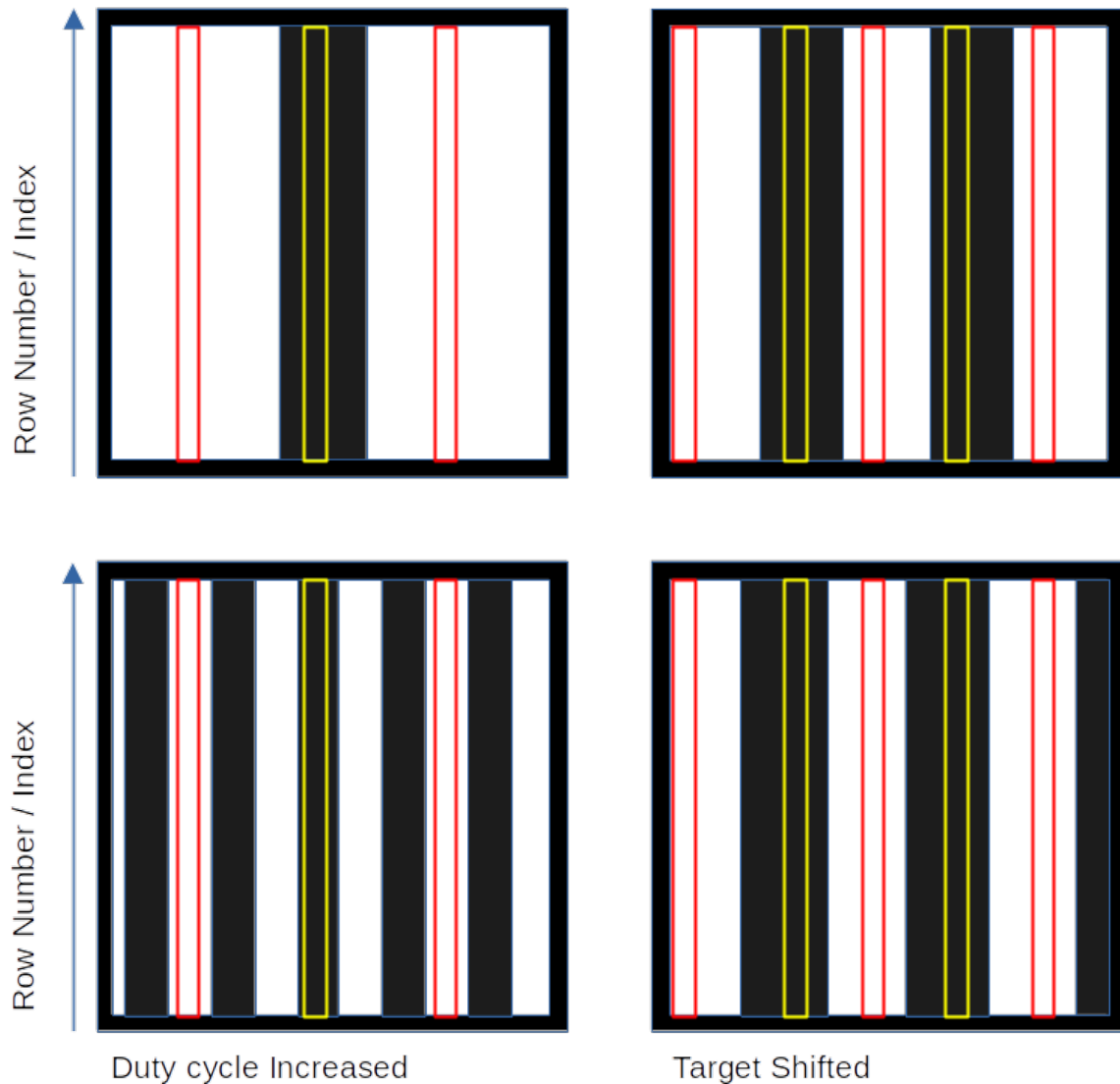


Figure 5.9.: Bar test: the red regions are marked for tracking change in the always illuminated region, and the yellow regions for tracking change in the always dark region.

Parallel Bar and 2 Stick Test In case there is still doubt about the sensor showing a scene dependent effect, a comparison between this target and a flat illumination would confirm the presence of a scene dependent effect. The middle panel in figure 5.6 shows the actual target used for this test. Figure 5.10c shows the difference of the two images on the left in figure 5.10, $(c)=(a)-(b)$. Ideally, the central white vertical strip should not have shown that small blue block. It is only because of the dependence of the pixel count on the row average that we see some difference in the rows covered by the two horizontal sticks.

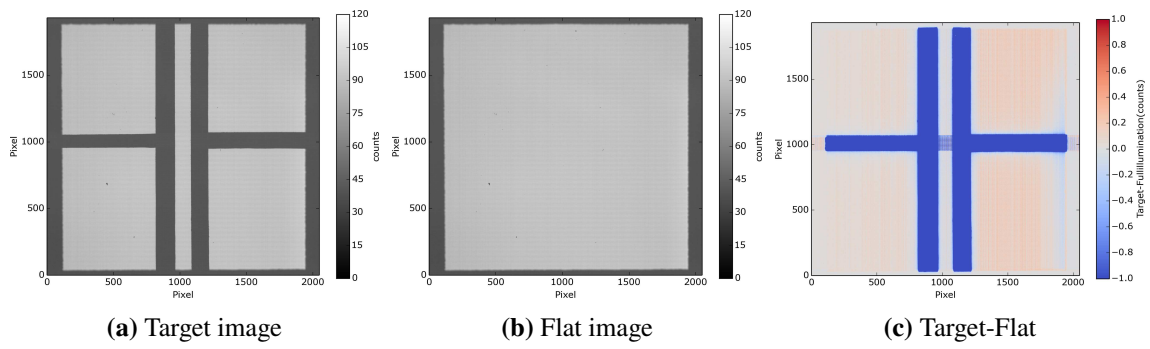


Figure 5.10.: Parallel Bar and 2 Sticks test

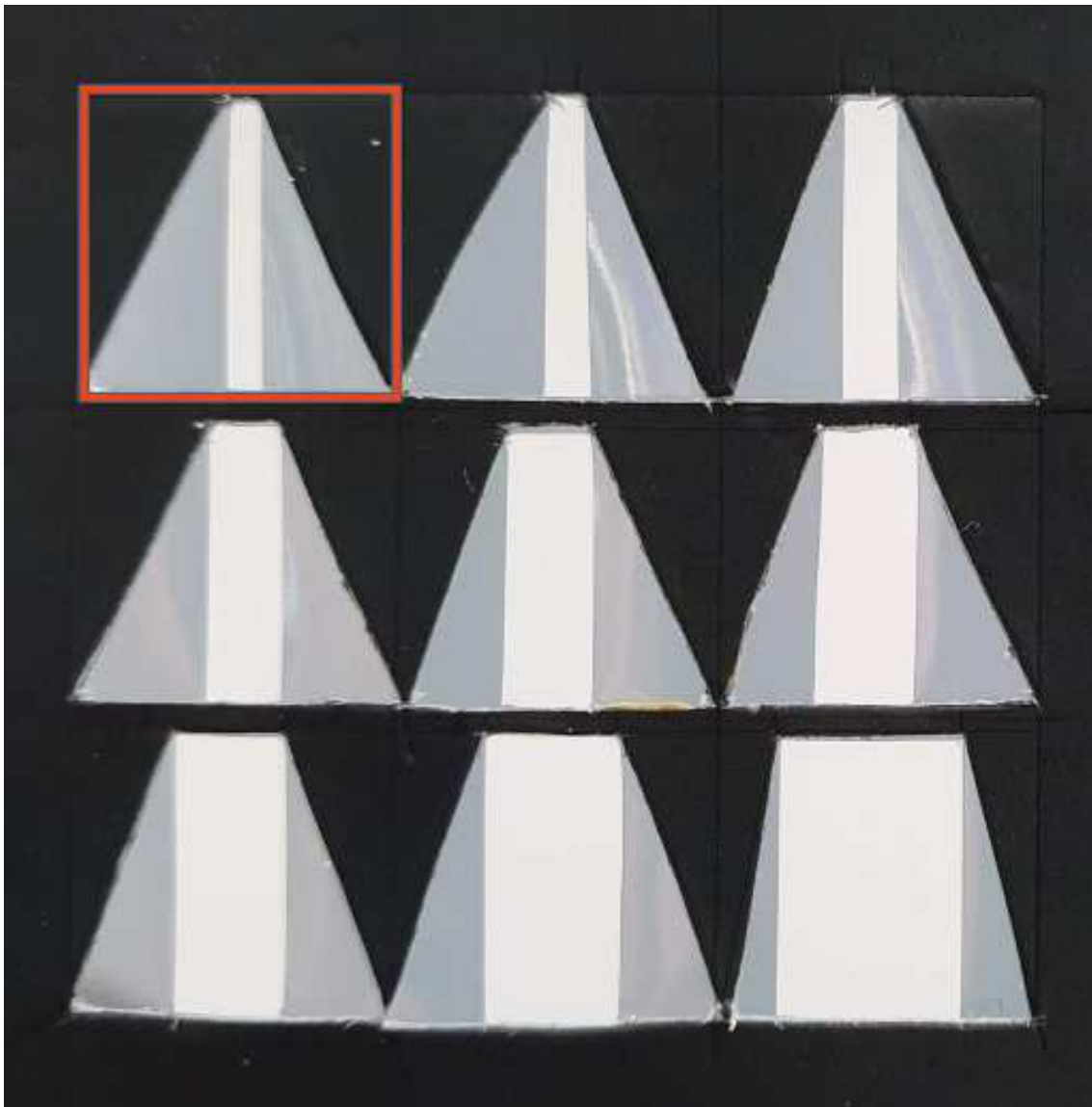


Figure 5.11.: An array of three light level targets, for independently varying the siblings and row average, with the red square marking the boundary of one target. The width of the central region controls the number of siblings. The dark slanted target controls the row average.

5.2.4. Multiple Light-Level Deductive Targets

The targets we studied till now are all two-level targets; apart from the dark shielded pixels, there are two regions with two different illuminations on the sensor: the calibration region and the control region. However, these two-level targets cannot independently control the row average and the number of simultaneous conversions. As already discussed in the context of figure 5.3.

Moreover, figure 5.4 shows a histogram for three light-level targets. One sub-target in figure 5.11 shows how to change the row average keeping the same number of siblings in the calibration region (constant width of the central region, under the assumption of homogeneous illumination). As the width of the translucent part changes, the position of the peak corresponding to the translucent region in figure 5.4 shifts.

Changing the width of the central strip changes the number of siblings. Thus shifting between the sub-targets allows us to independently change the number of siblings and row average while keeping a constant illumination in the calibration region, assuming that all rows or pairs or rows behave similarly.

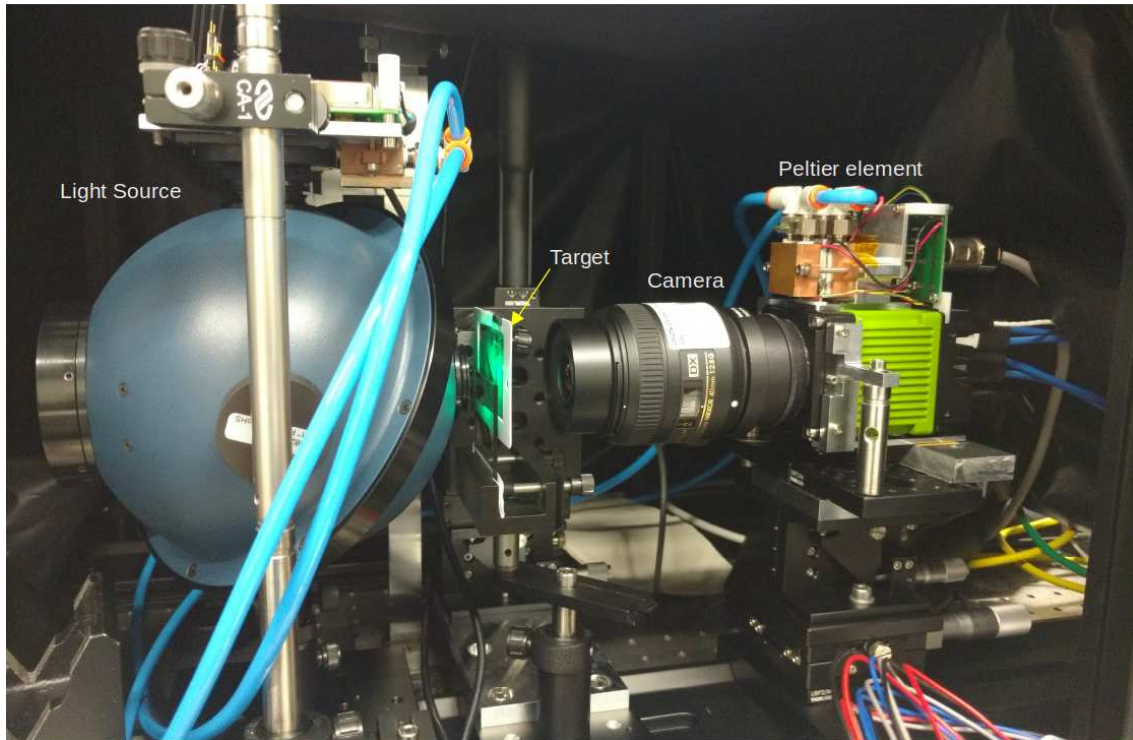
5.3. Setup

The setup is based on the type of calibration needed and the effects we suspect to play a role in the pixel output and want to probe. We discuss two setups, a preliminary one used for the most basic testing and light level calibration and an evolved version of the same that accounts for the parameter space discussed above and aims to expose the camera to some extreme illumination conditions.

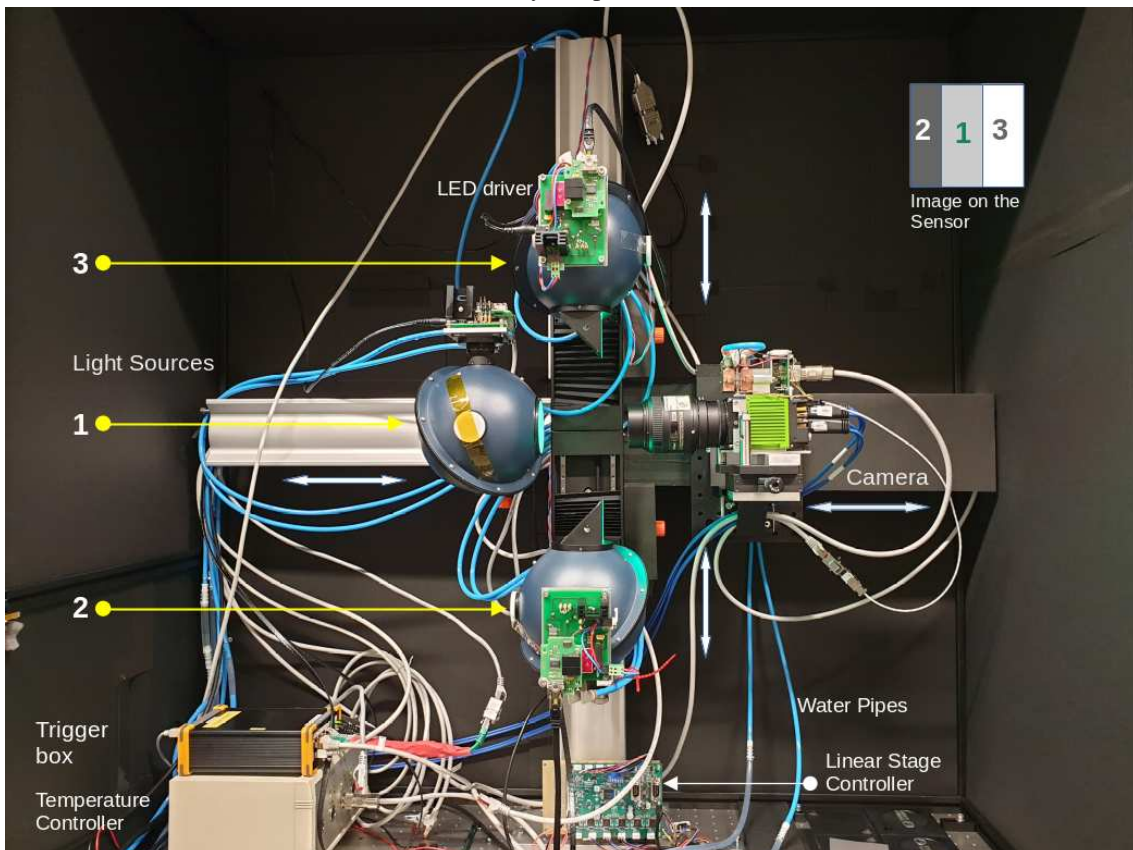
Preliminary Setup For a simple light level calibration of the light sensor, the setup required is a homogeneous light source with a known or quantifiable light output and the camera, as shown in figure 5.12a. We say it is a basic calibration because if there were no scene dependent effects or pixel cross-talk, this would take care of any pixel non-linearity. One can easily discard the assumption of treating all pixels as identical.

Given that the number of electrons generated per photon depends on the sensor's temperature, we might have to stabilise the camera thermally (as has been done here, blue water cooling pipes in figure 5.12a) or add another calibration parameter, but that is all we need. The camera's temperature stabilisation and cooling are better because it gives some control over the thermal flicker.

Independent Illumination Setup However, we need a slightly different setup for scene dependent effects since we need to create different scenes on the sensor. The easiest way is to go with deductive targets; block some part of the light falling on the sensor. The problem with deductive targets is that we would never be able to access the entire parameter range using them as described in section 5.1 (we discuss the targets in section 5.2). For that purpose, we will need a setup that can independently illuminate certain regions of the sensor. The setup shown in figure 5.12b is an example.



(a) Preliminary setup for calibration



(b) Three-sphere setup for camera calibration. The numbers indicate the light sources and the corresponding illuminated region on the sensor, as in the subfigure on the top right.

Figure 5.12.: Camera Characterisation Setup

The two light sources numbered 2 and 3 independently illuminate the sensor's control regions. At the same time, the central integrating sphere directly (numbered 1 in the figure) in the beam path illuminates the calibration region.

The following sections describe each of the setup elements in more detail.

5.3.1. Light Source

The light source in the final setup contains a 3W LED mounted on an integrating sphere. The LED is driven using pulse-width modulation. This means the sensor's illumination can be changed just by changing the width of the pulse, and the pulse can be synchronised with the trigger for the camera.

Let us look at how we can control the number of charges generated in a pixel. We can either increase the number of photons falling onto the pixel in a unit of time or collect the photons for a longer time. As a change of the camera timing parameters might also affect its response properties, the cameras are operated at an instrument-specific, fixed frame rate with fixed exposure time and light level control is done as follows.

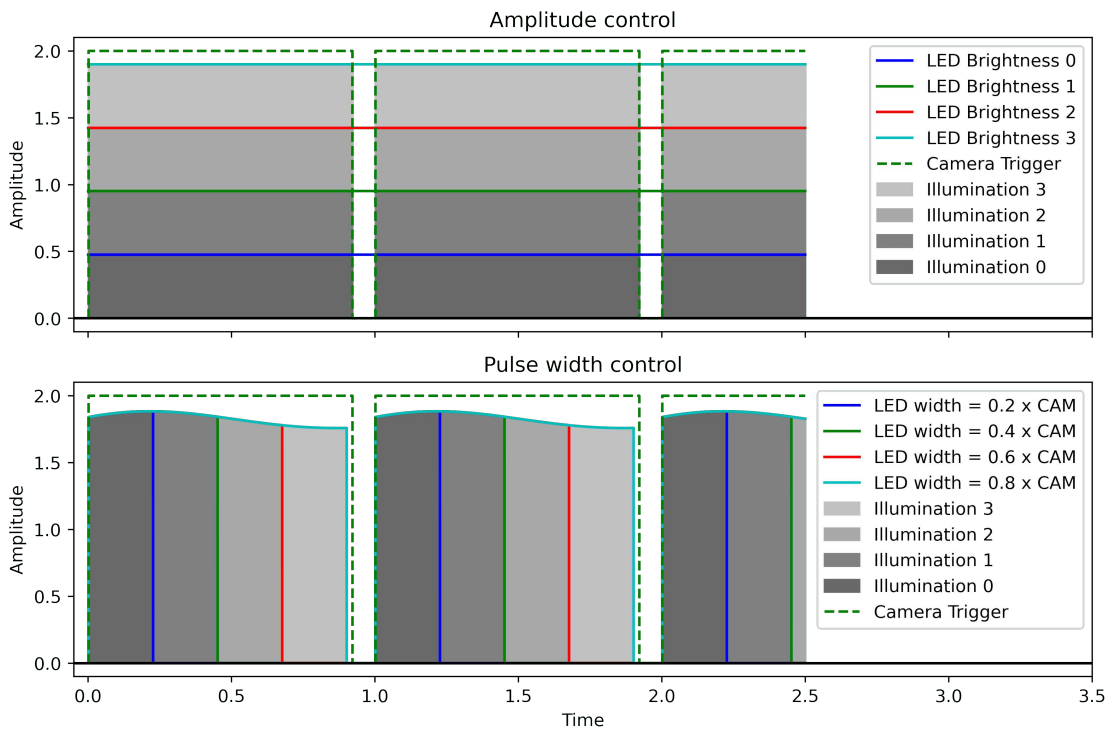


Figure 5.13.: Illumination control of a pixel. Top figure: LED brightness being changed by changing the current driving it. Bottom figure: changing the LED-ON time. The different colours represent the changing brightness and pulse width of the LED. The dark to light grey colour gradient shows the increasing illumination of the camera.

For a light source synchronised with the camera, there are two degrees of freedom for illumination control (we remove the distance dependence). The first is the source's brightness, and the second is for how long that source is active or the duration of overlap

of the LED-ON time with the exposure window. Below we describe three different ways of illumination control and their respective problems.

5.3.1.1. Changing Current

For the case of an ideal light source, the number of generated photons is a function of the current flowing through the LED package, but that is not guaranteed to be linear. Hence, the only way out is to calibrate the light source itself with respect to the driving current of the LED (given we can change the current linearly). The top panel in figure 5.13 shows this case when the LED is just continuously ON and has reached thermal stability. We change the current for the next light level and wait for the LED to reach stability again. Different colours of the horizontal lines correspond to different LED brightnesses.

5.3.1.2. Pulse Width Modulation

The problem with the inherent non-linearity of the source can be removed simply by driving the LED at a fixed current and voltage setting and controlling the *average* illumination via the ON/OFF time of the LED. This requires synchronising the start of the camera exposure with the LED start time. Ideally, this gives control over the light illumination. However, we would still have to consider the shape of the LED pulse, as seen from the LED pulse shape (curvature of the shaded region) in the lower panel in figure 5.13. The different colours of the vertical lines correspond to different LED-ON times.

Thermal Stability of LED Independent of the method used for the LED control, if we change either the current driving it, or the time for which the LED is ON, we will have problems with the thermal stability. A change in the switched ON time of the LED changes its temperature and hence the brightness. A change in the current driving the LED changes the power consumption of the LED and hence its temperature; thus, the resulting brightness would be different from a linear dependence. One solution would be to thermally stabilise the LED, which should help in keeping the LED's brightness constant at one pulse width. However, it is not guaranteed to be linear. On top of that, we would still have to take care of the LED's start-up effect and wait until it achieves thermal stability whenever we change the LED's current or pulse width.

Figure 5.14 shows the mean count of the sensor with time for a specific pulse width of the LED. The two runs were taken on two different days. It is clear that although the curves would settle to the same light level on average, it would take a finite time for the LED to reach thermal stability. Furthermore, that means the data acquisition process would be long (calculations for the time required for data collection are given in the Appendix B).

The effect of cooling (to $\sim 10^{\circ}\text{C}$) the LED is easily seen in the comparison time curve, as seen in figure 5.15. One point is to see how fast the LED stabilises in intensity after cooling. Without cooling, the stabilisation time is on average 45 minutes, while the same comes down to below 10 minutes with cooling. The time needed for stabilisation changes depending on the intensity of the LED, with a longer time required for higher driving currents and longer pulse widths. The cooling of the LED and the driving electronics also

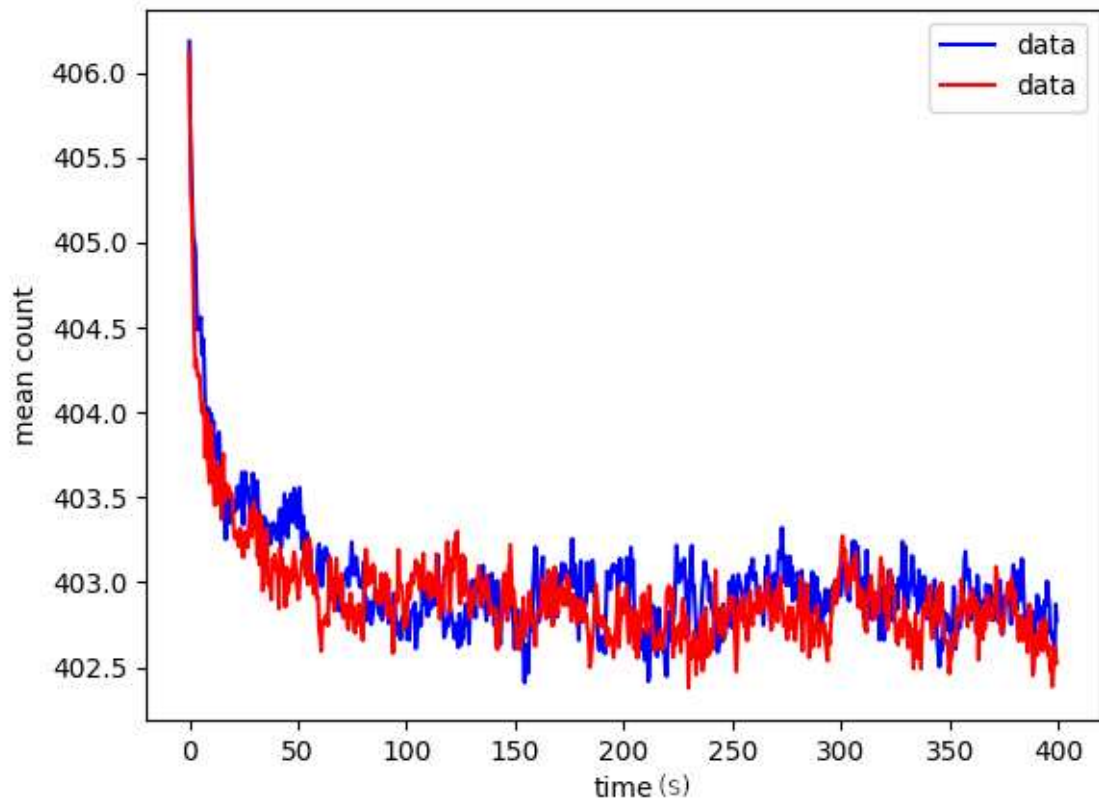
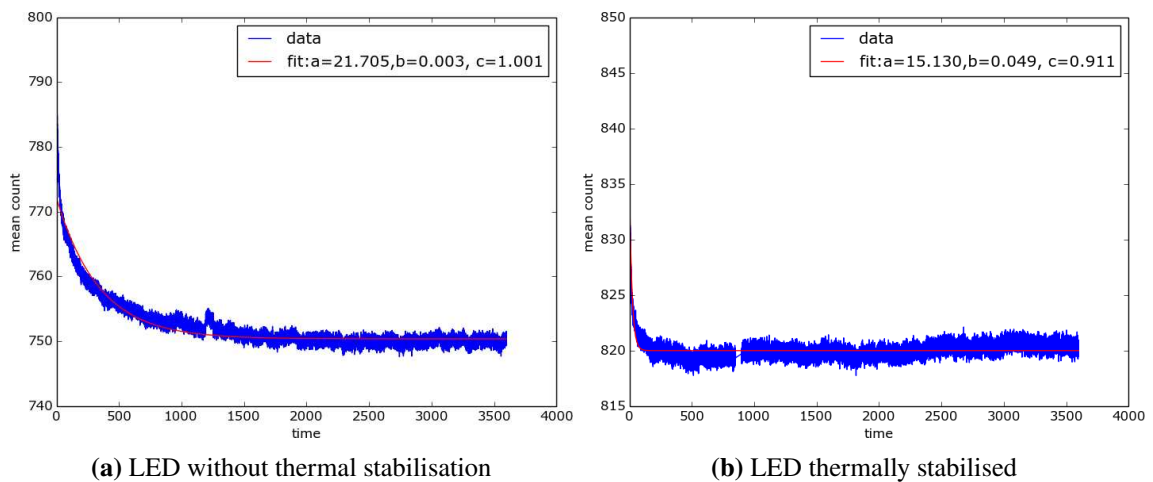


Figure 5.14.: Time series for two different runs of the LED on two different days, obtained by averaging complete frames.



(a) LED without thermal stabilisation

(b) LED thermally stabilised

Figure 5.15.: Frame averaged camera count as a function of time(seconds); for the two cases, the LED with and without thermal stabilisation. The red coloured profile is a fit to $f(x) = a \times e^{-bx} + c$.

changes the maximum intensity of the LED for the same driving conditions, as can be seen from the vertical axis in figure 5.15. For general use case we cool the LED to $\sim 18^\circ\text{C}$, which is the temperature of the water cooling loop used for the camera.

5.3.1.3. Phase Shift

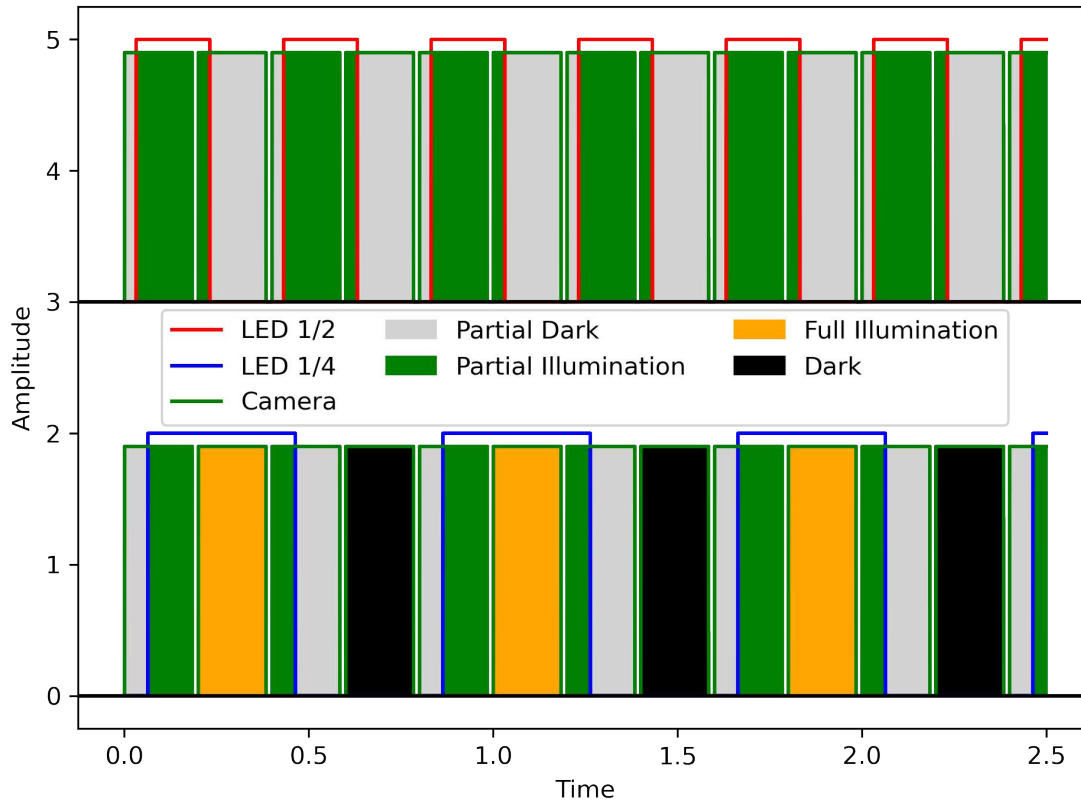


Figure 5.16.: Illumination control using phase shift between LED and camera, with time and amplitude in arbitrary units.

There are specific ways to get out of the waiting problem for thermal stability; a feedback loop for the LED is one option, and the other is to drive the LED at a constant current, voltage and pulse width. Changing the illumination becomes a problem then. The way out is to change the amount of overlap between the LED-ON state and the camera exposure window by introducing a phase lag between the camera and the LED trigger. Figure 5.16 shows the phase lag scheme for illumination control, where the green shaded region is the effective illumination, and the white region enclosed under the pulse is the partially dark part. This can be achieved by running the LED at a frequency going as $1/2n$ of the camera frequency. The number of frames going to waste for each frame considered for calibration (partially illuminated frame, where illumination can be controlled) increases as n increases, and we want to reduce that wastage. Hence one would be inclined to go for $n=1$, as shown at the top of figure 5.16. The $n=2$ case is not that bad and has a slight advantage, as it gives an entirely dark and illuminated frame. The dark frame can be used to check for any thermal fluctuations during the experiment and the setup's

stability. At the same time, the fully illuminated frame can be used as a reference. The two partially illuminated frames can be used for calibration once the LED pulse shape is known completely; in that case, the camera and LED pulse only need to be shifted up to half the LED pulse width.

Timing Jitter There was a small amount of drift seen in the timing sync mechanics, and this came up as a sawtooth pattern in the time series of the mean count of the frames. Figure 5.17 shows the same jitter in the dark frames for the phase shift control of illumination when the LED was running at half the frequency of the camera. Only a small phase shift of ($30\mu s$) was given to test for jitter. This allowed for the possibility of the rising edge (second frame, partially dark, top figure 5.16) of the camera and falling edges of the LED to be in proximity and within this time range of $30\mu s$, and the change in the mean count of the frame gives the measure of the timing jitter.

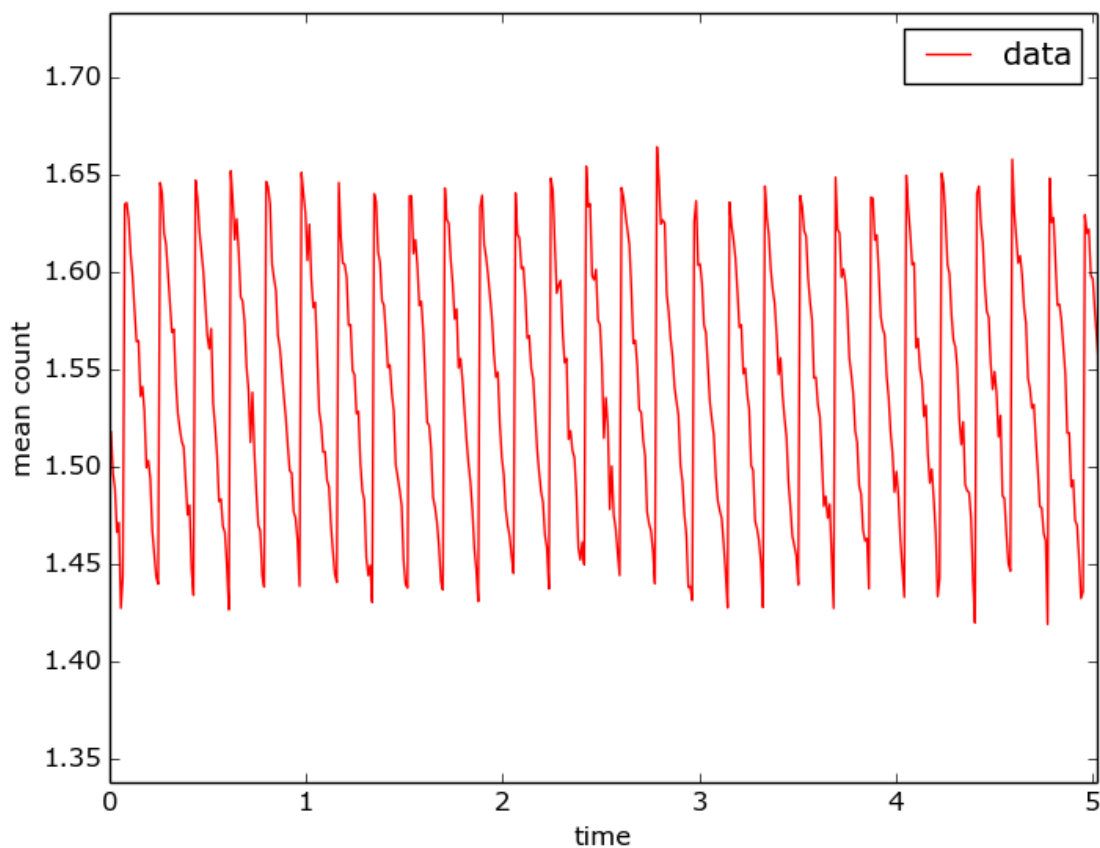


Figure 5.17.: Time series of partially dark frames (frame averaged value) for 1/2 phase shifting mode (time given in seconds), with the camera operating at 200 fps and the LED running at half the camera frequency.

However, this approach of phase-shifting also has a limitation to its application. In cameras showing a time dependence, i.e. the signal in the first frame affecting the signal in the consecutive frames, the only way to study this type of camera is to change the actual brightness of the LED.

We have discussed three different approaches to illumination control here, and each one has its own advantage. In the current setup, we never changed the driving current of the LED; we only used the pulse width modulation, or the phase shifting technique, for thermal stability of the light source and to reduce the waiting time between measurements.

Finally, given that all pixels need to be calibrated to the same light level scale, it is crucial to have a homogeneous illumination of the entire sensor; therefore, we need the integrating spheres. The same can be achieved using a set of lenses in the correct order with some diffusion screens, except the setup would be a bit larger then. The setup (figure 5.12b) contains three such light sources for individual illumination of different regions on the sensor.

The difference in the calibration and control regions exists only when we do not have the three light sources cross calibrated, meaning calibrated to the same intensity scale as seen by the camera. Once that is done, all three regions can be calibrated at once, provided the data volume can be handled, see Appendix A.

5.3.2. Trigger Box

It is a unit that sends the relevant trigger signals to the camera and the light sources. It allows individual triggering and pulse width control of all the setup elements, allowing the setup to be run in two independent modes, pulse width controlling the illumination and the phase shift controlling the illumination. The trigger box is an in-house development, purpose-built for various instrumentation projects at MPS. It is based on a field programmable gate array (FPGA) to guarantee the required timing accuracy for all eight output ports. The timing sequence is programmed via a serial computer connection and then executed in hardware on the device.

5.3.3. The Camera

Several different types of CMOS cameras are used in the various instrumentation projects at MPS. The setup was designed such that different cameras can be characterised. Commercial machine vision cameras are modified with an in-house temperature stabilisation system. The temperature control is based on a thermoelectric element (Peltier element) on the camera head and a water circuit to transport the heat of the warm side of the Peltier element. As we are running the cameras without a protective window in front of the sensor, the cameras cannot be cooled (which could cause damaging condensation on the sensor) but stabilised to typically a few degrees above ambient (22-23°C). Temperature stabilisation of better than one Kelvin is reached with that setup.

The setup currently uses a commercial macro lens for projecting the targets onto the sensor, providing one-to-one mapping of the target onto the sensor. Although the macro lens works fine as an imaging system for the cameras used in this work, we would need to develop a separate imaging system for a different camera. The final goal is to have a configurable imaging setup, allowing us to calibrate even medium format sensors and, in

future, even much bigger ones if they come into existence. Table 6.1 lists the cameras and their operating mode used for testing.

5.3.4. Mechanical and Cooling Elements

Stepper Motor Based Linear Stages To cover the entire parameter space, we need different targets. This is achieved by moving the two side light sources, marked by double-sided arrows in figure 5.12b; hence we need a movable stage for the light sources. In the present setup, we have two linear stages, which can be configured using a stepper motor controller linked to the overall control of the setup.

Water Chiller and Pumps As each light source and the camera is mounted with a water cooling block, the heat generated is dumped into a water chiller, maintaining the water at a constant temperature. The water is circulated through the loop using near-zero or negative water pressure to be safe from leaks.

Temperature Controller This is required mainly to control the Peltier elements for the camera.

This setup has been designed to calibrate monochrome sensors. We would need to modify the light sources and the accompanying optics for them to have a configurable wavelength of illumination for calibrating colour sensors. We only need monochrome sensors for most of the photo-metric or polarimetric applications, where the only effect of changing the wavelength is to change the number of charges generated. Hence the wavelength configuration part was left out in this setup; currently, the only way to change the wavelength of the light source is to replace the LED with the one for the desired wavelength.

5.4. An Alternative Setup

Given that the critical part of the setup is to create different scenes on the sensor, a suggestion would be to use a matrix of LEDs (or an OLED panel) and map it onto the sensor. The top part of figure 5.18 shows precisely this. A matrix of LEDs can indeed illuminate different regions of the sensor independently. The problems with this kind of illumination source would be the non-uniformity of the different LEDs and their non-linearity. The other problem is the illumination control; phase shift control of camera illumination is impossible here unless the LED matrix is explicitly made for this calibration setup. The commercially available display modules do not allow for independent clocking of each pixel.

Some characteristics we would like in this panel would be that each LED has a small angle of radiance, for each LED to be considered an individual light source and not contaminate the light from other LEDs. Furthermore, an optical system that can project the illumination plane onto the sensor is a must for this setup. Once we have a calibrated display panel (or LED matrix), it would be the best light source available. Moreover, this is the part where future developments for the calibration setup are needed.

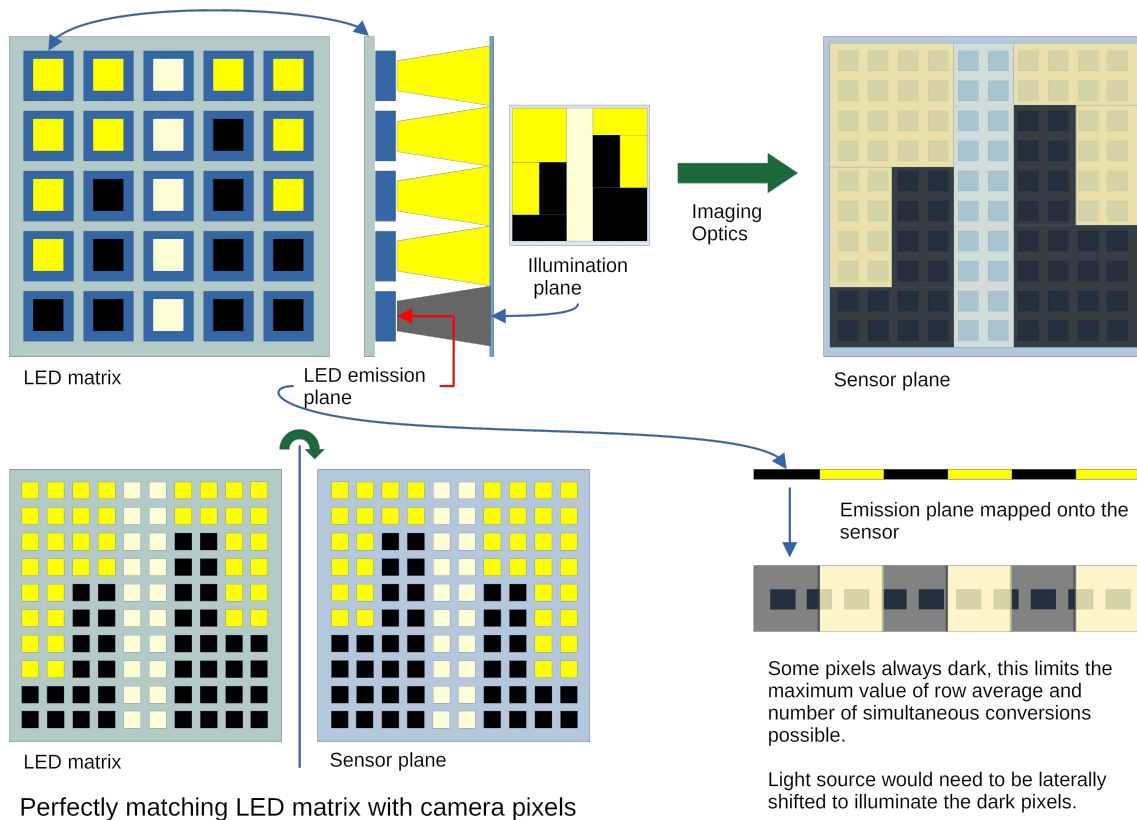


Figure 5.18.: Schematics of calibration setup containing a LED matrix as an illumination source. The top row is the desired case. Light yellow regions are calibration regions, with bright yellow and black being the illuminated and non-illuminated control regions mapped onto the sensor. The bottom left is the ideal case of each calibrated LED mapped onto a single pixel, but practically impossible. The bottom right part shows why we cannot directly map a light source (with a different spatial density from the sensor) onto the sensor.

Once we have a calibrated panel, the rest of the steps are similar to what we have done in our current setup. One regime where this kind of setup would be superior to the one we currently have is with sensors having a more complicated resource sharing between the pixels, complicated in the sense of sharing resources in both dimensions. However, if that is not the case, it is much easier to operate the current setup.

6 Camera Characterisation Process and Results

At MPS, we use a variety of cameras for ground-based solar observations. During this thesis, I worked on characterizing three of these. For our use case, we typically use the same settings or only a small set of variable settings across different observation campaigns. This is done to avoid calibrating the camera for each and every small change in the camera settings before every observation, as it is impossible to do that. Hence, the only viable option is to run the camera in a constant state. Thus the optimal operating temperature, gain settings, and exposure time are chosen after the initial calibration when the camera arrives in the lab for the first time.

The first thing to do when the camera arrives in the lab is to start by making it compatible with our camera control system (Appendix B). Exposure time is set to maximize the duty cycle at a given frame rate, while the frame rate is set as high as possible. The cameras and the configuration parameters are listed in Table 6.1; the calibration process was done for only one configuration setting listed in the table.

Cameras used in the Project			
Properties	Cam1	Cam2	Cam3
Pixels WxH	2048 x 1934	2048 x 2048	1280 x 1024
ADC Resolution(bit)	10	12	14
Full well charge range used(ke^-)	13.5	2.7	50
Frame rate(fps)	200	48	90
Shutter	Global	Rolling	Global
Model	SP-12000M-CXP4	GSENSE400BSI	PIRT 1280SciCam
Manufacturer	JAI	Gpixel	Princeton Infrared
Instruments		SUSI (Feller et al. 2020)	GRIS+

Table 6.1.: Cameras used and their operating configuration.

It should be mentioned that Table 6.1 only lists the essential parameters of concern for this work. Modern machine vision CMOS cameras come with extended capabilities for data processing in real-time right on the camera unit before the image is written to storage. Starting with basic cosmetic corrections for dark/bias subtraction and corrections on a

higher level, typically based on pre-stored calibration data for different operating conditions (temperature, exposure time etc.). Such features might be interesting for real-time machine vision applications (component inspection on an assembly line, surveillance, etc.). However, it is critical to switch them off entirely for precision photometric applications as we are using them in astronomy and spectropolarimetry in particular. This is because the precise algorithms for the corrections are usually not documented well (intellectual property of the camera vendors) and because the algorithms are often adaptive, e.g. they operate based on light level and temperature data from previous frames, making it virtually impossible to reproduce a certain outcome.

Here we shall be presenting the characterisation process and the results as they were done for each camera. We will see that even though the overall idea remains the same, the exact strategy used for each camera is a bit different. The complete characterisation was done only for CAM1, showing the due process taken for the calibration.

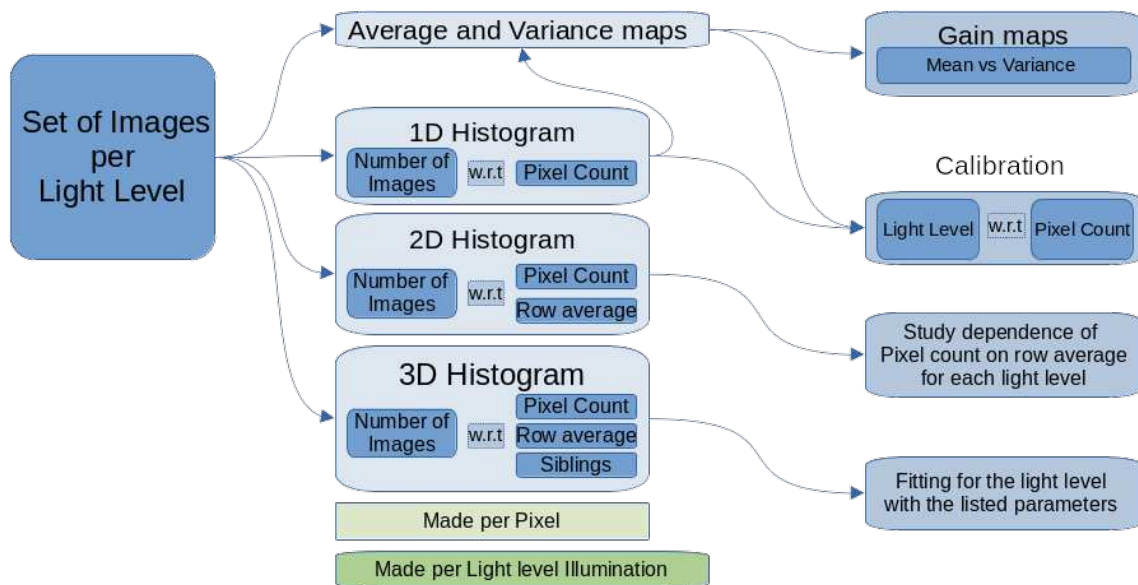


Figure 6.1.: Flow diagram for the data processing. As histogramming is done by stacking images, the axis denoting the number of samples in the histogram refers to the number of images used. The histogramming is done per pixel; hence, we have an array of histograms (each being 1D, 2D or 3D, as required).

Figure 6.1 displays a flow diagram for the data acquisition and processing. There are two main branches, one linked to saving the actual images to the disk, as they are captured from the camera. The other branch is linked to making histograms for all pixels. Here we want to make per-pixel histograms by staking the images for one light illumination scene; thus, the distribution contained in the histogram for one pixel is from the set of images used to make the histogram. This is a one-dimensional histogram, as only the light level was considered to make the histogram for a pixel.

Similarly, we can make 2-dimensional and 3-dimensional histograms for each pixel by adding the row average and siblings to the considered parameters. That means that

each bin for a 3D-histogram is defined on the light level, row average and the siblings' axis. For each pixel, the samples are collected from all the images for one scene. This histogramming is just a convenient data storage technique.

Before we move ahead, let us properly define the terms homogeneous illumination, uniform illumination, full illumination, and flat illumination. We shall always deal with a homogeneously illuminated sensor, where the illumination beam is from the output of an integrating sphere. However, there can be different targets in the beam paths. Full illumination would mean no target in the beam path; it will be interchangeably used with flat and uniform illumination. At the same time, the term constant illumination would refer to the fact that the light level is not changing during a test. The term scene dependence ideally would encompass all kinds of variations of different illuminations of the sensor. Furthermore, our designed setup allows us to project different scenes on the sensor. However, in this text, this term refers to the row average and the siblings' dependence whenever we cannot separate the two.

6.1. CAM1

The SP-12000M-CXP4¹ camera (first in table 6.1) is based on a CMOSIS CMV 12000 CMOS sensor with a native resolution of 4096×3072 pixels. When the region of interest is restricted to 2048×1934 pixels, a frame rate of 400 Hz is possible with 10-bit digitisation and with global shutter operation. The high frame rate at 4 Mpixel makes the camera extremely interesting for our applications because it allows us to capture a complete polarimetric state (4 modulation states) at an effective rate of 100 Hz, which is similar to the evolution time scale of atmospheric seeing, and cameras of this type have already been used in the field for various instrumental setups (e.g. Zeuner et al. 2020, Saranathan et al. 2021). For the characterisation and calibration runs carried out for this thesis, it was decided to operate at 200 Hz because that was the maximum frame rate that could be achieved with stable operation, as the aforementioned histogramming (see Appendix A) is done in real-time before the data is written to disk. Initial tests with the camera showed a pronounced non-linearity and indicated a scene-dependent response. The characteristics of the camera response are investigated in detail in the following.

6.1.1. Preliminary Characterisation CAM1

6.1.1.1. Slanted Edge Target

The first target projected onto the sensor is a dark triangular edge, as described in section 5.2.2. We want to use this target to see the effect of changing the row average, and we would like to do that for different light levels.

For the triangular target test, we start by taking 10000 images per light level for the triangular target and the fully illuminated sensor. We had a total of 11 light levels for the preliminary test, including the dark. We can take ratios of averaged target images and the

¹<https://www.jai.com/products/sp-12000m-cxp4>

fully illuminated images per light level. One such image ratio for one light level is shown in figure 6.2c, the ratio of slant target and the fully illuminated sensor shown in panel (a) and (b) of figure 6.2. We can clearly see a gradient in the always illuminated triangular region, with the primary direction of the gradient being vertical, which is also the direction of changing row average. One of the direct inferences of this vertical gradient is the presence of the scene dependent effect varying with each row. This indicates to a row-by-row readout which is consistent with the readout direction specified by the manufacturer.

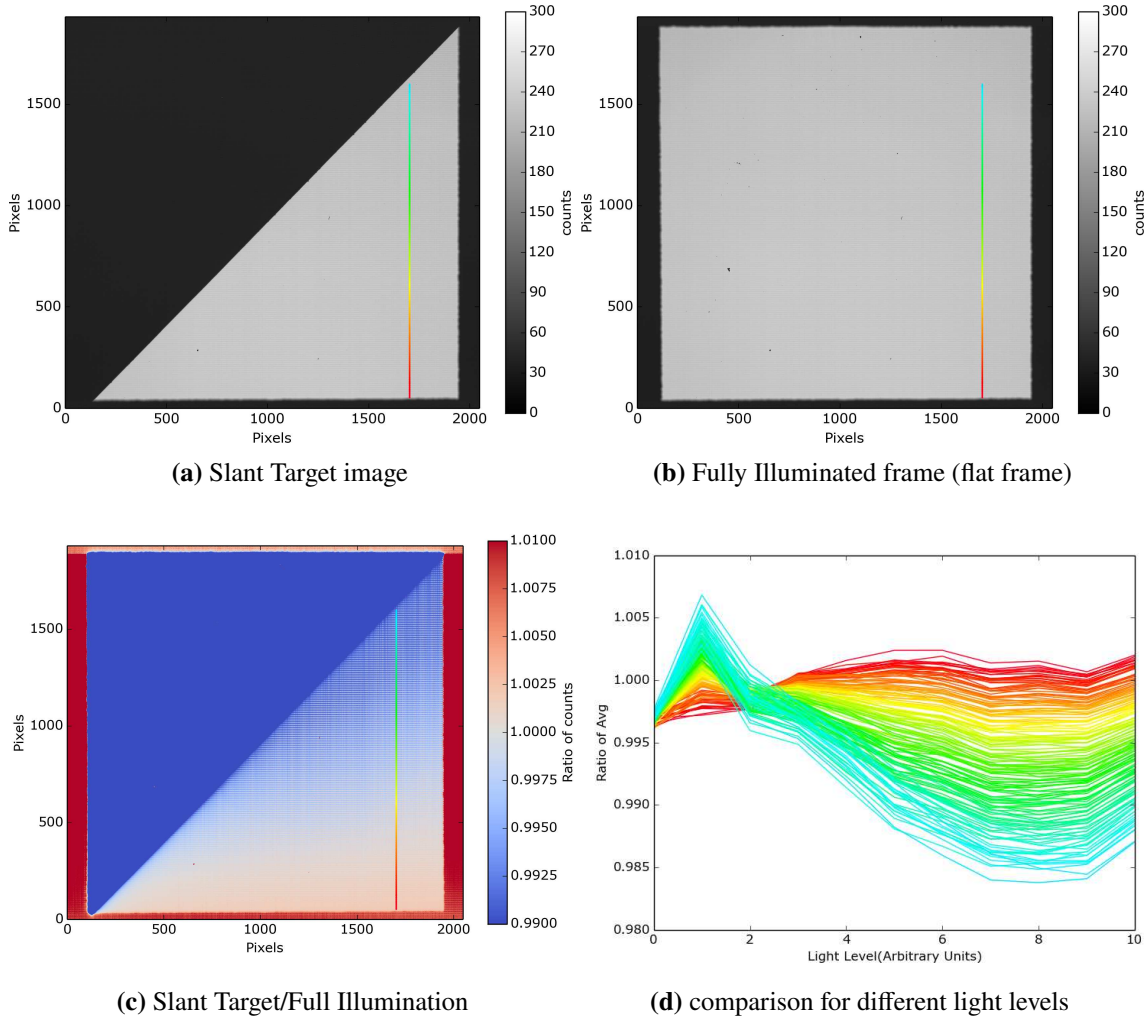


Figure 6.2.: Slanted target projected on Cam1. The bottom right triangle is always illuminated, and the upper left is shielded. Panel (c) shows the ratio of the target image with the flat(uniform and fully illuminamted) illumination. Panel (d) plots that ratio (target/flat) as a function of light level for the pixels of one column on the sensor, marked by the rainbow line in images, where the colour in the line corresponds to the different rows.

The ratio as a function of light level is plotted in figure 6.2d where the different colours correspond to the vertical positions along one column of the sensor as indicated with the coloured bar in figure 6.2c. The peak to valley deviation shows that this scene dependent response has a magnitude of up to 2% of the light level.

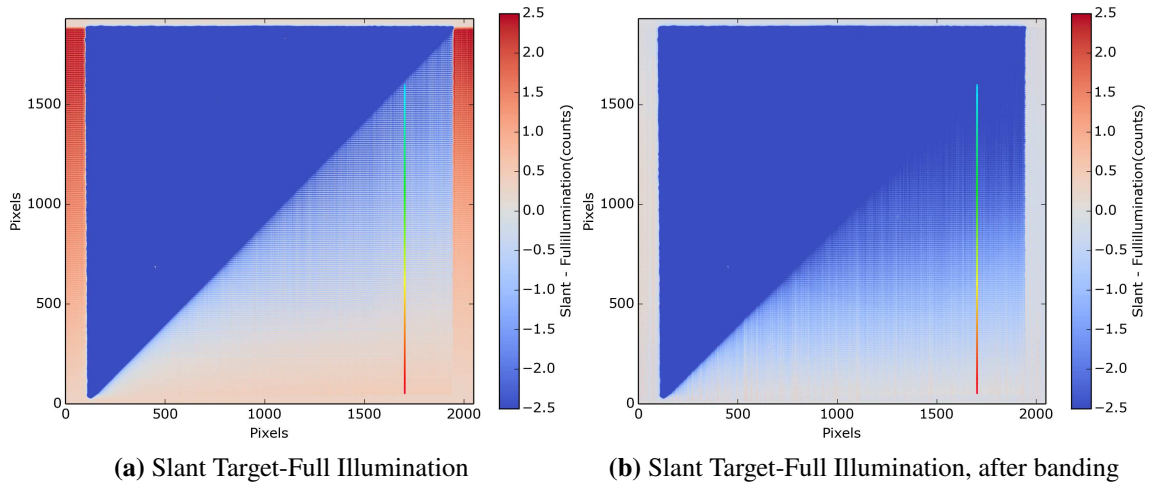


Figure 6.3.: Slanted target projected on Cam1, Difference with the fully illuminated frame, (a) before banding correction, (b) after banding correction, as described in section 6.4.3.

We can try to correct this scene dependent effect by deriving a correction factor using the deviation of the count in the shielded pixels on the edges, given by:

$$\text{Average} (test\ image - dark\ image)_{\text{Shielded pixels}}$$

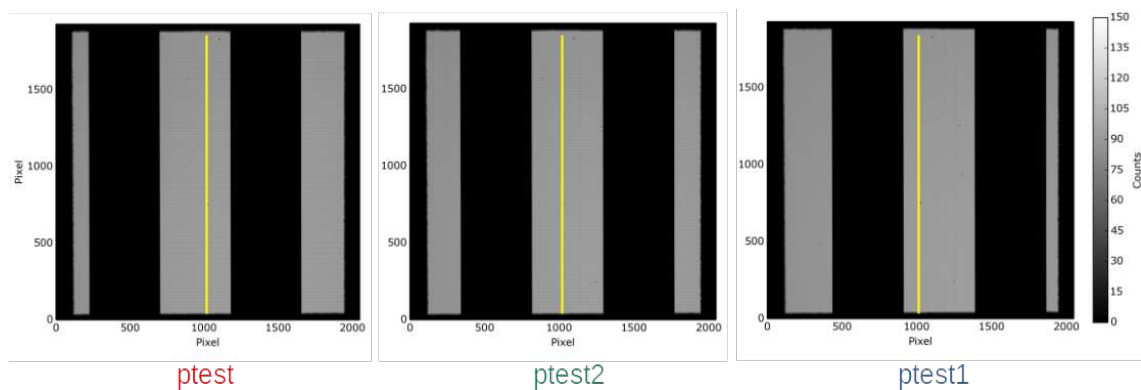
This value is subtracted from the test image to get a corrected image (for each row) and is called banding correction. This correction is applied to both the slanted target and fully illuminated images. The difference of target image and flat illumination is shown in figure 6.3, for the two cases of before banding correction (figure 6.3a) and after banding correction (figure 6.3b). Banding correction, or correcting for the deviation as seen in the shielded pixels, mainly accounts for the dependence of the pixel count on the row average. Looking at the two images in figure 6.3, we can see that the banding correction easily corrects for the deviation in the shielded pixels and the lowermost region of the image. The lowermost region of the image is the region where the always illuminated triangle has the same number of simultaneous conversions in the row for the target image and the fully illuminated image. As we move towards the top of these images, the number of siblings starts to differ in the target and fully illuminated images. Thus, we see the gradient in the always illuminated region even after the banding correction.

The vertical stripes (in figure 6.3b) indicates that each column has its own set of readout electronics, further confirming that the sensor has a column parallel readout.

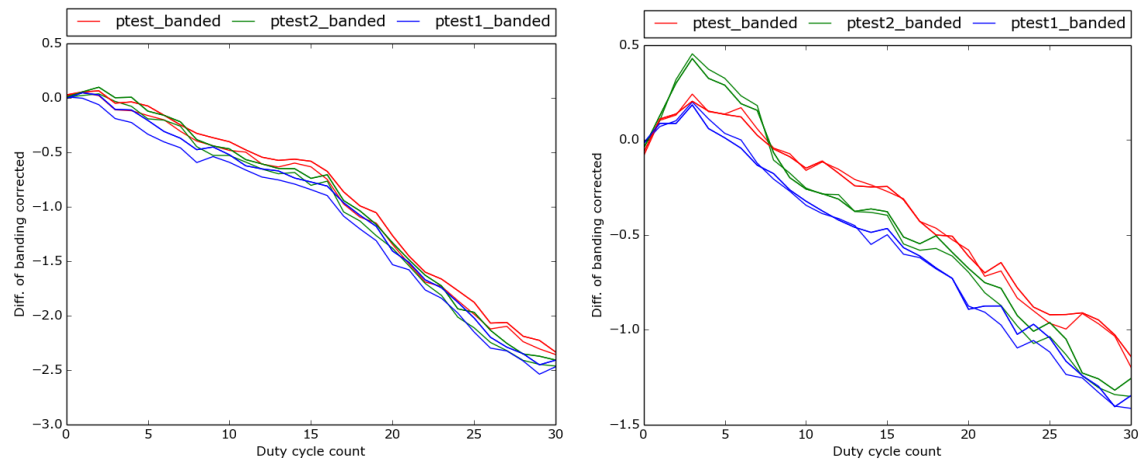
6.1.1.2. Parallel Bar Target

A set of parallel vertical bars (for column parallel sensors), are projected onto the sensor (figure 6.4). This keeps the average signal in each row constant while moving the target across the sensor can change the illumination pattern. 10000 images were captured per duty cycle. Where a duty cycle of zero corresponds to the dark and the last duty cycle corresponds to an average of 300 counts; thus the duty cycle is a proxy of the illumination.

As the target is moved across the sensor, we look at the response, using the average count of the pixels in a column, indicated by the vertical yellow bar in figure 6.4. To clarify a bit more, we can make a histogram using the pixels along a row, where the x-axis of the histogram is the illumination, and the y-axis is the number of pixels; this is a row histogram. A parallel bar target keeps this histogram similar for all sets of odd and even rows. Moreover, shifting this target horizontally does not significantly alter the row histogram. The effect of shifting this parallel bar target is of the order of 0.25 counts on average, the average separation between the different coloured profiles. While the profiles go down to about -2.5 counts for the even rows and -1.5 counts for the odd rows. Thus the effect of the row histogram is an order of magnitude stronger than the effect of the positioning of the target. Furthermore, as effect of shifting the target is an order less than the effect of the changing row average, we will ignore it for this camera.



(a) Reference images for the Parallel Bar test



(b) averaged over even rows

(c) averaged over odd rows

Figure 6.4.: Parallel Bar test for CAM1. Deviation from the flat, in the always illuminated region marked by the yellow vertical line. The different colours correspond to the different positions of the target as marked in the legend of the plot, **RED Green Blue**, produced when moving the target from left to right. Made for two nearby columns, and hence we have two profiles per target.

6.1.2. Results Calibration Targets

Now that we know about the scene dependence effect and its dependence on the row average and the siblings, the whole problem can be formulated into a fitting problem. Where the digital number, or count, of a given pixel is a function of three parameters: the light level (the true number of photons falling on that pixel), the average count of the row the pixel is in, and the number of simultaneous conversions in that row. Furthermore, given that we finally want the light level falling on the pixel, we can also invert the problem and write the light level as a function of the pixel count and the other two parameters.

The idea is to do a three-parameter polynomial fit, where the parameters are the light level, the average value in a row, and the number of simultaneous conversions (defined as the number of pixels having the same value in that row). The equation for a second-order fit in all three parameters can be written as

$$\begin{aligned}
 I(x, y, z) = & c_{0,0,0}x^0y^0z^0 + c_{0,0,1}x^0y^0z^1 + c_{0,0,2}x^0y^0z^2 + c_{0,1,0}x^0y^1z^0 + c_{0,1,1}x^0y^1z^1 + c_{0,1,2}x^0y^1z^2 \\
 & + c_{0,2,0}x^0y^2z^0 + c_{0,2,1}x^0y^2z^1 + c_{0,2,2}x^0y^2z^2 + c_{1,0,0}x^1y^0z^0 + c_{1,0,1}x^1y^0z^1 + c_{1,0,2}x^1y^0z^2 \\
 & + c_{1,1,0}x^1y^1z^0 + c_{1,1,1}x^1y^1z^1 + c_{1,1,2}x^1y^1z^2 + c_{1,2,0}x^1y^2z^0 + c_{1,2,1}x^1y^2z^1 + c_{1,2,2}x^1y^2z^2 \\
 & + c_{2,0,0}x^2y^0z^0 + c_{2,0,1}x^2y^0z^1 + c_{2,0,2}x^2y^0z^2 + c_{2,1,0}x^2y^1z^0 + c_{2,1,1}x^2y^1z^1 + c_{2,1,2}x^2y^1z^2 \\
 & + c_{2,2,0}x^2y^2z^0 + c_{2,2,1}x^2y^2z^1 + c_{2,2,2}x^2y^2z^2.
 \end{aligned} \tag{6.1}$$

We need to know all the coefficients. The fitting technique we use is as given below. Suppose we were doing a one parameter polynomial fit, we will have a set of equations, given by

$$I_i(x_i) = c_0x_i^0 + c_1x_i^1 + c_2x_i^2 + \dots + c_nx_i^n, \tag{6.2}$$

where n is the degree of our polynomial. We can write the same as a matrix equation

$$\begin{bmatrix} x_1^0 & x_1^1 & x_1^2 & \dots & x_1^n \\ x_2^0 & x_2^1 & x_2^2 & \dots & x_2^n \\ x_3^0 & x_3^1 & x_3^2 & \dots & x_3^n \\ \vdots & \vdots & \vdots & \ddots & \vdots \\ x_N^0 & x_N^1 & x_N^2 & \dots & x_N^n \end{bmatrix} \times \begin{bmatrix} c_0 \\ c_1 \\ c_2 \\ \vdots \\ c_n \end{bmatrix} = \begin{bmatrix} I_1 \\ I_2 \\ I_3 \\ \vdots \\ I_N \end{bmatrix} \tag{6.3}$$

$$A \times C = I. \tag{6.4}$$

Multiplying it with the transpose of the matrix,

$$A^T \times A \times C = A^T \times I \tag{6.5}$$

$$B \times C = D \tag{6.6}$$

This equation can be solved to reveal $C = B^{-1}D$. The codes to numerically solve this type of equations can be found in the standard library of most programming languages.

Proxies of light level

We have a direct measure for the row average, the number of siblings, and the count of the pixel, but we would need some proxy for the light level, such as: 1) The phase shift between the LED and the camera. 2) The pulse width of the LED. 3) The average value of the fully illuminated row. The first two items have a direct correspondence to the integration time of the sensor, and are the most natural proxies for the light level for the two methods of illumination controls, respectively. At a final stage we would want to have a scale for the photon flux linked to these proxies. But for the work discussed here it would suffice to make calibration profiles linked to these proxies.

6.1.2.1. Calibration Using Deductive Targets

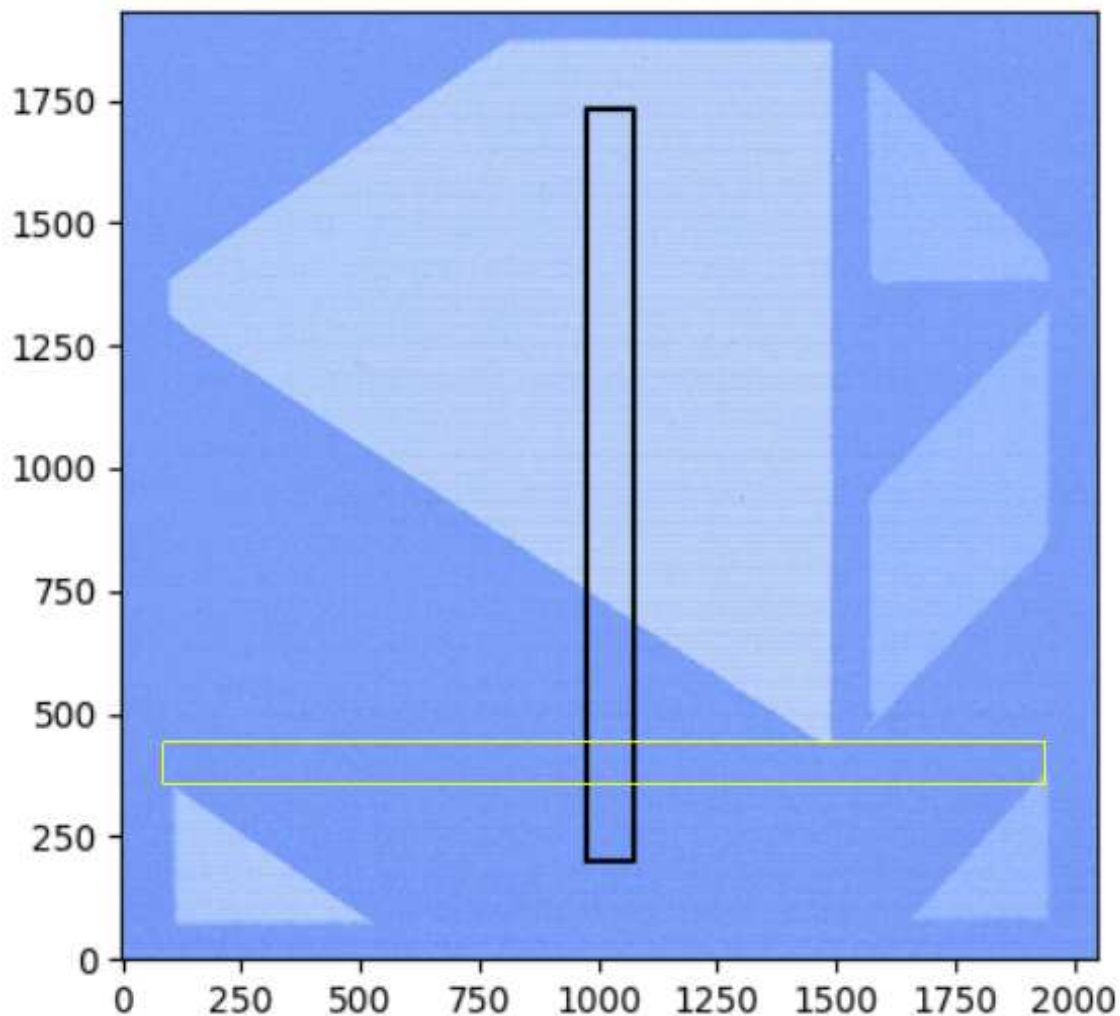


Figure 6.5.: For the test target image, an image showing the calibration region(the black rectangle). The yellow region marks the dark pixels, where the row averages are similar to the pixel value in the region.

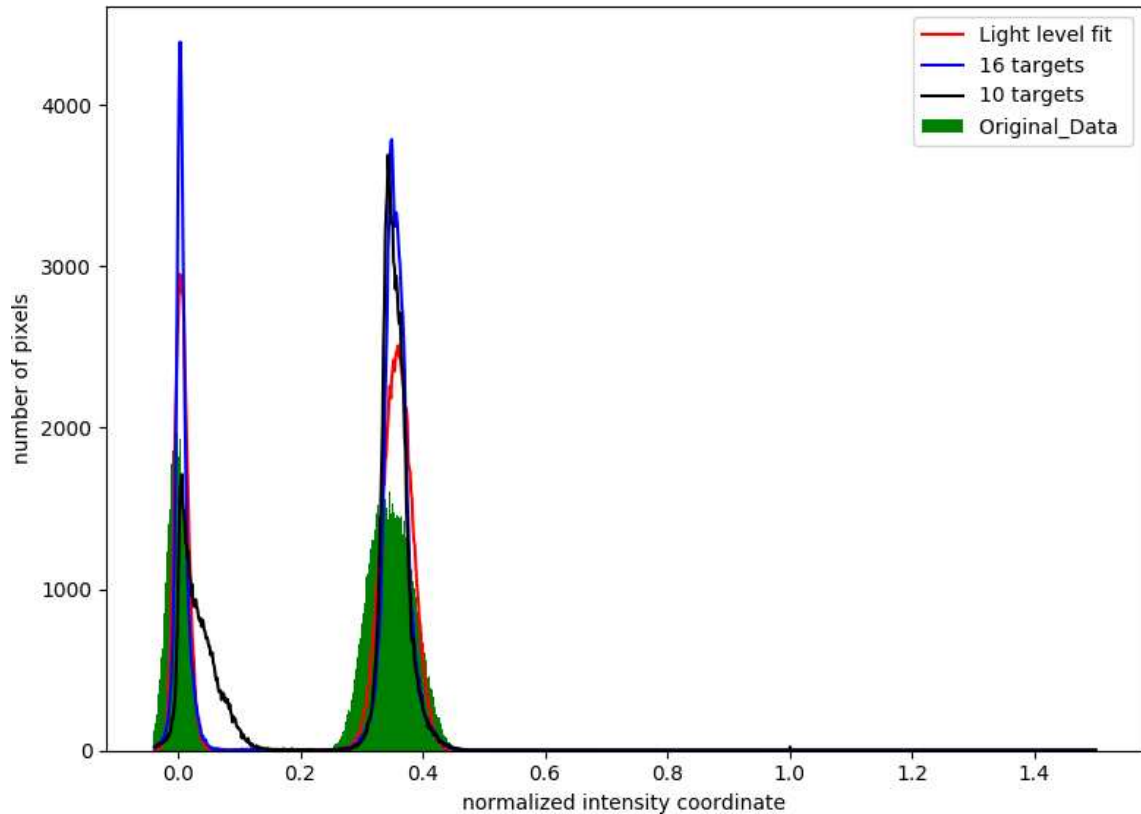


Figure 6.6.: Histogram of the pixels in the calibration region marked by the black rectangle in figure 6.5. The green region is for the original data set (a linear fit with the light level), and the red profile is for just a light level fit (non-linear) per pixel. The black profile is after considering the row average and the siblings for the targets shown in figure 5.11 (see page 40). The blue profile uses the same fitting function as the black one, just that some additional targets are added to the calibration data, which have a row average more than the pixel of interest (dark pixels).

We start by assuming that all rows behave similarly for the effect of the row average and the number of siblings. We would still want to vary the row average and the number of siblings independently. The target used is shown in figure 5.11 on page 40. After collecting the calibration data and fitting, the resultant fitting function was tried on a different target, as shown in figure 6.5. For comparison, only the region marked by the black rectangle was considered. As shown in figure 6.6, we make a histogram of this region. We can see that the histogram should have two distinct peaks, one for the dark pixels and the other for the bright pixels in the black rectangle. This histogram is made using:

- The original data, in simple terms a linear fit with the light level (shown in green).
- Just the light level fit per pixel (shown in red), using a third order polynomial function.
- Recovered data after the fitting is done with calibration data acquired from targets as shown in figure 5.11 (shown in black), using a polynomial function of degree 3 in the light level, third order in the row average, and the first order for the siblings.

- The blue profile, made using recovered data after the fitting was done with calibration data acquired from targets as shown in figure 5.11 and a few more targets as shown in figure 6.5. Figure 6.5 shows targets which have a row average higher than the count of the pixel of interest (for the dark pixels in the calibration region).

One of the key points to note is that we use a homogeneous illumination, meaning that all pixels in the region of interest are expected to have a similar response. In that case, the spatial variance will tell us how well all the pixels behave compared to other pixels. This means that after the calibration, the recovered light level would indicate to one value of the light level for all pixels, and the temporal variance (one pixel, in different frames) and spatial variance (all pixels in a single frame) should ideally be the same. Thus a spatial histogram is a quick way to check how well a correction would work. We see that the histograms made using the recovered data after the fitting have narrower peaks than the original data. We also see that the histogram for the fitting done using a 3-dimensional polynomial has still narrower peaks, as seen for the histograms shown by the black and blue profiles. This narrowing of peaks indicates that additional variance was added to these histograms (due to cross-talk), which gets removed after the calibration.

The main discrepancy arises when we look at the peak for the dark pixels, for the case of fitting done using just the targets in figure 5.11, black profile in figure 6.6. The peak for illuminated pixels has the expected normal distribution shape, but the peak for the dark pixels is not symmetric and has a bulge on one side. The explanation for this bulge is that the fitting did not give proper values for these pixels. We identified that the pixels in the lopsided region histogram are for the case where the row average is much higher than the actual value of the pixel (dark pixels excluding the pixels in the yellow block). Sadly that regime of the parameter space can only be covered using the independent illumination setup or additive targets. For the dark pixels, the case of a row average higher than the pixel value is easy to achieve, as can be seen for the dark pixels not in the yellow region in figure 6.5. We make a fit after considering calibration data from these targets as well; the blue profile in figure 6.6 shows this case. We see that the problem for dark pixels is fixed in this case. This illustrates the importance of covering the entire parameter space for the calibration data. The critical difference that these extra targets make is to add more data for the dark pixels when the row average is higher than the count of the pixel. This data set is missing in the original targets, shown in figure 5.11 on page 40.

6.1.2.2. Calibration using the Independent Illumination Setup

The next stage is to acquire the calibration data using the independent illumination setup shown in figure 5.12b (see page 42). Figure 6.7 shows the different regions of illumination formed by the projected target using the calibration setup (three-sphere setup). We can cover the entire parameter space formed by the different parameters by controlling the width and light level in the control regions. The data for this experiment was collected after spanning all the targets, as shown in figure 5.5 on page 35. We project these targets for each light level as in figure 6.8, and finally cover the entire space shown in figure 6.9. Each point in figure 6.9 is a distribution of points around an average value. To generate the plot, we take averages of all the three parameters for each target and light level.

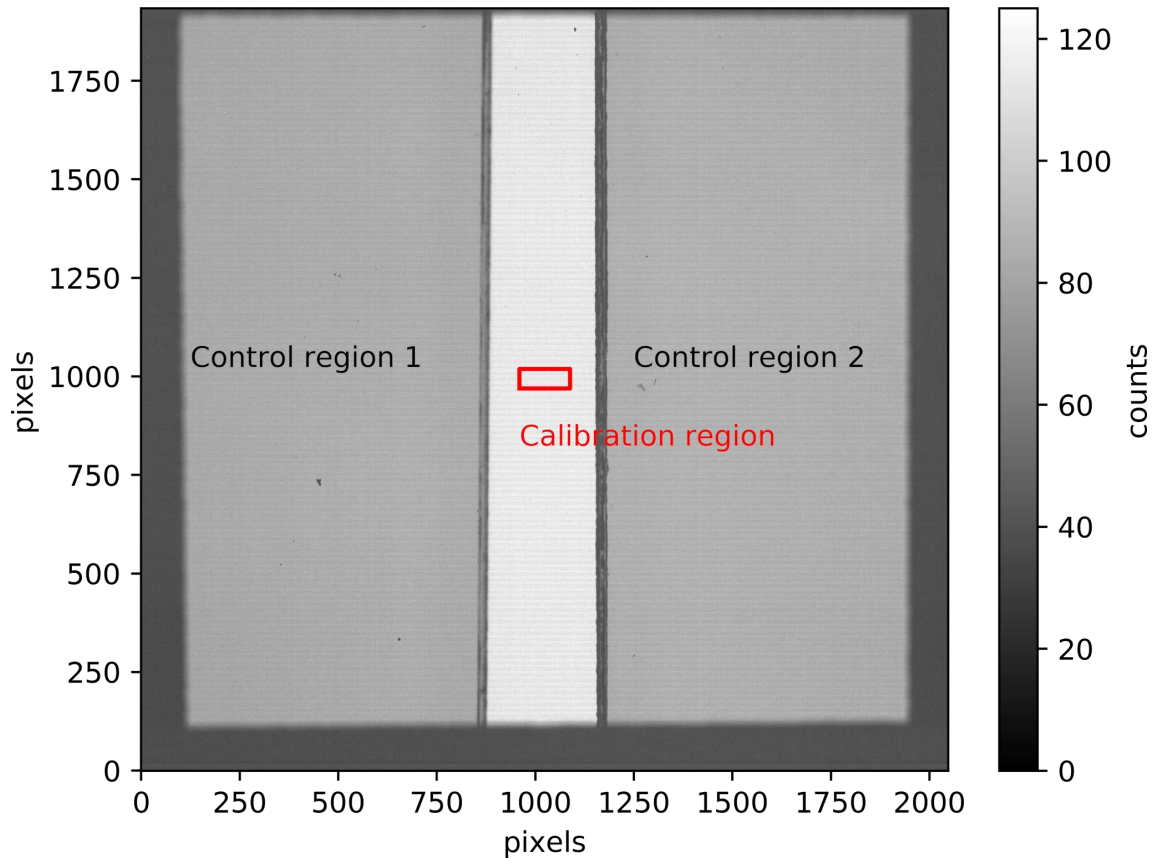


Figure 6.7.: Calibration region selected for testing, and the configurable control regions as imaged on the sensor.

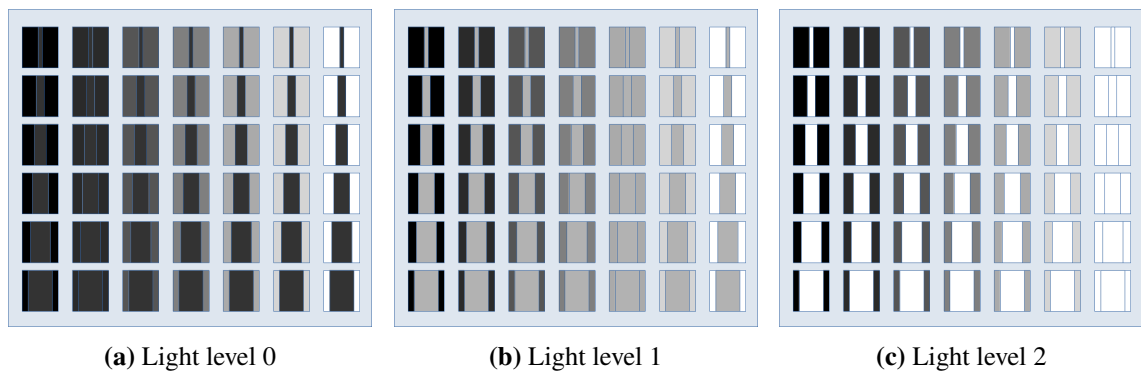


Figure 6.8.: Complete target space with three different illuminations of the calibration region, with the illumination increasing from left to right.

Figure 6.10 shows the parameter space covered for the different sets of parameters using the three light source setup. Figure 6.10a, is a direct correspondence of figure 5.1 (see page 31), where green is the always accessible region using deductive targets, and blue being the region requiring an additive target setup. The covered parameter space, as shown in figure 6.10a is not a rectangle. The reason for that is simple to see if we look at the corresponding figure 5.1, where the minimum slope allowed is defined by the minimum width of the strip corresponding to the calibration region.

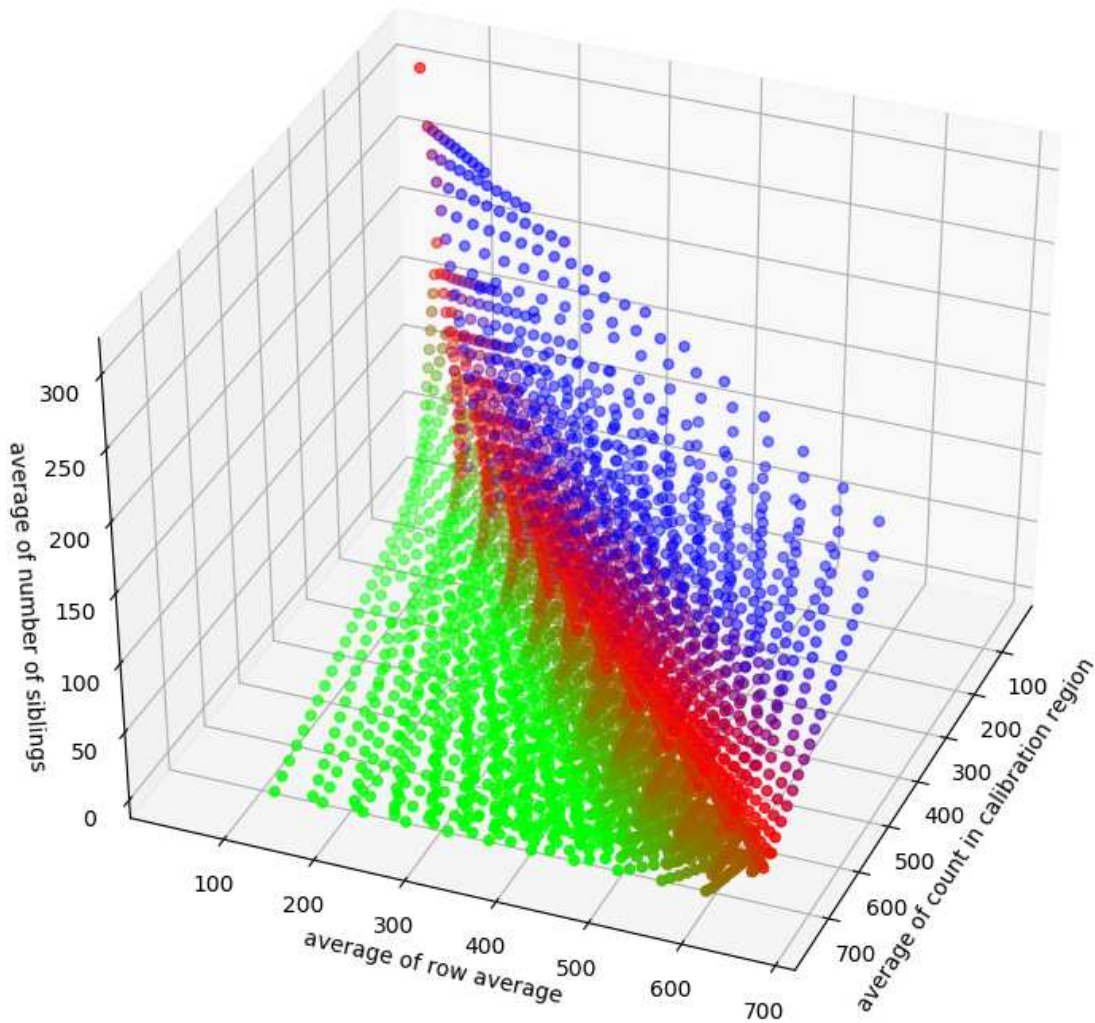


Figure 6.9.: Three-dimensional data space is formed by the average count in the calibration region, row average and the siblings. The green points are for the region covered using deductive targets, and the blue for the region covered using additive targets. The red points are the transition region from deductive to additive targets.

To understand the slant in the upper boundary of this space, we need to look at figure 6.7. Now assuming that we have a very thin central strip and maximum illumination in the control regions. Then the two extreme cases possible are the calibration region having the same illumination as the control regions. That is the case depicted by the points on the top right corner in figure 6.10a. The second is the case where the calibration region is dark, which is depicted by the dot on the top left corner in figure 6.10a. Theoretically, the roof and the base for the parameter space shown in figure 6.10a are parallel, and thus, the thinner the central strip is, the smaller is the slope, and the more complete the parameter space covered, see figure 5.1 on page 31.

Figure 6.10b shows a cut of the covered three-dimensional parameter space along the siblings and light level axis. The shape of the upper boundary is easy to understand as it is

just a manifestation of the increasing variance of the pixel count with the increasing light level. As the shot noise increases, the number of simultaneous conversions must decrease.

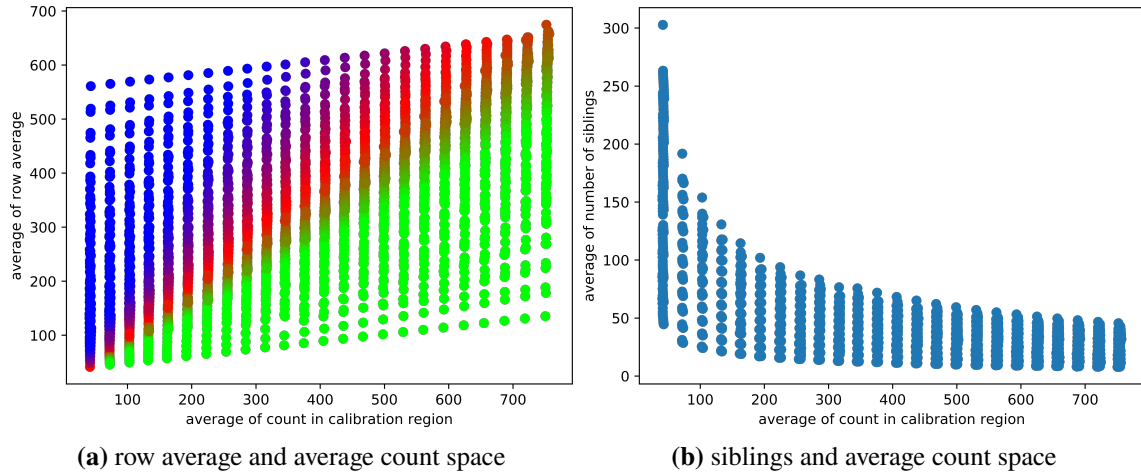


Figure 6.10.: Two-dimensional projections of the covered parameter space, (a) along the row average and light level axis, (b) along the siblings and light level axis, where the average count in the calibration region is shown as a proxy of the light level.

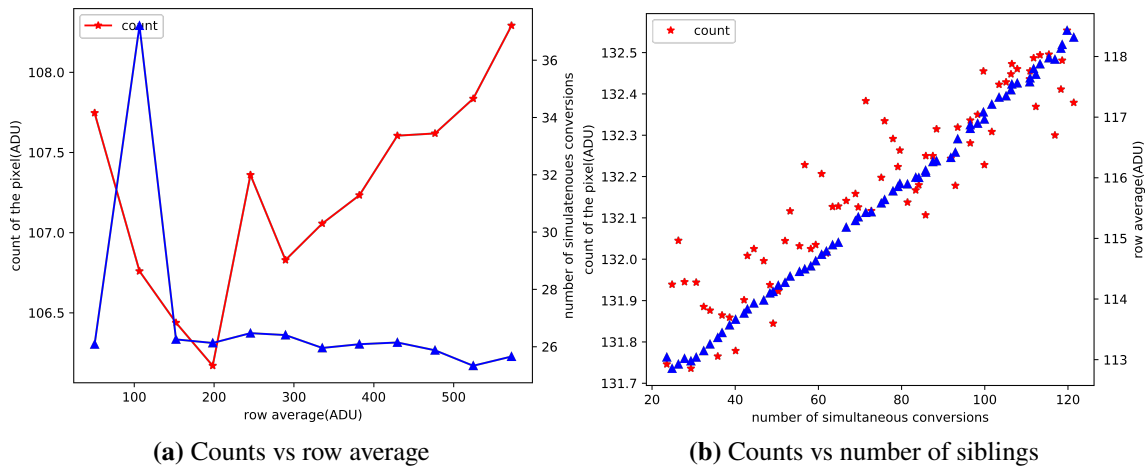


Figure 6.11.: Variation of counts in a pixel (a) with respect to the row average while the siblings are supposed to be constant, (b) with respect to the siblings when the row average is supposed to be constant. The variation of the counts is shown in red, while the variation of the other parameter, which is supposed to be constant, siblings in (a) and row average in (b) is shown by the blue colour data points, which refer to the second y-axis (on the right edge of the plots).

Figure 6.11a shows the effect of the changing row average on the counts of a pixel for constant illumination of the test pixel (red curve). The blue curve shows the values of the number of siblings during the same test; they do not change much, except the second data point, which can be considered an outlier.

Figure 6.11b shows the variation of a pixel count with the number of siblings (red). The blue data points show the change in the row average for the same test. These dependencies are for one light level; this would change over the range of the light levels falling onto the sensor.

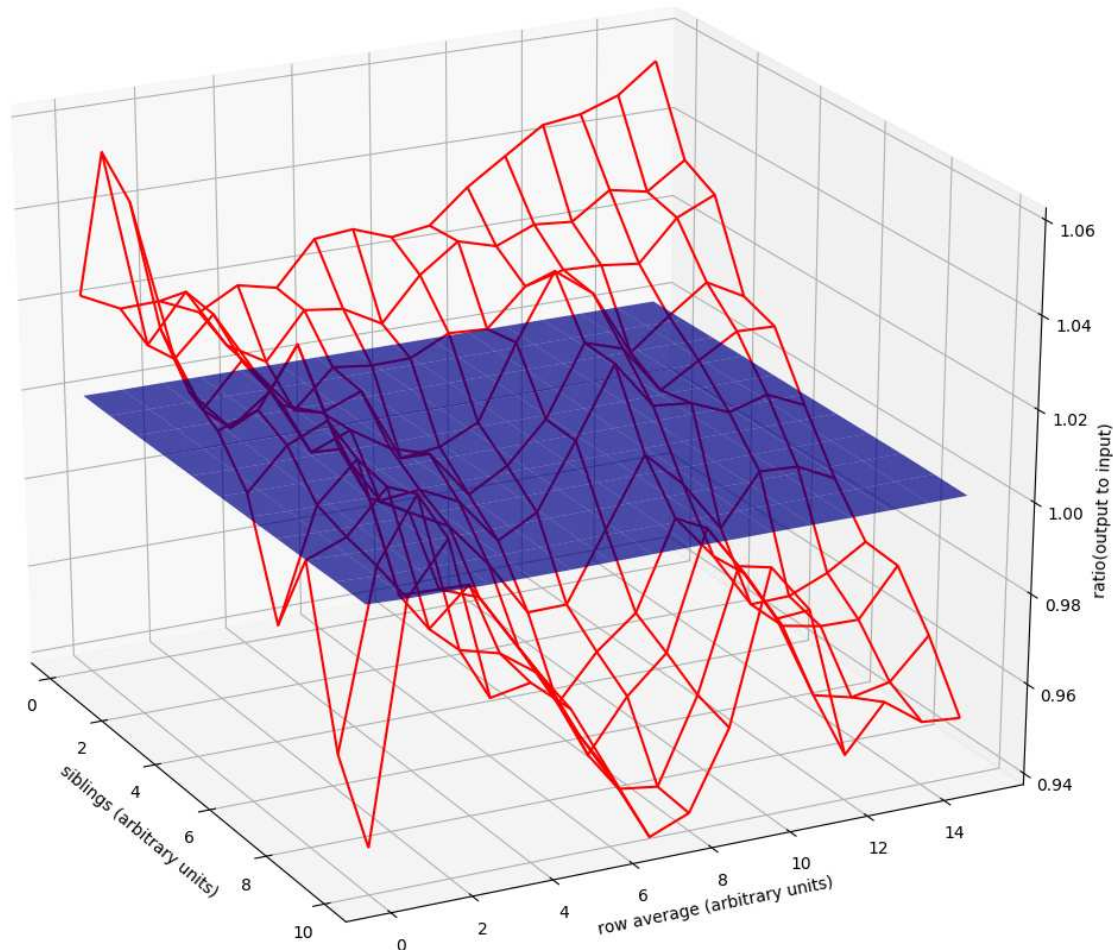


Figure 6.12.: Comparison of output to input, with the x and the y axes being the target space, and the z showing the deviations from a reference light level fit as a ratio of the input light level.

Thus, the count can be seen as spanning a two-dimensional surface lying above the x-y plane, where the x and the y axes are the row average and the siblings. This surface is not guaranteed to remain the same for the different light levels. A roundabout way to deal with this problem is first to make an average light level fit for all pixels. That means for one pixel, gather the data for all the targets and make a light level fit, forgetting that each target corresponds to different row averages and siblings. This helps in two things, one is to set a scale for the light level, and second, we can look at the final count of the pixel for different target configurations as a deviation from this developed scale.

We show such a map for the different targets in figure 6.12. The red mesh is the deviation

shown as a ratio for one light level and one pixel. The x and y axes is the different targets, and here we directly used the siblings and row average as the proxies, simply stating it is just the target space we saw in figure 5.5 (on page 35). We can see that the level of deviations from the normal scale goes up to 6% on the intensity scale. The blue surface shows the same after fitting this red surface and making the corrections. Figure 6.13 shows a scaled up view of the blue surface. Moreover finally, to get an idea of the correction, we can look at the vertical scale in the two figures. The residual deviations are now of the order of 10^{-4} or 0.05% of the intensity scale. Certainly, the structure remains in the corrected map, but now the scene dependent non-linearities would be 100 times better than an uncalibrated sensor. We were able to confirm it for a small region of the sensor. Here we looked at one pixel and all the different target configurations projected onto the sensor.

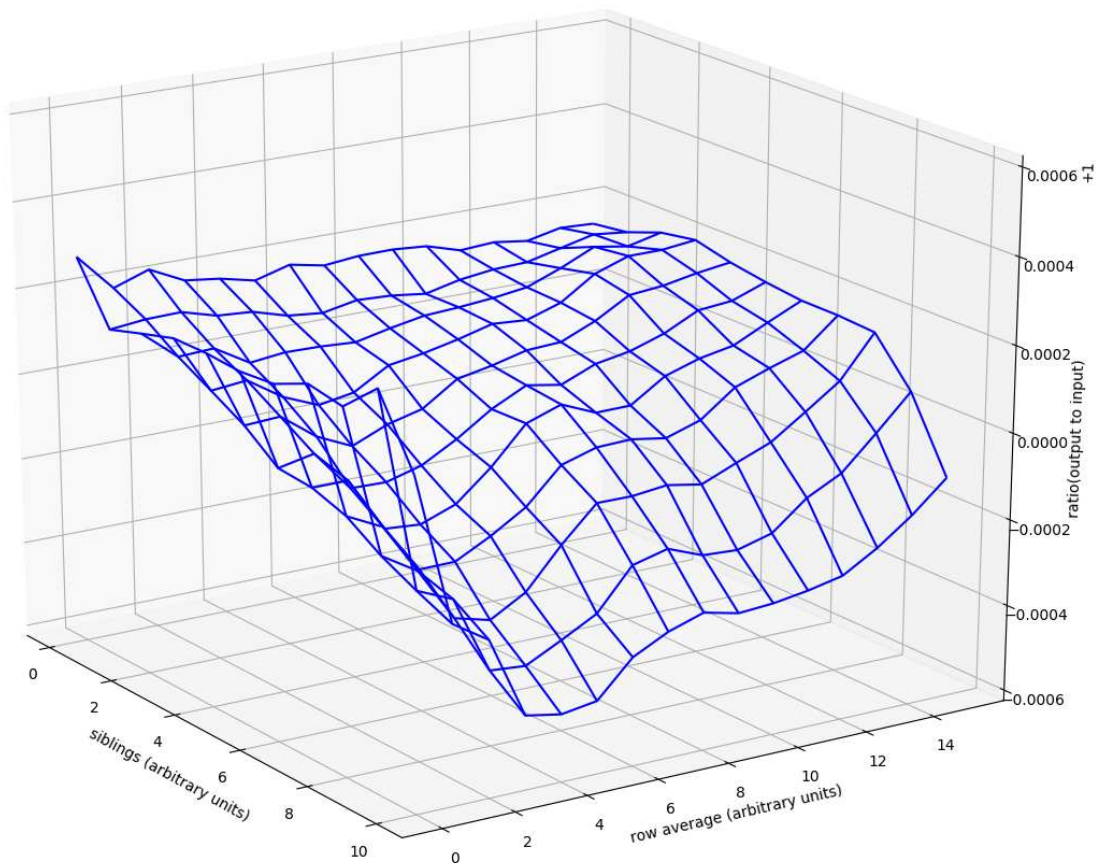
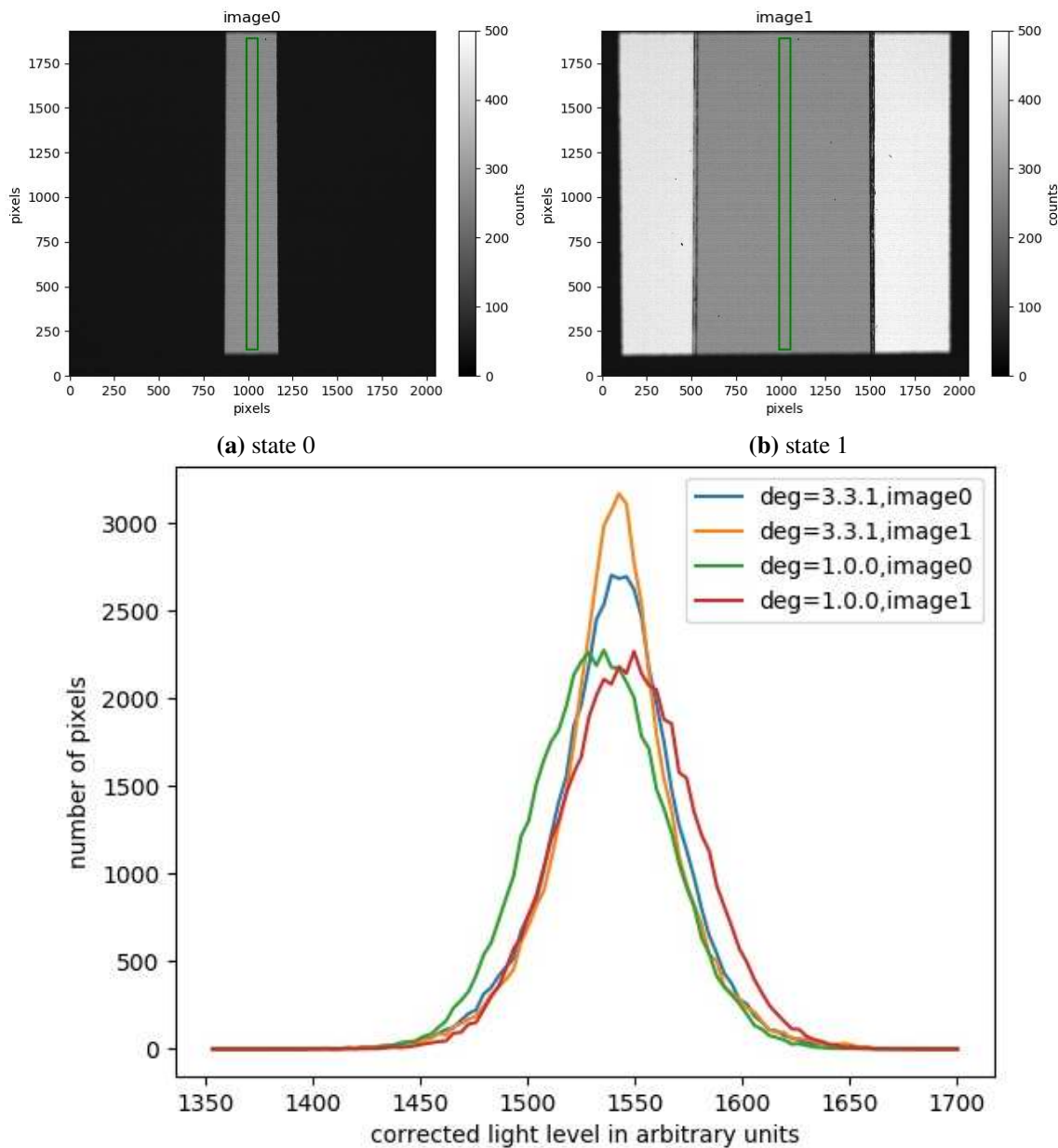


Figure 6.13.: Comparison of output to input after correction, with the x and the y axes being the target space, and the z showing the deviations from a reference light level fit, after including the row average and the siblings in the calibration.

Next, we try to look at just two different targets in the target space shown in figure 5.5 and all the pixels in the calibration region. We show the histogram comparison for this purpose using a secondary data set. Figure 6.14 shows the histogram of pixels in the calibration region marked by the green rectangle in figure 6.14a and figure 6.14b. We can see the difference in the location of the peaks for a first-order light level fit, which scales

the data to the light level proxy used for the calibration (image0 in green and image1 in red). The overlap of the other two peaks in the plot shows that the deviation in the pixel count due to a different scene on the camera is corrected by the polynomial fit, at least in a statistical sense. There are still a few differences, like the width of the blue and orange peaks is different, indicating that there is still some additional variance (due to the scene dependence) left in the corrected pixels. Ideally, we would want these two peaks to overlap in position and shape and size for a perfect correction.



(c) Comparison histogram of the pixels in the green rectangle for image0 (blue and green) and image1 (orange and red), with the degree of the polynomial given in the figure legend. Where the first value is for the light level, the second for the row average and the third for the siblings.

Figure 6.14.: Comparison between different states, with the x-axis being the proxy used for the light level.

6.2. CAM2

The sensor we shall look at now is one of the sensors used in the Sunrise Ultraviolet Spectropolarimeter and Imager (SUSI; Feller et al. (2020)). It has a rolling shutter. As SUSI is integrated under clean room conditions, this sensor had to be characterised in the cleanroom. The calibration setup described in chapter 5 could not be used. Instead, a dedicated setup for the characterisation of this camera has been installed in the clean room (similar to figure 5.12a on page 42). The first test was again to look at a triangular edge; some example images from the test are shown in figure 6.15.

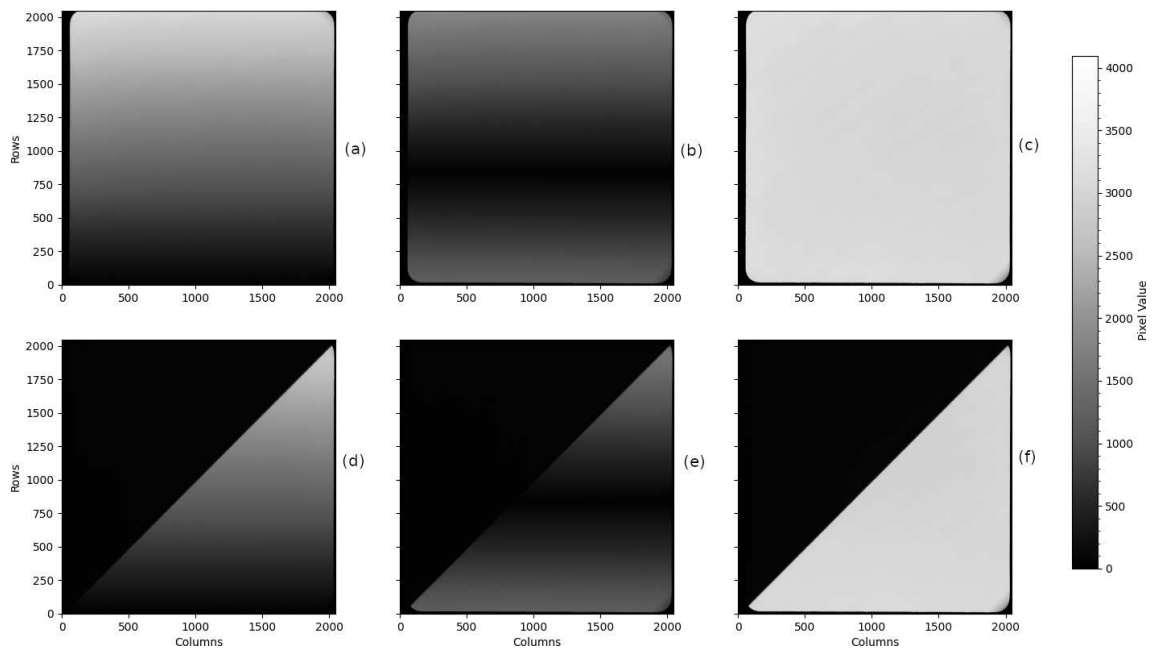


Figure 6.15.: Example images for a fully illuminated sensor and slant target. For the first column of sub-images, the rising edge of the pulsed illumination is synced to the first sensor row, and for a rolling shutter, we will get a gradient illumination in this case. The second column corresponds to a phase shift between illumination and rolling shutter, i.e. the illumination is synced to a different sensor row. We get the last set of images if we keep the light source just in the ON state; after the first frame, all the other frames will have a constant illumination for all rows in this case.

The images in the first column of the figure 6.15 are obtained by setting the LED-ON time (pulse width) equal to the rolling-shutter time and syncing the start of the illumination with the start of the exposure of the first row. The rolling-shutter time is equal to the frame-acquisition time. The LED will be OFF during the following frame acquisition, i.e. the period of the LED pulses corresponds to half the frame rate. The resultant images will have a continuous illumination gradient across the sensor, similar to the one shown in figure 5.8 (see page 37). The continuous gradient here is simply because not all rows are illuminated equally. The second column of images is obtained by shifting the LED switch ON time, shifting the start of the illumination. The last column of images is obtained by having a light source that is continuously ON; this means that all rows will eventually have the same exposure time, and thus we get a flat illumination.

After the data acquisition, we proceed by looking at the value of the counts in the shielded bands or the masked edges of the sensor for uniform illumination of the sensor and compare it with the values we have for a dark frame. Figure 6.16 shows this comparison of the dark-region values averaged over the rows (800 rows, discarding the very bottom and the very top of the image) for the odd and the even rows. The blue and the red profiles pertain to the case of uniform illumination as shown in the top right panel of figure 6.15. The green and the black profiles correspond to the dark images.

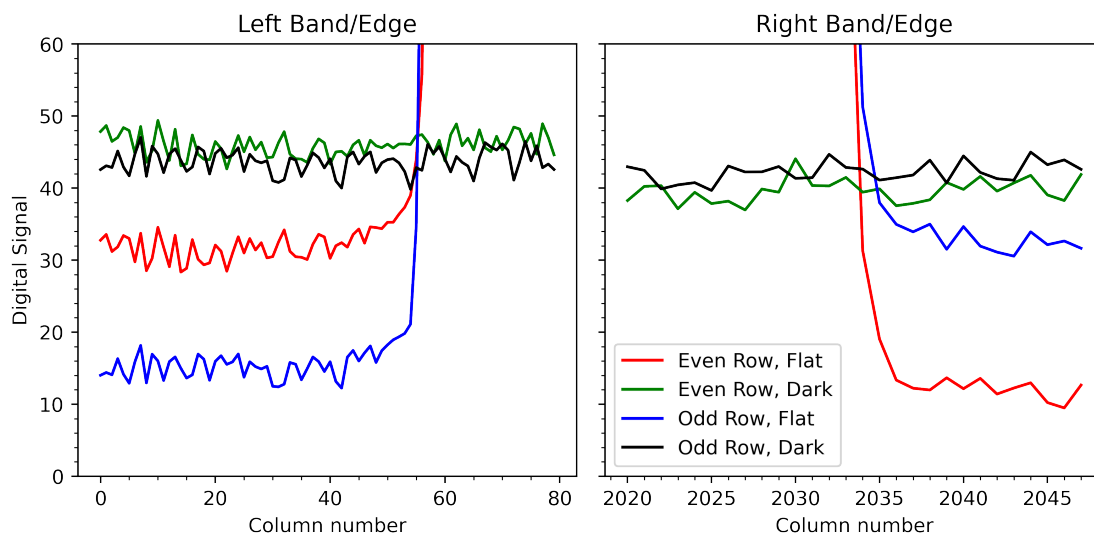


Figure 6.16.: Average profile (averaged over rows) of the dark images and the images with uniform illumination (top right panel of Figure 6.15) along the x-axis in the image. The left plot is for the pixels in the left band, and the right plot is for the pixels in the right band.

Some of the direct inferences that can be made from figure 6.16, are that the counts in the shielded pixels decrease when the sensor is illuminated, as seen by the comparison of the green and the red profiles (for even rows) or the black and the blue profiles, for the odd rows. The green and the black curves are almost similar, showing that the counts in the dark frames are similar for the different sets of rows, but one set of rows shows a more significant gradient in the dark across the sensor as we move from left to right. The black profiles (odd rows) are similar in the left and the right shielded pixels, while the green profiles (even rows) show a marked difference of ~ 10 counts.

The next point is to compare the profiles for the even rows (red and green profiles) in the flat and the dark frame. The value of the count in the shielded pixels goes down when the sensor is illuminated, but the difference (uniformly illuminated frame - dark frame) for the left and the right shielded pixels is not the same. It becomes larger as we move from the left to the right. While for the odd rows (black and blue profiles), this difference between the illuminated and dark frames goes down as we move from the left to the right. Thus the camera has a horizontal gradient in the dark and also in the banding effect (change in the value of the shielded pixels due to sensor illumination). On top of that, this gradient

has a different direction for the odd and the even rows. The other thing to note is that the profiles (red and blue) are flat for the first ~ 35 pixels on the left edge and the last ~ 10 pixels on the right edge, and then start to show a gradual increase, this is due to some scattered light seeping below the mask edges. Nevertheless, the last few columns on the right edge of the sensor can still be used for testing and correction.

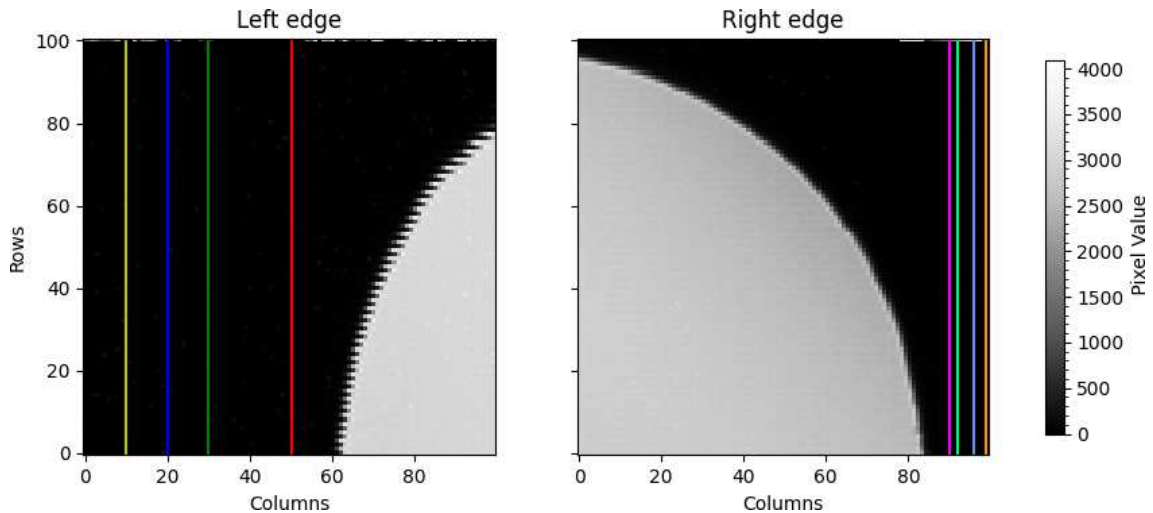


Figure 6.17.: Left and right shielded pixels and selected columns for Figure 6.18. Columns 10, 20, 30, 50 on the left edge and columns 2038, 2040, 2044, 2047 on the right edge.

The next point is to look at the banding effect for different illumination levels. For a first-order analysis, let us consider that all rows (odd and even considered separately) behave similarly. Then the gradient in the first and second column of figure 6.15 can be considered as a proxy for the changing illumination, and the row number becomes a direct index to it. Thus, we will look at the banding effect as a function of the row number for some selected columns within the shielded sensor regions. These columns are marked with different colours in the images shown in figure 6.17, where the image on the left is a crop (100×100 pixels) of the top left corner of the uniformly illuminated sensor. Similarly, the right image is a crop of the top right corner. The issue with the difference in the odd and even rows are seen in the image on the left in figure 6.17, which can be seen as the zig-zag pattern between the dark and bright region. This overemphasised zig-zag pattern is a sensor timing issue which has been solved at a later stage, however it suffices to show that the two set of rows behave independently.

The plots in figure 6.18 show the deviation of the count in the shielded pixels from an averaged dark frame, as a fraction of the mean count of the entire average dark frame, for the selected columns indicated by the different colours in figure 6.17. The left and right plots correspond to the odd and even rows. The first row of plots is for the image shown in the top left panel of figure 6.15, (a). Given that the illumination increases uniformly with the row number, this figure directly shows the deviation of the count in the shielded pixels as a function of the light level. The profiles are different in the left and the right band, not just in the deviation level but also in shape. The profiles are linear only in the first 20% of the entire range of values available for the row number. The increasing separation in the

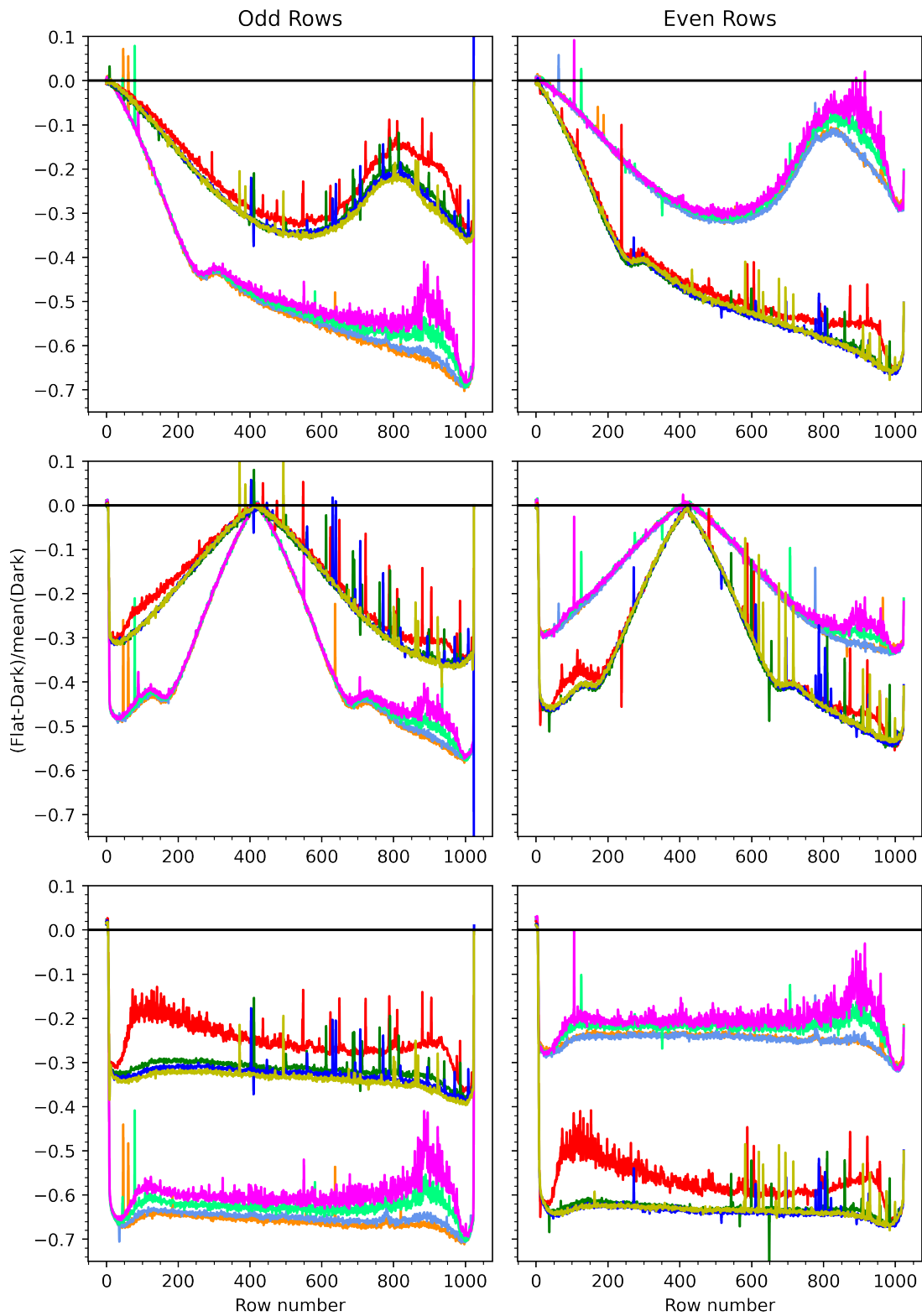


Figure 6.18.: Deviation of the counts in the dark bands in the fully illuminated sensor. With the subfigures (top to bottom) corresponding to the subfigures (top, left to right) in Figure 6.15. The colours represent the selected columns as depicted in Figure 6.17.

profiles for the columns close to the mask edge (red, pink) shows primarily the effect of the scattered light seeping into the shielded pixels. The profiles for the last few columns (light blue and orange) are almost the same, and this is the case for all the images in figure 6.18. This indicates that we can use these last few columns on the left and the right shielded regions for deriving a correction term based on the shift in the dark pixels due to sensor illumination.

The second row of graphs in figure 6.18 corresponds to the image shown in the top middle panel of figure 6.15, (b). There are a few things to note here; the profiles are symmetric about the row having zero illumination, which remains valid for both sets of rows (odd and even). Compare these profiles with the profiles shown in the first row of figure 6.18, and we see that the profiles up to row number ~ 300 in the top row are just shifted in the figures in the second row. This indicates that our assumption that all rows (odd and even separately) behave similarly works for this case. This becomes more evident when we look at the profiles for the selected columns, for a uniformly illuminated sensor (image shown in the top right panel of figure 6.15, (c)), shown in the last row of figure 6.18. All profiles are almost flat, as expected for a flat illumination, which is consistent with what we see in figure 6.16.

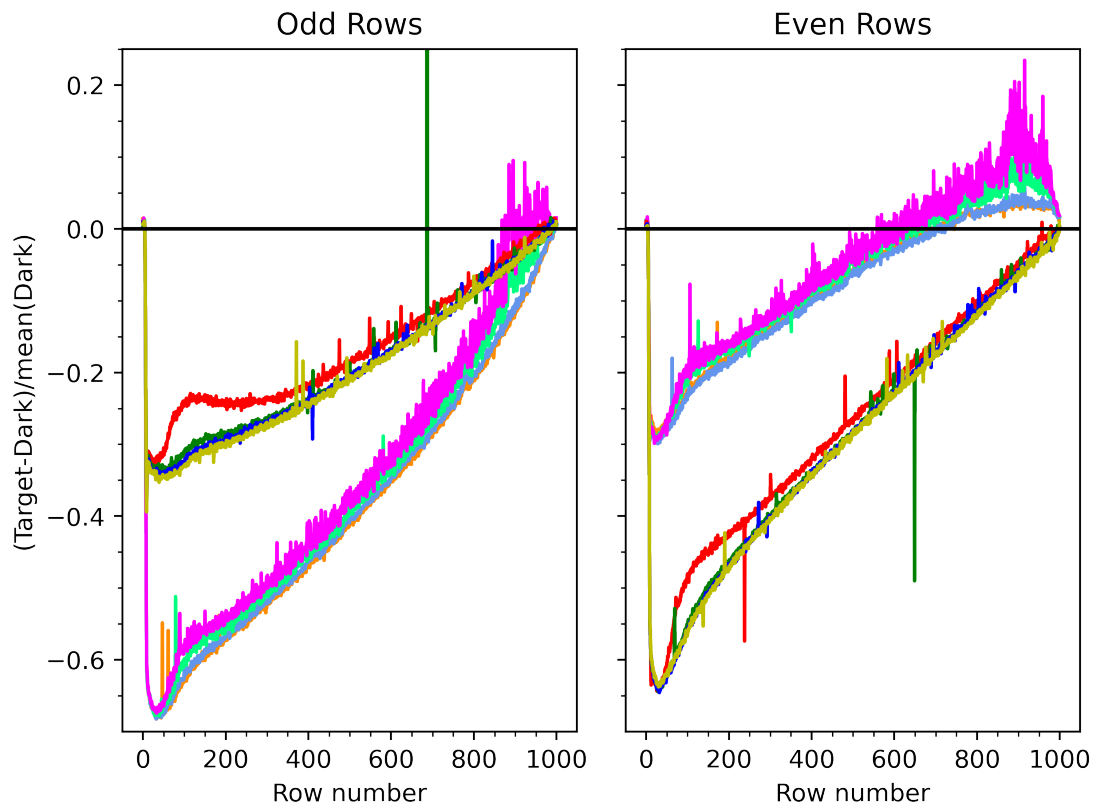


Figure 6.19.: Deviation in the dark bands in the triangular target image, corresponding to the right bottom image in Figure 6.15, (f). The colours represent the selected columns as depicted in Figure 6.17.

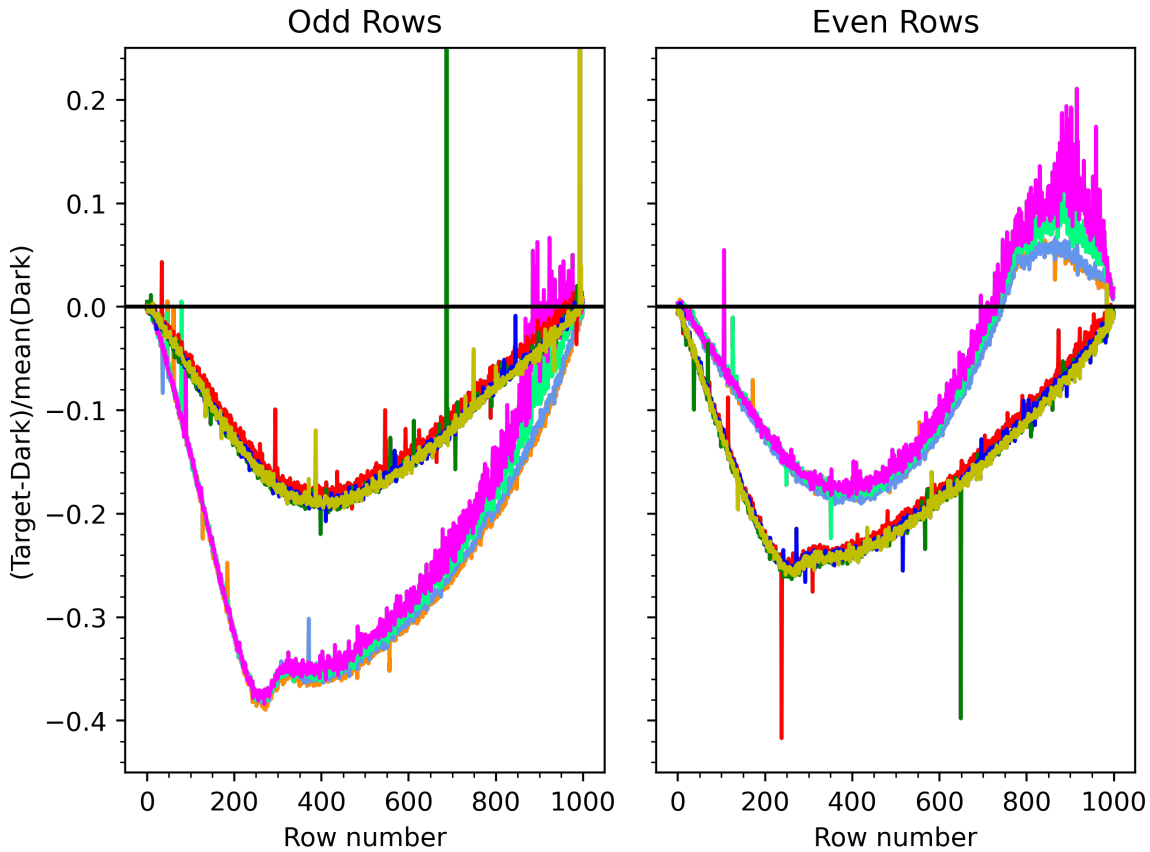


Figure 6.20.: Deviation in the dark bands in the triangular target image with respect to the row number, corresponding to the left bottom image in Figure 6.15, (d). The colours represent the selected columns as depicted in Figure 6.17.

Until now, we just looked at images without any obscuration in the beam path. Figure 6.19 shows the deviation of the signal in the shielded pixels in the triangular target image from an averaged dark frame as a fraction of the mean count in the averaged dark frame. The panels of the figure correspond to the odd and even rows, for the image shown in the bottom right panel of figure 6.15, (f). The selected columns are indicated by different colours, as shown in figure 6.17. The figure shows the effect of the number of illuminated columns and the row average on the non-illuminated pixels. In the previous case, we had all the columns illuminated by a similar illumination in terms of the siblings; that will change for the different rows in this case.

Here, let us start by looking at figure 6.19, where the illumination is constant (maximum, in this case), while the row average and the number of illuminated columns decrease linearly as we go from the bottom edge of the sensor to the top edge, see bottom right panel of figure 6.15, (f). Looking at the profiles, the deviation starts with being close to zero and reaches a maximum (negative) value corresponding to the illuminated bottom rows in the target image. Then a regime of non-linear increase is observed until row number 200 (mostly for the red curve, which is most prone to straylight). Between row numbers 200 and 900, the profiles can be fitted with respect to the row number using at most a second order polynomial. The important point here is that the row number, in this case, is a proxy of the row average, not the sensor illumination. And thus, we can get a

primary handle on the deviation in the shielded pixels due to the row average.

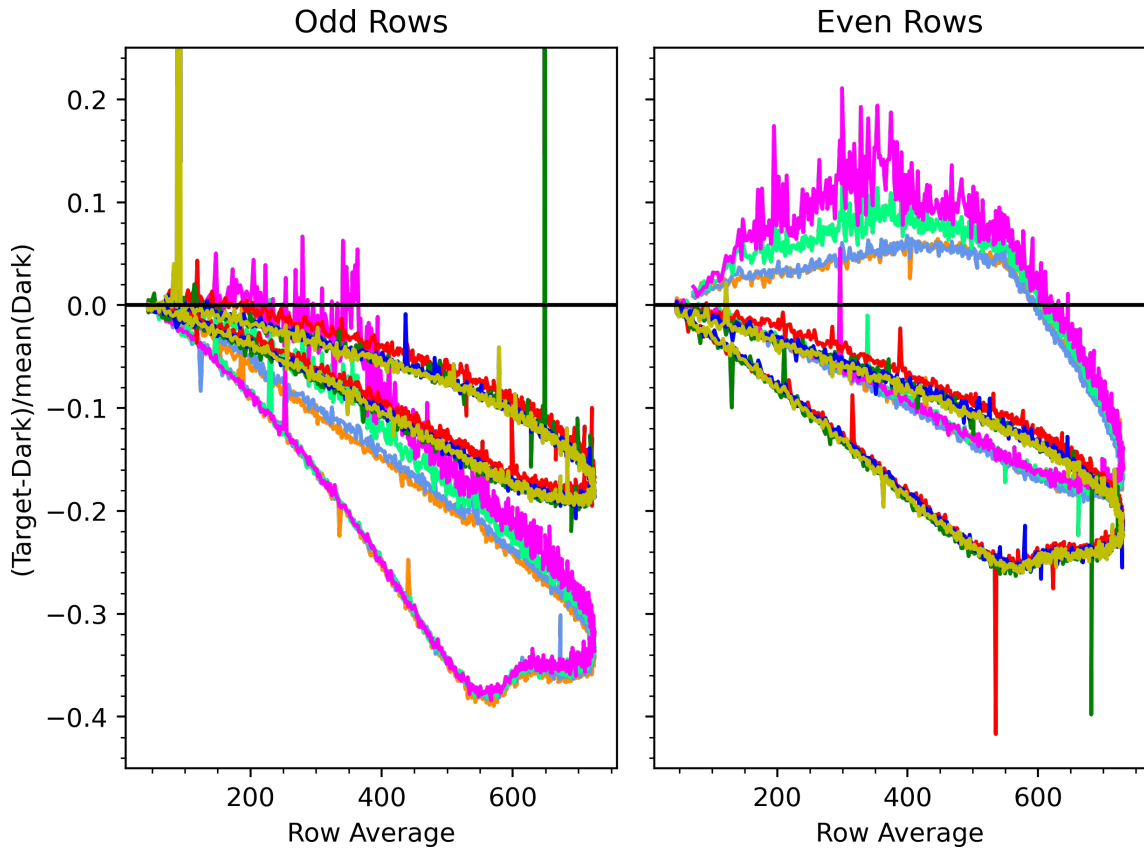


Figure 6.21.: Deviation in the dark bands in the triangular target image with respect to the row average, corresponding to the left bottom image in Figure 6.15, (d). The colours represent the selected columns as depicted in Figure 6.17.

We now proceed with the case of a triangular target, combined with a vertical intensity gradient across the sensor. Figure 6.20 corresponds to this case, see the bottom left image in figure 6.15, (d). Here the row average first increases with the row number, then decreases after reaching a maximum value. On the other hand, the number of simultaneous conversions corresponding to the shielded pixels shows the opposite trend, first a decrease and then an increase with the row number, for reference see section 5.2.2. The deviation profiles first show a decrease as the row average increases with the row number, consistent with what we previously saw. But after a certain point, they return towards the line of zero deviation, marked in black. The important point is that the profiles are not symmetric about this return point. This becomes more evident if the same deviation is plotted against the row average instead of the row number, as in figure 6.21. The two separate branches can be seen for the same row average, primarily because of the different number of illuminated columns in the two branches.

To put everything into perspective, the average dark level in the images was ~ 50 counts, while the average maximum illumination was ~ 3500 counts. Now looking at the extremities of the y-axis in figure 6.18 and figure 6.19 we see that the dark signal shifts by up to

70% of its average value, depending on the average illumination of the sensor.

The next stage is to correct for the deviation in the shielded pixels due to the variation in the light level. Figure 6.22 shows the difference between the top and the lower image in the central panel of figure 6.15 (images b and e). We used a field dependent banding correction as described in section 6.4.3.

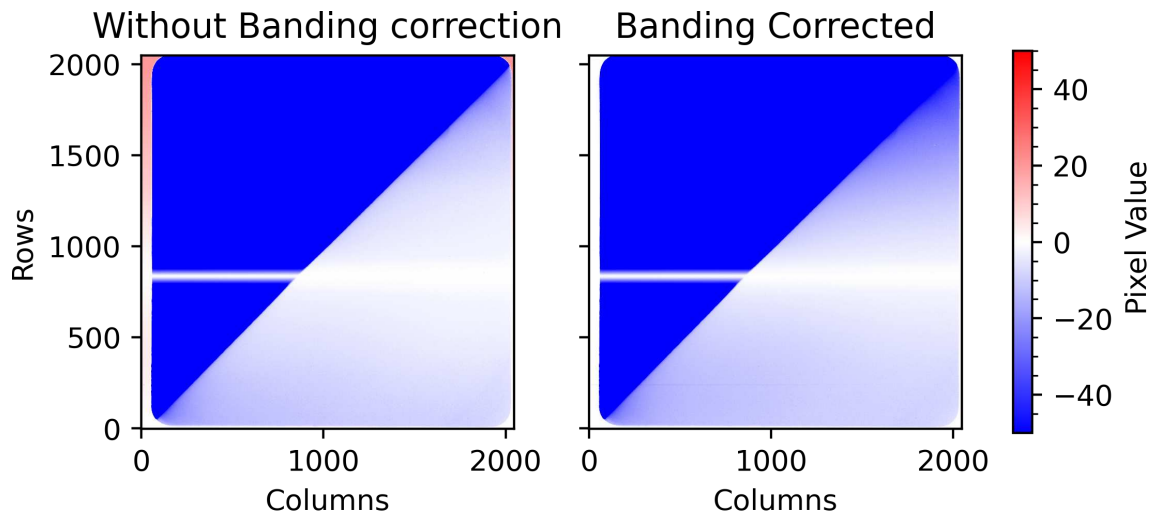


Figure 6.22.: Difference between target and fully illuminated image (a) before banding correction, (b) after banding correction. The colour bar shows the scale of deviation in the shielded pixels.

It can be seen that the shift in the dark pixels is corrected simply using the banding correction as for CAM1, which is what we would expect. The gradient in the always illuminated region has a similar shape in both the cases, before and after banding correction. This is because of a slight shift in the actual brightness of the LED; this leads to this kind of gradient in the always illuminated triangle for a rolling-shutter camera. The good thing is that the banding correction takes away most of the deviation in the dark shielded pixels even after this shift in the LED brightness. The images used for the test are from the central panel of figure 6.15 (b and e), and have a central dark region, thus we see a central white strip in figure 6.22, that will continue into the covered triangular region. It is just another proof that when there is no sensor illumination, there is no deviation in the shielded pixels or the covered triangular region from the average dark.

6.3. CAM3

This camera is a back illuminated, hybrid InGaAs Focal Plane Array, with the detection material made up of InGaAs, mounted on top of silicon readout circuit (please see the manufacturer² website for more details). Once the camera is running at constant gain settings and a fixed frame rate, the first test after the classical calibration (consisting of making a photon transfer curve) is again the triangular target test as for the previous two cameras.

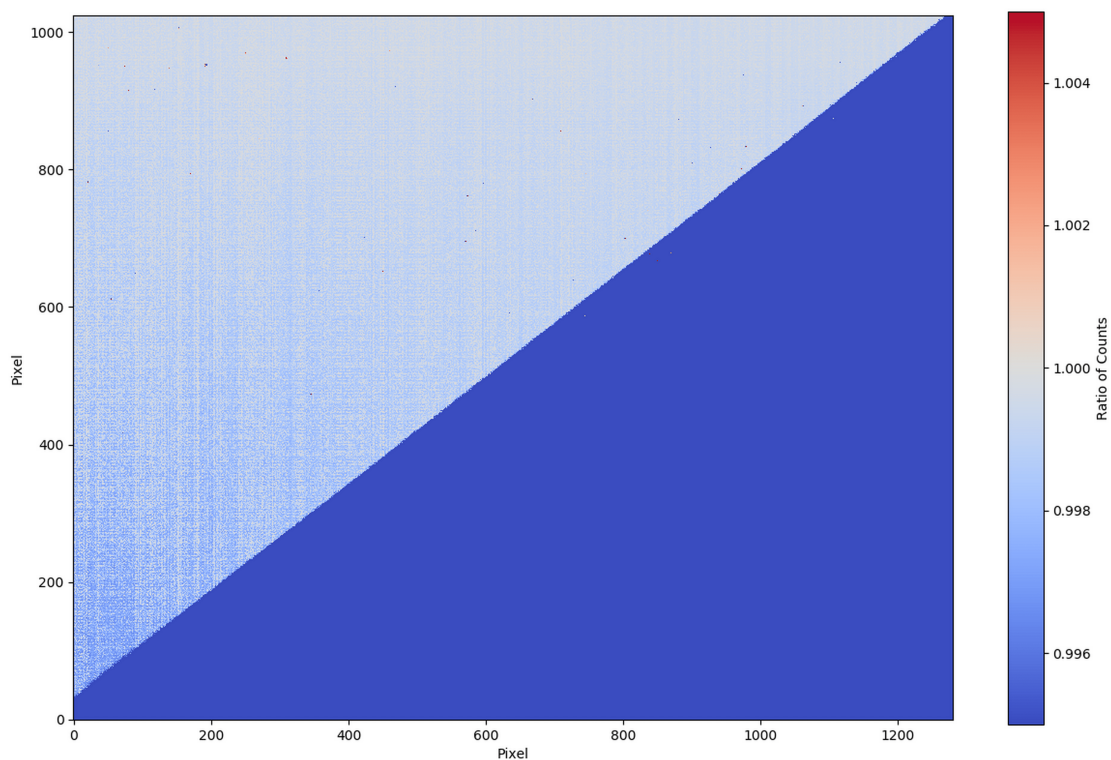


Figure 6.23.: Triangular target comparison for CAM3, with the top left triangle being the always illuminated region.

Figure 6.23 shows the comparison image for a triangular target and uniform illumination of the camera. The gradient (in the vertical direction) can be easily seen in the always illuminated region (light blue). Although the level of deviation is not as significant as the other cameras, it is still there. In this case, the effect is of the order of 0.1-0.3%, which is an order of magnitude less than that seen for the other two cameras, and this level was deemed sufficient for the camera use case (GRIS+, an upgrade to GRIS, Dominguez-Tagle et al. 2022).

²<https://www.princetonirtech.com/products/1280scicam>

6.4. Schemes of Camera Calibration and Data Correction.

Ultimately what we want is a workable calibration profile for the sensor, that accounts for the non-linearities shown by the sensor, a mapping between the count of pixel, the light sensor illumination and any other parameter that might effect the pixel count. Reaching that point is a lengthy process, where we start with the standard techniques of sensor characterisation which have been there since the development of the first imaging sensors. However as the sensors have become more and more complex, so have the problems with these sensors. We discuss the calibration techniques for these effects here.

6.4.1. Standard, Non-linearity Map w.r.t Integration Time, and Gain Maps

The standard camera calibration techniques try to make a non-linearity correction with respect to the integration time of the sensor. The light source is kept in the ON state, and the integration time of the camera is changed to get a profile of counts with respect to the integration time. But in most applications we keep a fixed exposure time, and hence we need a calibration with respect to the light illumination of the camera. Furthermore changing the exposure time changes the sensor temperature, and the working conditions of the sensor, thus not an ideal situation.

6.4.2. Basic, Pixel by Pixel Non-Linearity Map w.r.t Light Level, and Gain Maps

For a light sensor, the ideal approach is to make a profile of counts for the intensity of the light source. This should be done for each pixel individually for an imaging array; this is the more relevant case of camera calibration. Most often, all pixels are treated as one and the same to get an overall idea of how one sensor differs from the other. The average pixel response w.r.t. the light level would tell the difference between the light response of the sensors, and the variance would tell how similar are the pixels to each other. However, the suggested case is still to at least make pixel individual non-linearity curves (pixel counts with respect to the sensor illumination).

6.4.3. Banding Correction

Running the three-light source setup is expensive in terms of data storage and time, and thus for applications where we do not need to bring the non-linearity to a level of 10^{-4} or below, we can make due by taking out the general trends or dependencies, assuming that all rows work in the same fashion.

Basic Banding Correction Take the average of the deviation in the shielded pixels in a row, and just fix this deviation for all the pixels in the row. This takes away most of the dependence on the row average.

$$Image(corrected) = Image(original) - Average(Image - Dark image)_{Shielded\ Pixels} \quad (6.7)$$

Field Dependent Banding, Depending on Camera Calculate the deviation in the shielded pixels in the masked edges, fit a linear profile to this deviation, as a function of the pixel position in the row. Correct the count in the pixels with this profile.

$$p = \text{polynomial fit}(\text{Image} - \text{Dark image})_{\text{Shielded Pixels with pixel position in row}}$$

$$\text{Pixel count}(\text{corrected}) = \text{Pixel count}(\text{original}) - p(\text{pixel position})_{\text{per row}} \quad (6.8)$$

Making these corrections mostly accounts for the affect of the row-average, in the bias deviation. Although all rows can be considered to behave similarly and an average correction can be obtained it is suggested to make the banding correction on a row by row basis.

6.4.4. Calibration With Respect to Light Level, Row Average and Siblings

The most straightforward approach here is to directly fit a three-dimensional polynomial of appropriate degree, which depends on how densely we traverse the parameter space. This method is readily applicable to the acquired data. We calculate the row average and the number of siblings for each pixel in the test image or the image to be corrected and use the fitting function obtained from the calibration data.

The better approach is to first make a fit for the counts with respect to the illumination. For this, we consider the entire data set, consisting of the data for all the different illumination conditions. This has to be done for each pixel individually. This accounts for the average response of the pixel under all the different illumination conditions. Now this will act as a reference point.

From this reference point, we calculate the deviation of the pixel count for each pixel, as the row average and the siblings vary under the different illumination conditions. Then we make a fit of these deviations in the count with respect to the row average and the number of siblings for each pixel. This has to be done per light level. Thus finally, we have two parts to the fitting function, one is the reference part (for the light level fit), and the second is the part of the deviation from this reference. The problem is that it is not readily applicable to the test data. The pixel count indicates the secondary part of the fit function to be used given by the equation below, where $f(\text{counts})$ is a function of the pixel counts. While $g(\text{row average, siblings})$ is a function of the row average and the siblings, it differs in different count ranges.

$$\text{output light level} = f(\text{counts}) + g(\text{row average, siblings})_{\text{counts}} \quad (6.9)$$

The difference between the two approaches is that in the second approach we remove lot of the free parameters like $C_{2,2,2}$ and just keep paremeters like $C_{2,0,0}$ in equation 6.1. We can also directly formulate the problem after removing these coeffecients from equation 6.1, and solve it directly. The main point is that we would need a large number of data points in the parameter space for the fitting to correctly work with a large number of coefficients. For simplicity take the example of trying to fit a third order polynomial for 3 data points.

6.4.5. Defective Pixel Map, Correction

All sensors will have some defective pixels that have a pixel response very different from the average pixel response of the sensor. This needs to be corrected to get a uniform light response profile for the sensor. The suggested point to make this correction is after all the fitting and calibration process has been done. The simple reasoning in doing so is that these pixels too affect the behaviour of the sensor; they affect the row average and the number of siblings. Thus only after calculating all the needed parameters, and making the above-stated corrections, should these pixels be discarded or replaced with average values of the surrounding pixels.

6.5. Discussion

We have shown that the three tested CMOS camera types with a highly multiplexed read-out show some kind of non-linear scene dependence in their response. Moreover, we can get information about the level of the deviations from a linear response with a rather simple procedure by projecting suitable targets onto the sensor. Some corrections can also be made using the obtained data from these deductive targets. We can also make banding correction that accounts for most of the bias level shift and does not require any extensive calibration data set, as done for CAM2. It has to be pointed out that most of the literature on camera calibration deals with an independent linearization of the response of individual pixels, and most calibration processes are directed at doing that, for example see (Wang and Theuwissen 2017, Soman et al. 2015). Bohndiek et al. (2008) shows the extensive analysis of the various methods of calculating conversion gain and how the inherent camera non-linearity affects these calculations. Herrmann et al. (2022) gives an overview of standard camera calibration techniques. Wang (2018) provides a thorough analysis of pixel linearity and looks at various pixel architectures. That approach of starting from pixel architecture and studying the non-linearity in a pixel is important, but that is only possible if we know the actual architecture, which is often not the case. Hence a setup that can probe the sensor architecture at least to the first order is required.

During this work, we have realised the importance of looking at the pixel response under different illumination scenarios (scenes). In simple terms, the scene dependence adds to the temporal variance (across different frames for the same illumination) of a pixel as each frame would have a different number of siblings because the photons falling onto the pixel is a statistical process. And accounting for the scene dependence will ideally lead to a decrease in this variance. We can see this effect in figure 6.6 where the peaks for the data recovered after fitting are narrower than the original data. Here, we show the spatial variance as a proxy for the temporal variance under the assumption of homogeneous illumination as a first-order test. Looking at spatial variance is better as we can compare different areas of the sensor (each having its homogenous illumination) at the same time.

To comply with the accuracy requirements of solar polarimetry, we need to characterize and eventually suppress these non-linearities at least to the level of 10^{-3} (see also the paragraph on polarimetric accuracy below). This needs to be done for the sensor under different illumination scenes. That requires spanning the entire parameter space as densely

as possible. However, even if we take 10 steps in each direction (row-average and siblings) and 10 light levels, we are already looking at 1000 measurements, and at each state, say we take 1000 images, we are looking at a data set of 10^6 images. As the photons falling onto the pixel is a statistical process, we need a large number of images under the same illumination scene, to have a proper statistical sample. Handling this data set becomes difficult as the number of images and the number of light-level samples increases. Furthermore, all of this is for that small calibration region shown in figure 6.7. We must move this region around to calibrate the entire sensor or cross-calibrate the light sources. This means that we need to handle an enormous amount of data if we try to work with all of these images. This is not only a problem in storing the data, but even analysing it as the read time of these images in the analysis codes will also be large.

There is a way to circumvent the problem, and it is to store the relevant data for each pixel; instead of saving images for each target, we make histograms that save the count, the row averages, and the siblings for each pixel. Thus a set of 1000 images is just one histogram, and the advantage of histogramming is that the data volume remains constant even if we take a larger number of images per target or light level, while it linearly increases if we save raw data. The ideal solution is to do the fitting in parallel with the data acquisition. This has been tested for one set of fitting functions, and it worked flawlessly in terms of the setup stability. The only problem was that the fitting function we chose was not entirely suitable to the data. Doing an online fitting during data acquisition means that we cannot try different fitting functions, or we need to run the calibration again. Thus histogramming is a middle ground between saving all images or saving no data.

The other problem lies in the fitting routines; directly fitting a three-dimensional surface to the obtained data set most often fails (it will not work for some light levels). The point here is that we need a fifth-order polynomial in the light level, a third-order in the row average and a first-order in the siblings for a good calibration. This means that the resultant 3-dimensional polynomial will have many coefficients. We will need an equivalently dense sampling of the parameter space for this fitting to work properly. Currently, the adopted solution is to fit the surface for each light level individually after making a reference light level fit using the complete data set. This is a two-step process; although this works, the correction method becomes a bit cumbersome. Another viable solution is to look at mapping techniques or machine learning, as a mapping between the count, light level, row average, and siblings can be developed even if the polynomial fits do not lead us to the intended results.

The non-linearity calibration method applied in this thesis can be considered a proof of concept. The full calibration process was applied only for one camera type to demonstrate the method's feasibility. Some additional practical steps are required to render the calibration fully applicable to solar polarimetric data. The main steps include extending the calibration to the full sensor area and to the different CMOS camera types used in our instrumentation.

We have developed a setup that probes cameras across a sufficiently large intensity range and allows to fully characterize the sensor non-linearities. We have demonstrated that these

non-linearities are reproducible and can thus be corrected in terms of a calibration. We have shown that after calibration, the residual deviations from an ideal linear sensor response are suppressed down to a level of 10^{-4} . This level is sufficient in practice, as most often, other instrumental factors will limit the polarimetric accuracy to a level of 10^{-4} . This fact becomes apparent if we look at the non-linearity model presented in (Keller 1996), where the polarimetric accuracy scales with the non-linearity and with the absolute degree of polarization. A residual non-linearity of order 10^{-4} would allow reaching a polarimetric accuracy of 10^{-5} , even in the presence of large instrumental polarization of order 10%. Therefore the level of non-linearity correction demonstrated in the thesis is more than sufficient for basically all practical cases.

7 Results: General Properties of Sunspots

7.1. Introduction

Sunspots consist of an umbra that is dark relative to the quiet photosphere. It is surrounded by a penumbra that is intermediate in brightness. The umbra harbours a strong, rather homogeneous and relatively vertical magnetic field. The penumbra is much more inhomogeneous than the umbra, with patches of strong, umbral-like magnetic field associated with dark, cool gas (the spines) interlaced with generally brighter regions, where the magnetic field is complex but much more horizontal (the penumbral filaments) (Title et al. 1993, Solanki and Montavon 1993, Lites et al. 1993, Tiwari et al. 2013). Both the umbra and the penumbra exhibit magnetoconvection. In the umbra, convection occurs predominantly within the small, bright umbral dots (Danielson 1964, Parker 1979, Choudhuri 1986, Schüssler and Vögler 2006, Bharti et al. 2010a). The penumbral filaments are now recognized as products of magnetoconvection (Scharmer et al. 2008, Zakharov et al. 2008, Rempel et al. 2009, Rempel 2011, Rempel and Cheung 2014), with the Evershed flow, an almost horizontal outflow along their central axis, being the most prominent magnetoconvective flow they harbour (e.g., Borrero et al. 2004, 2005, Bello González et al. 2005).

It is not clear yet, why there is such a sudden transition from the umbra to the penumbra. Jurčák (2011) and Jurčák et al. (2018) observed that the vertical magnetic field B_z averaged along the umbra-penumbra (UP) boundary assumes a constant value that is independent of the size of the sunspot. This motivated the theory that there is a critical value of B_z for the onset of magnetoconvection (the so-called Jurčák criterion). However, Löptien et al. (2020) interpreted this constant value of the averaged B_z to be caused by the brightness of penumbral filaments varying between spots of different sizes. Most observables are remarkably uniform between different penumbral filaments, but the brightness of the penumbral filaments depends on the size of the sunspot (Löptien et al. 2021). The larger the sunspot, the darker the penumbral filaments. Löptien et al. (2021) also noticed that there is a smooth transition from umbral dots to penumbral filaments, with no obvious discontinuity at the UP boundary. These results indicate that explaining the transition from the umbra to the penumbra does require not only a characterisation of the UP boundary itself but also an understanding of the global properties of sunspots.

A straightforward way to quantify the properties of different sunspots is to compute radial profiles of different parameters across the spot. This approach has been used extensively

to study the structure of the magnetic field within the penumbra and its dependence on optical depth (Lites and Skumanich 1990, McPherson et al. 1992, Solanki et al. 1992, Balthasar and Schmidt 1993, Hewagama et al. 1993, Keppens and Martinez Pillet 1996, Rueedi et al. 1998, Westendorp Plaza et al. 2001b, Mathew et al. 2003, Borrero et al. 2004, Bellot Rubio et al. 2004, Sánchez Cuberes et al. 2005, Langhans et al. 2005, Borrero and Ichimoto 2011, Tiwari et al. 2015, Joshi et al. 2017). Similarly, radial profiles of the Doppler velocity for sunspots away from disk center can be used to quantify the Evershed flow (Bellot Rubio et al. 2003, Borrero et al. 2004, Bellot Rubio et al. 2004, Borrero et al. 2005). However, a detailed analysis of how these radial profiles vary between spots of different sizes is still missing. In this study, we address this question using observations obtained by the spectropolarimeter onboard the Hinode satellite. First, we examine the azimuthally averaged observables at both the inner and the outer penumbral boundary and extend the analysis to multiple optical depths. In the next step, we compute radial profiles of different parameters and evaluate their dependence on optical depth and on the size of the sunspot.

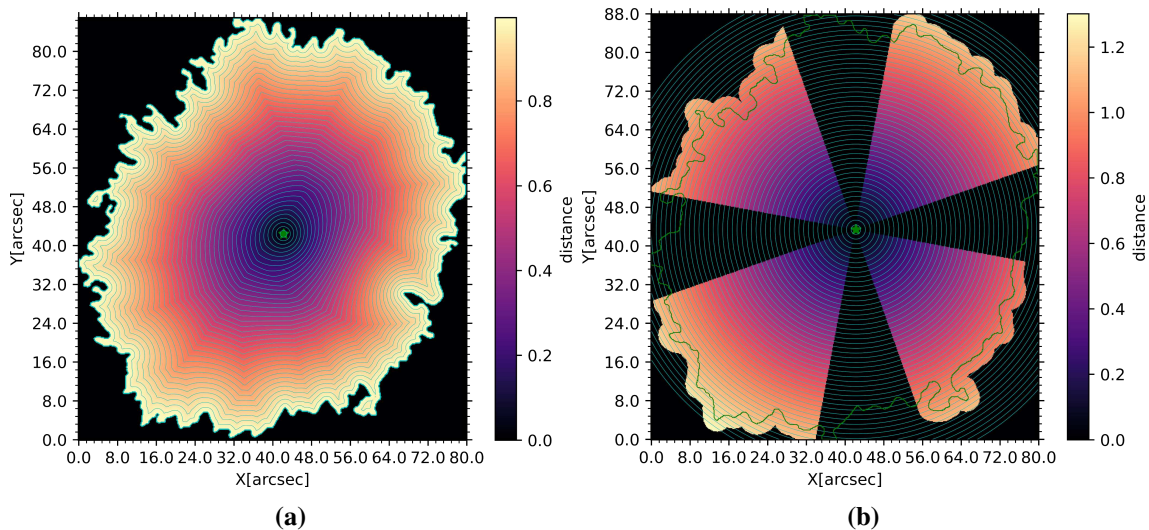


Figure 7.1.: Methods of defining distance contours in the spot, (a) distance from the centre of the spot to its outer boundary, with each point on the outer boundary defined as 1 on the normalisation scale. (b) distance normalised from the centre of the spot to the outer boundary, but, normalisation is done separately along the major and the minor axis of the spot, with the average distance along the desired part of the curve as the normalising factor.

7.2. Observations and Data Analysis

The data set contains 38 sunspots observed by the spectropolarimeter (SP) onboard the Hinode satellite from 2006 to 2012. Appendix C gives a complete list of the selected regions. A further selection from this list of spots was done to consider only complete spots and simple sunspots with a regular shape. The spectropolarimetric scans obtained by Hinode/SP were inverted using the spatially coupled inversion technique as discussed in van Noort (2012), incorporated into the SPINOR code (Frutiger et al. 2000), which uses

the STOPRO routines to solve the radiative transfer equations for polarized light (Solanki 1987). The inversions provide the physical properties of the solar photosphere at three inversion nodes, placed at $\log(\tau) = -2.5, -0.9, 0.0$, with τ being the continuum optical depth at $\lambda = 6302 \text{ \AA}$. The 180° ambiguity in the azimuth for the inverted data was solved using the non-potential magnetic field computation method (NPFC, Georgoulis 2005).

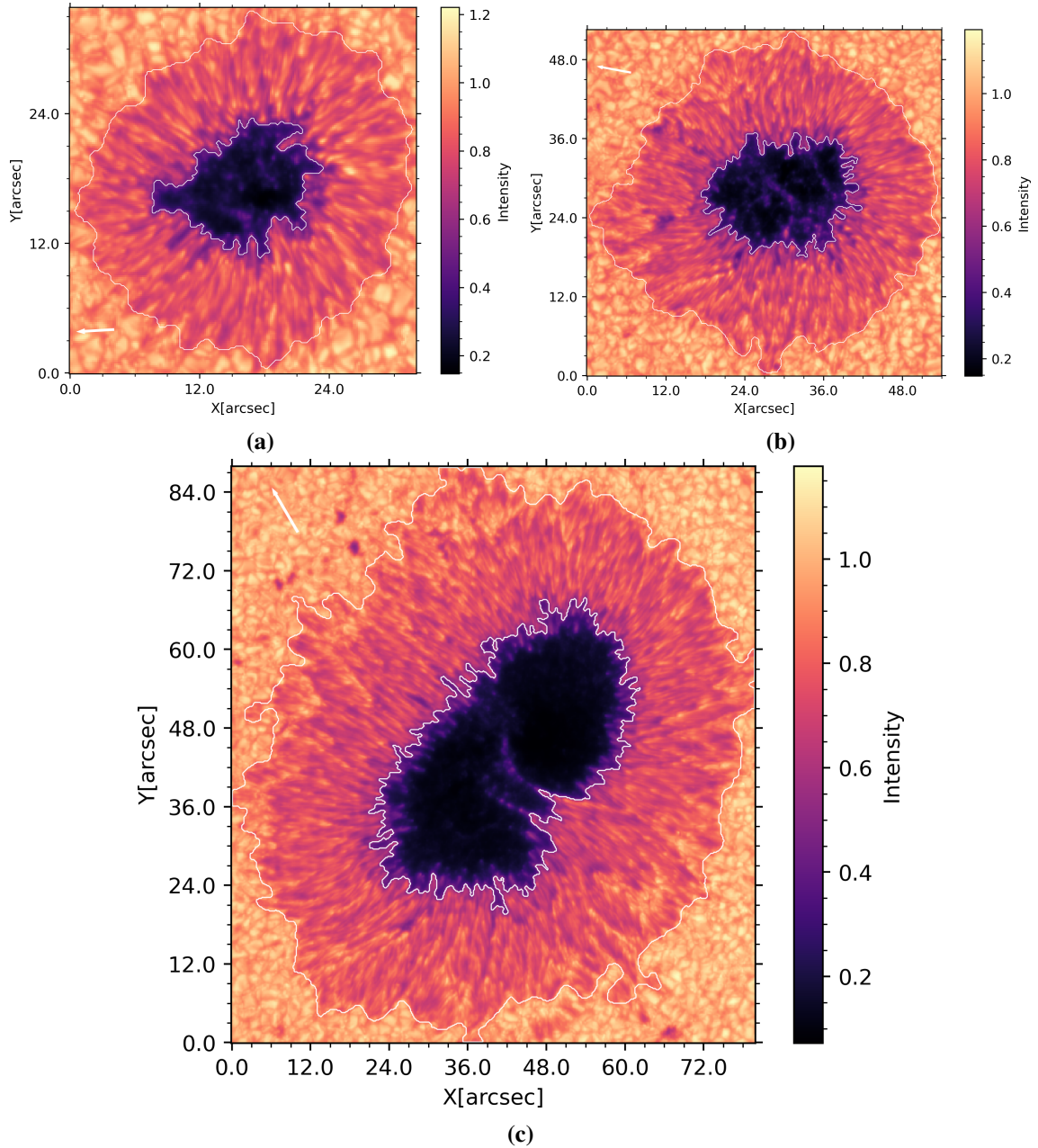


Figure 7.2.: Continuum intensity (a,b,c) maps of a small, a medium and a large spot, respectively. The contours show the inner and the outer penumbra boundary.

For our study of the magnetic properties of the penumbra, we selected only the spots lying within 40° of the disc centre. Furthermore, we only considered spots having a single umbra, mainly to remove the complications from light bridges when considering

the radial dependences. We studied the variation of different physical quantities at the umbra-penumbra boundary by defining it as a constant intensity contour at 0.5 of the normalised intensity. The intensity normalisation is done with respect to the intensity of the quiet Sun region in the image. The outer penumbra boundary was determined at a constant intensity contour of 0.9 of the normalised intensity after the image was first smoothed using a 4×4 uniform intensity filter.

For studying the physical properties across the penumbra, we started by defining the centre of mass of the total magnetic field at the central inversion node, as the centre of the sunspot. Then we determined contours around this centre, each located at a fixed fraction of the radial distance to the outer edge of the penumbra. Figure 7.1a shows the contours derived in this manner for a sample sunspot. Averaging the values of different quantities along these contour lines gives an average profile of the physical quantities with respect to the distance from the centre of the spot. The contours were drawn at a grid of higher resolution than the image and finally, the pixels lying on the contours were selected for averaging. For further investigation, we normalised the radial distance scale to 0 at the centre and 1 at the outer penumbra boundary.

The disadvantage of determining the radial distance in this manner is that individual contours may cover both the inner penumbra and outer umbra, especially for elongated spots. To better treat such spots, we also studied the penumbra by dividing it into a clover leaf pattern, with two of the leaves oriented along the major and the other two along the minor axis of the spot, as can be seen from Figure 7.1b. In such cases, the contours are chosen to be circular. The normalisation of the distance to the outer penumbral boundary is done separately along the two sets of clover leaves, with the radius of the spot along one of the leaves being the distance averaged over the length of the arc covered by that leaf, with each leaf having an angular extent of 60° .

In order to determine the dependence of various physical parameters and their averages on the spot size, the profiles were binned into three categories, small spots with umbral areas lying in the range $20 - 80 \text{ Mm}^2$ (5 spots). Medium spots are the ones between $100 - 200 \text{ Mm}^2$ (3 spots), and large ones have an area above 400 Mm^2 (5 spots). Continuum intensity profiles for three example spots are shown in figure 7.2, while figure 7.3 shows the maps for the magnetic field strength and its vertical component for the three example spots. The bins were chosen by looking at the bunching of points in figure 7.4.

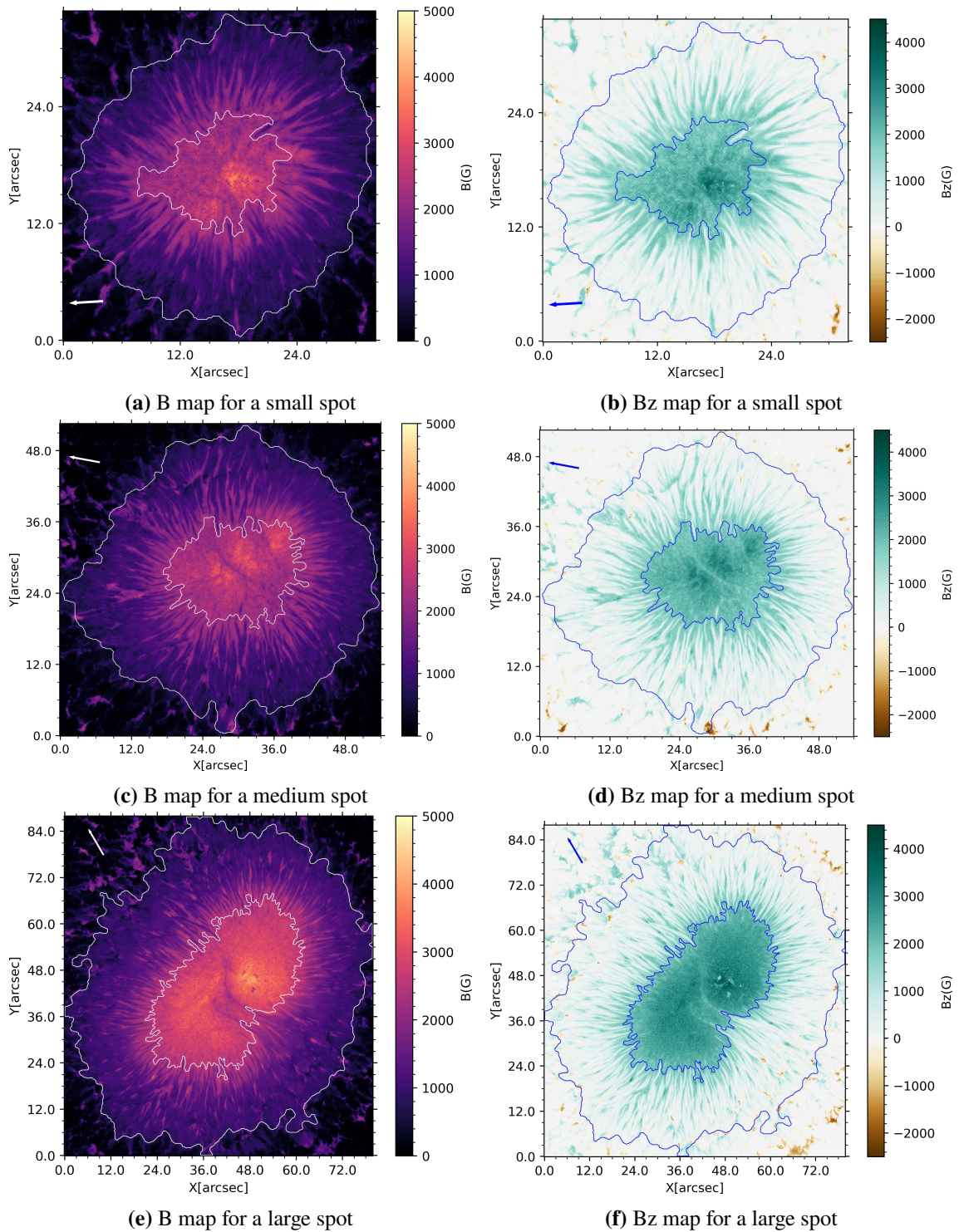


Figure 7.3.: Magnetic field strength (a,c,e) and vertical component of the field (b,d,f) maps for small, medium and large spots, respectively, at the central inversion node. The contours show the inner and the outer penumbra boundary, and the arrow points to the solar centre.

7.3. Results

7.3.1. Physical Properties at Umbra-Penumbra Boundary With Respect to Area of the Umbra

In this section, we explore how azimuthal averages of various observables along the umbra-penumbra penumbra boundary depend on the size of the umbra of the sunspot (see Figs. 7.4 and 7.5). The value of the magnetic field strength at the umbra-penumbra boundary increases with the area of the umbra, as seen in figure 7.4a. While the (negative) gradient of the magnetic field strength with respect to height decreases with the size of the umbra.

Figure 7.4b shows the vertical component of the magnetic field at the umbra-penumbra boundary with respect to the umbral area, and if we consider umbrae having an area above 3 Mm^2 , as done by Jurčák et al. (2018), we get a value for $B_z \sim 1820 \pm 17 \text{ G}$ at the central node with a slope of $\sim 0.08 \pm 0.07 \text{ G/Mm}^2$. While the top two (blue and green) nodes have a positive slope, the bottom-most node (red) has a small negative slope with the area of the umbra. These slopes seem to be blown out of scale when we plot the umbral area on a log axis; on the linear scale, these slopes are very small, as given by the value for the central node. The (negative) gradient of the vertical magnetic field with respect to height decreases with the size of the umbra, which is similar to the behaviour of the magnetic field strength.

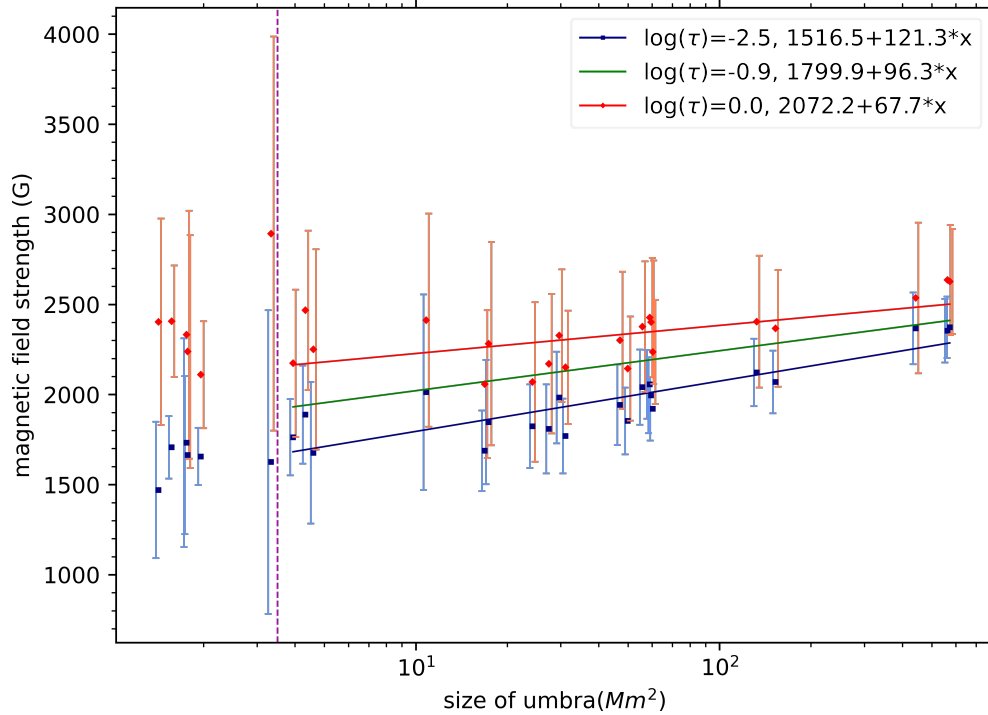
Figure 7.5a shows an increase in the inclination at the umbral boundary with the umbral area. The inclination increase with the umbral area is similar at all three nodes, while the bottom-most node has a higher inclination, i.e. a more horizontal field. Such a dependence is expected for the inclination based on Fig. 7.4. The increasing field strength with the umbral area can be matched with a nearly independent vertical magnetic field only if the field's inclination at the umbral boundary also increases with the umbral area.

The temperature at the umbra penumbra boundary for the central node shows negligible dependence on the umbral area. This is not surprising, given the criterion of constant contrast used to select the umbral boundary. The bottom and the top node show a positive and negative dependence on the umbral area (Fig. 7.5b), respectively. Thus the (negative) gradient of the temperature with height increases with the area of the umbra.

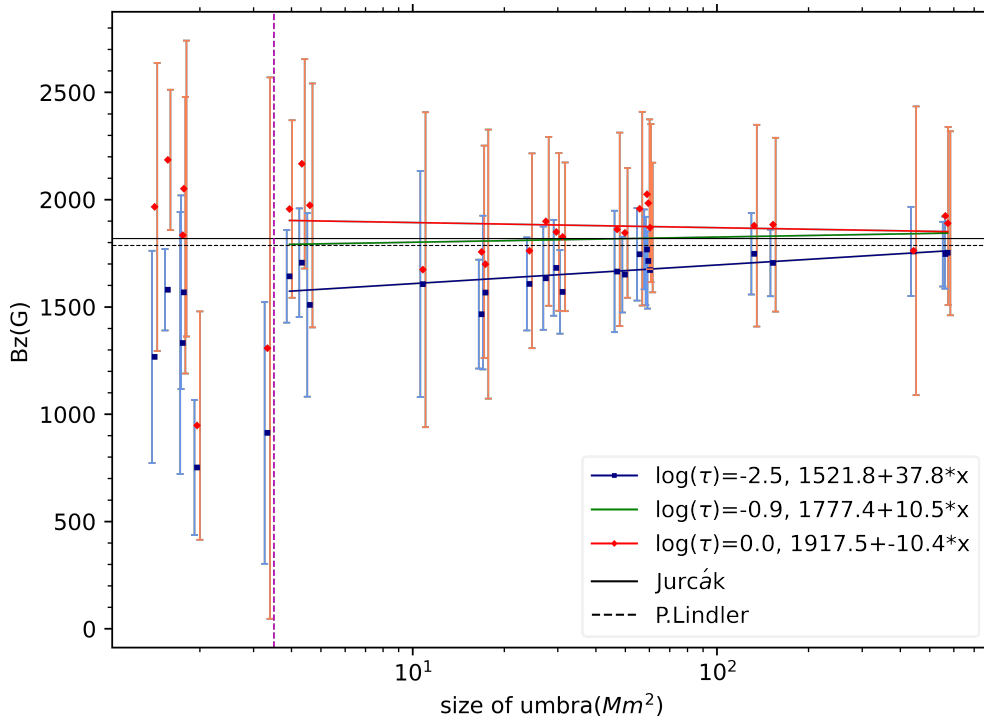
7.3.2. Physical Properties at Outer Penumbra Boundary With Respect to Area of the Spot

Here, we evaluate how various observables depend on the area of the sunspot when averaging them over the outer penumbral boundary (see figure 7.6 and 7.7). The magnetic field strength with respect to the size of the spot decreases at all three nodes, but the rate of decrease is highest for the central node, as seen in figure 7.6a.

The vertical magnetic field with respect to the size of the spot decreases and goes from positive to slightly negative at the outer penumbra boundary at the lowest node, as shown



(a) Magnetic field strength



(b) Vertical magnetic field

Figure 7.4.: (a) Magnetic field strength averaged along the umbra penumbra boundary, (b) similarly averaged vertical magnetic field plotted vs the sunspot umbral area. The error bars are the standard deviation of the values along the boundary. The fitted lines just consider umbras above an area of $3 Mm^2$ (as indicated by the vertical dashed lines), and the fitted lines and the values listed in the plot legend are for a linear fit with respect to $x = \log(\text{umbral area})$. The three colours represent the three inversion nodes, as shown in the plot legend. In panel (b) the solid black line shows the results obtained by Jurčák et al. (2018), while the dotted line is from Lindner et al. (2020).

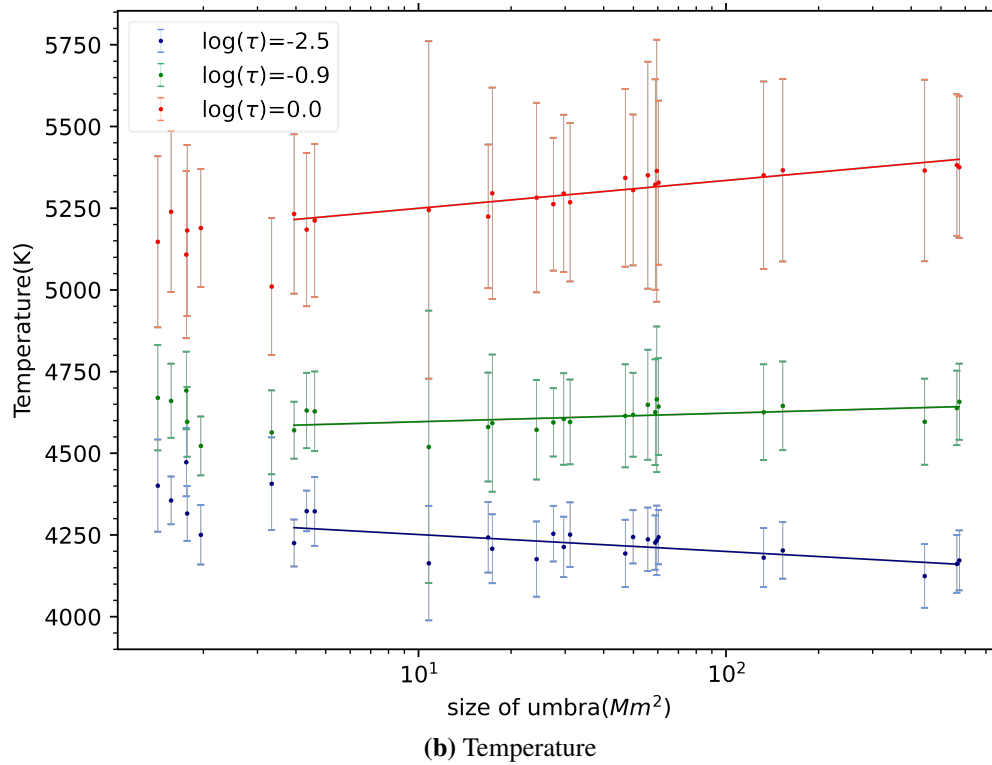
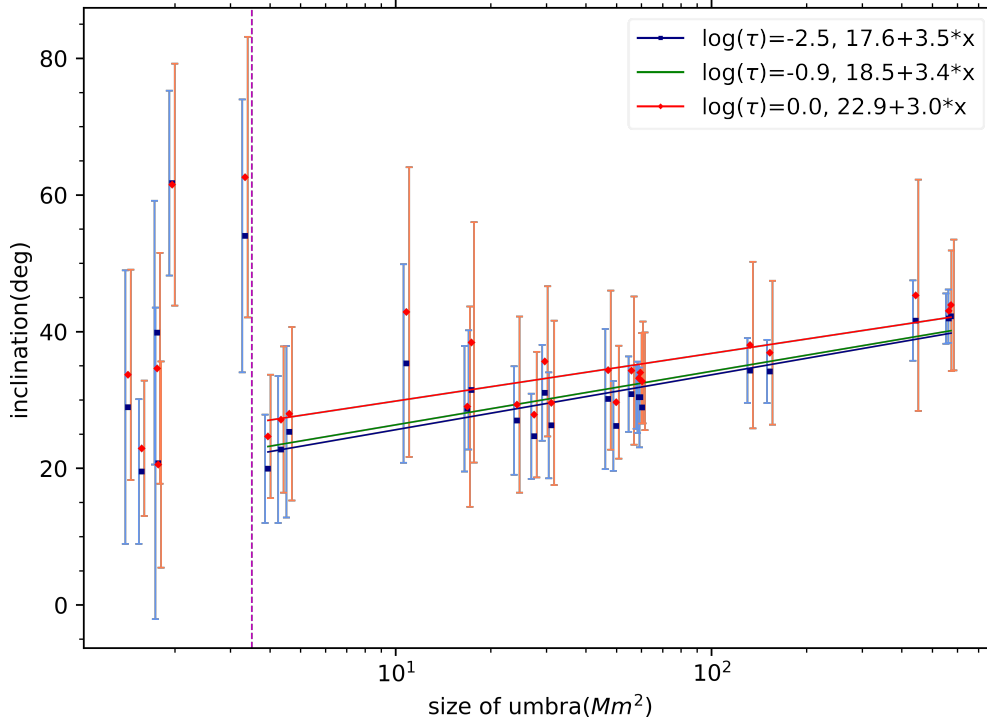
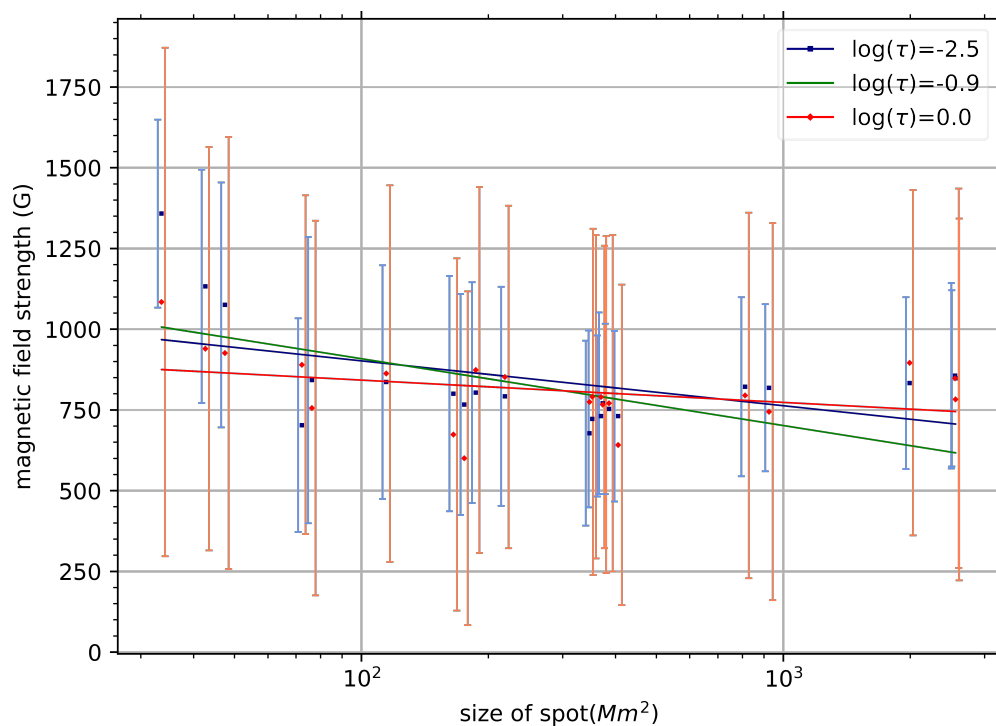
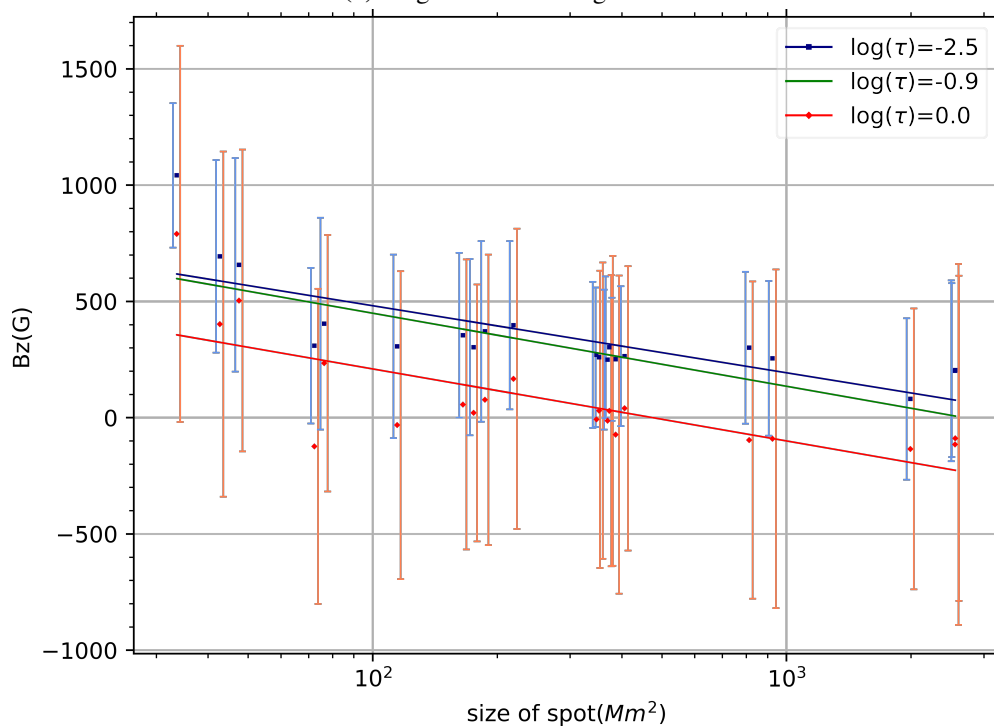


Figure 7.5.: The same as Fig. 7.4, but for (a) inclination and (b) temperature, both averaged along the umbra-penumbral boundary. The lines show linear fits with $x = \log(\text{umbral area})$.

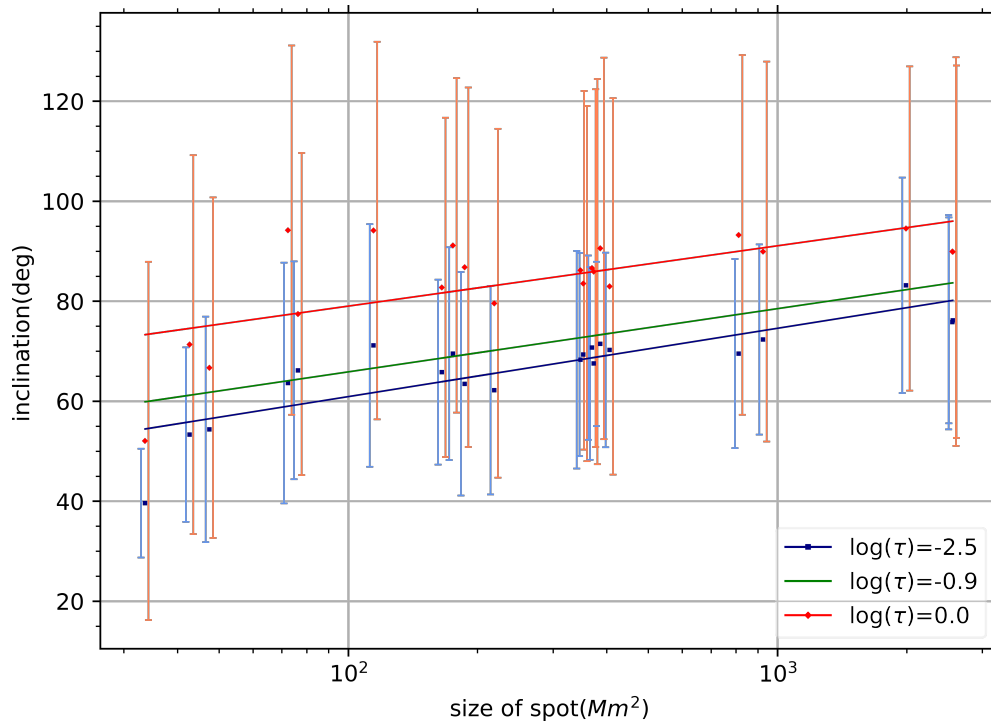


(a) Magnetic field strength

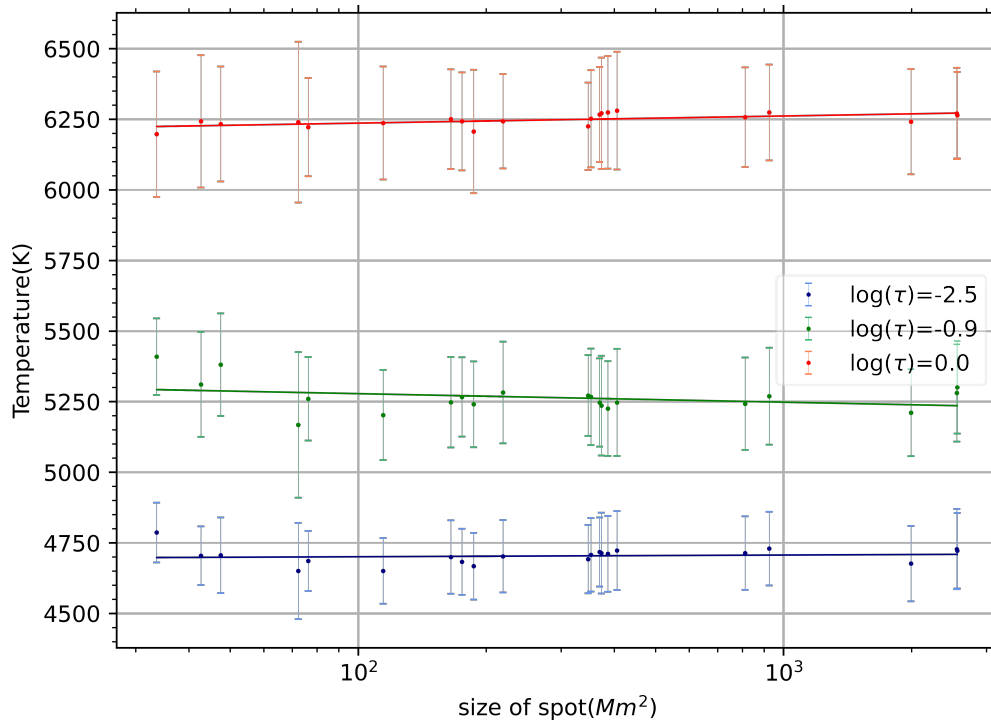


(b) Vertical magnetic field

Figure 7.6.: (a) Magnetic field strength, (b) Vertical magnetic field, averaged along the outer penumbra boundary (0.9 of the normalised Intensity) vs the area of the sunspot. The error bars are the standard deviation of the values along the boundary. The lines show linear fits with $x = \log(\text{spot area})$. The three different colours are for the three inversion nodes, as shown in the plot legend.



(a) Inclination of the magnetic field



(b) Temperature

Figure 7.7.: (a) Inclination and (b) Temperature, averaged along the outer penumbra boundary (0.9 of the normalised Intensity) vs the area of the sunspot. The error bars are the standard deviation of the values along the boundary. The lines show linear fits with $x = \log(\text{spot area})$. The three different colours are for the three inversion nodes, as shown in the plot legend.

in figure 7.6b. Actually, looking at the figure more carefully, it becomes clear that at the solar surface, the vertical component of the field is close to zero for all spots with areas larger than 100 Mm^2 . The inclination starts from 60° and increases towards 90° at the lower-most node. A similar increase is shown at the other two nodes, only that the inclination values are a bit lower, as seen in figure 7.7a. The average inclination at the bottom node is roughly 90° for spots with areas larger than 100 Mm^2 .

The temperature at the outer penumbral boundary is essentially independent of the sunspot area (figure 7.7b). This result is not too surprising, given that the outer boundary was chosen based on the continuum intensity. It does nonetheless tell us that the temperature gradient at the outer boundary does not depend on sunspot size.

7.3.3. Physical Properties Across the Penumbra for Sunspots of Different Sizes

In this section, we derive radial profiles of various observables across the sunspots. We average the profiles over several spots of similar area in order to decrease the spot-to-spot scatter. Here, we distinguish between three bins in spot size (see Section 7.2). Figure 7.2 and Figure 7.3 show maps of the the mean intensity and of the magnetic field for typical spots in the three size categories.

Our results show that larger spots have a stronger magnetic field than smaller ones across the entire spot and at all optical depths (see Figure 7.8), in agreement with previous studies (e.g., Kopp and Rabin 1992, Livingston 2002, Rezaei et al. 2012, Schad 2014, Watson et al. 2014, Kiess et al. 2014, Rezaei et al. 2015). The value of the field decreases from the inner to the outer penumbral boundary for all nodes.

The vertical component of the magnetic field also remains larger for larger spots, figure 7.8, at around 0.7 of the normalised distance, it tends to become similar for spots of different sizes, and this behaviour is seen at all the inversion nodes. Nonetheless, the decrease of the field strength at the outer penumbral boundary from small to large spots seen in figure 7.6 is not reproduced here. This is because for some of the large spots, not the complete spot was inverted, so that the exact location of the penumbral boundary was not known. Consequently, the edge of the FOV was set as the outermost boundary of the spot, which artificially raised the field strength at the sunspot boundary for the largest spots. The same issue is also found for B_z .

This behaviour for the magnetic field strength and for B_z remains almost unchanged when we look separately along the major or the minor axis of the spot, as shown in figure 7.9 and figure 7.10, respectively. For the minor axis, the spots with the largest size tend to have slightly lower magnetic field strength and a significantly lower B_z across the penumbra. The actual reason for this discrepancy is unclear, one viable explanation is that in most large spots in the data set there was some kind of light bridge structure coming up along the shorter axis.

When looking at the radially averaged profiles, the inclination (in the local solar coor-

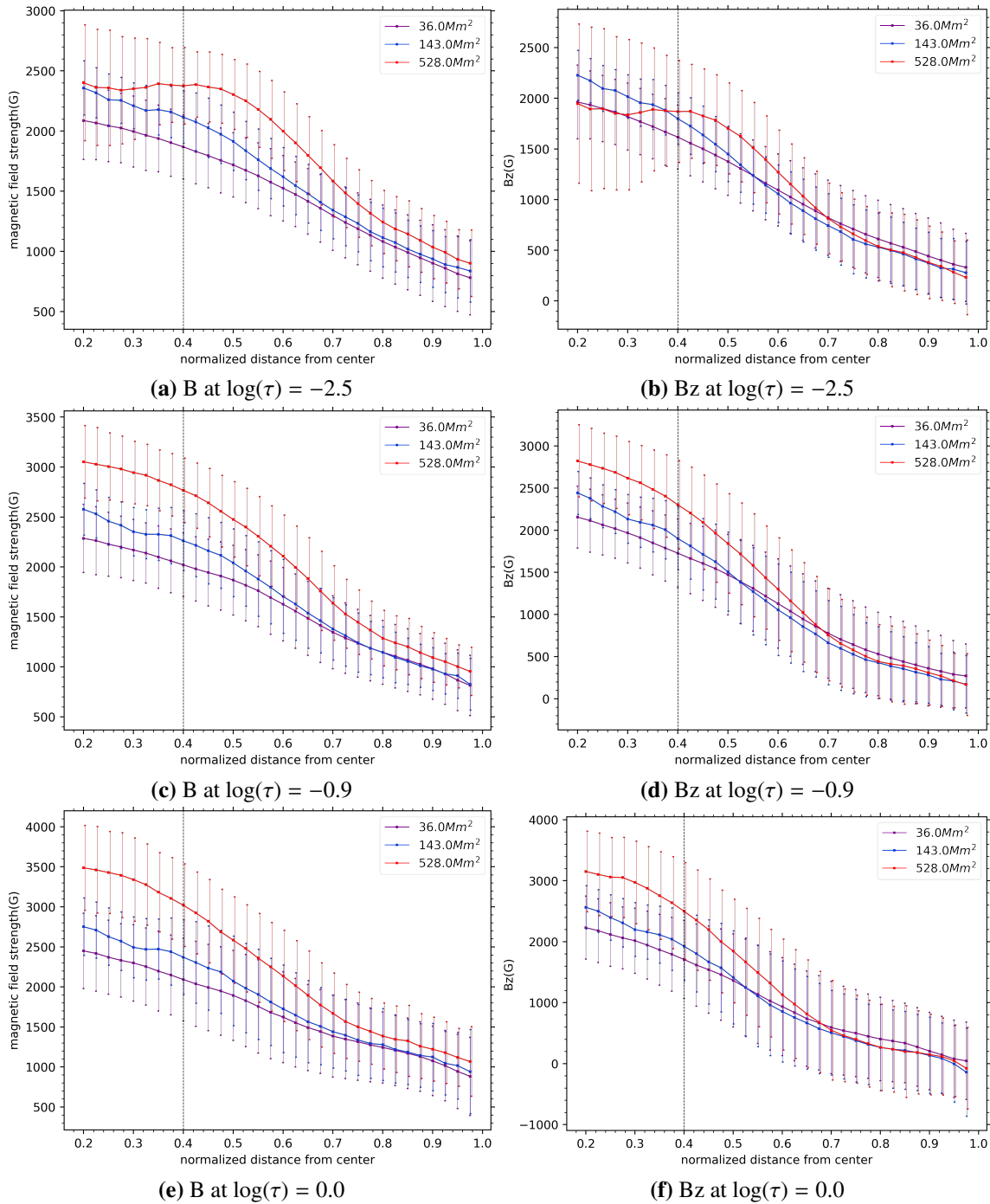


Figure 7.8.: Magnetic field strength {a,c,e} and the Vertical component of the magnetic field {b,d,f}, across the penumbra for the three nodes $\log(\tau) = -2.5, -0.9, 0.0$, respectively. The distance on the normalised scale is from the centre of the spot to the outer penumbra boundary. The error bars at each distance point are the standard deviation of the different spots from the mean.

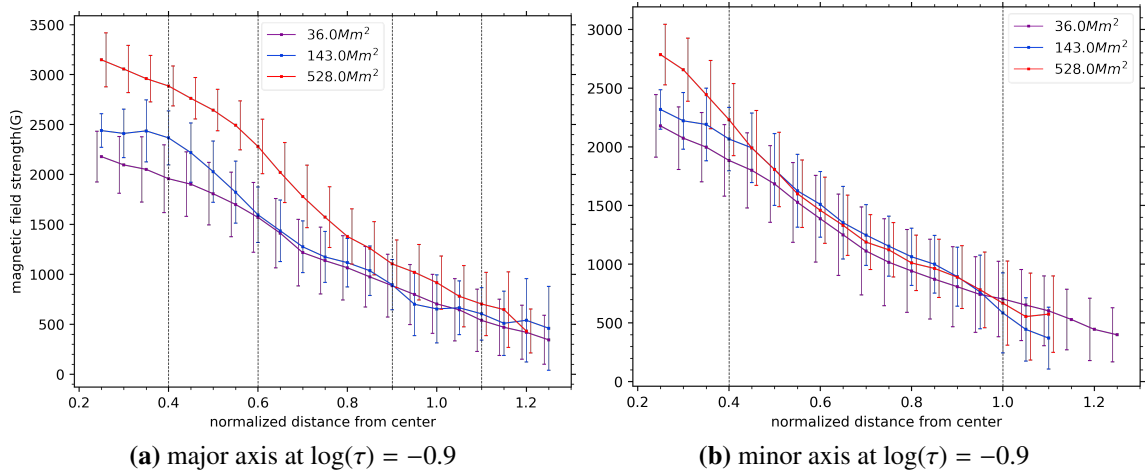


Figure 7.9.: Magnetic field strength across the penumbra for the central node $\log(\tau) = -0.9$, (a,b) along the major and minor axis respectively. The distance is normalised using the average distance of the outer penumbral boundary from the centre, separately for the major and minor axis. Thus the 1 on the x-axis represents the average outer penumbral boundary. The different colours of the profiles are for different sizes.

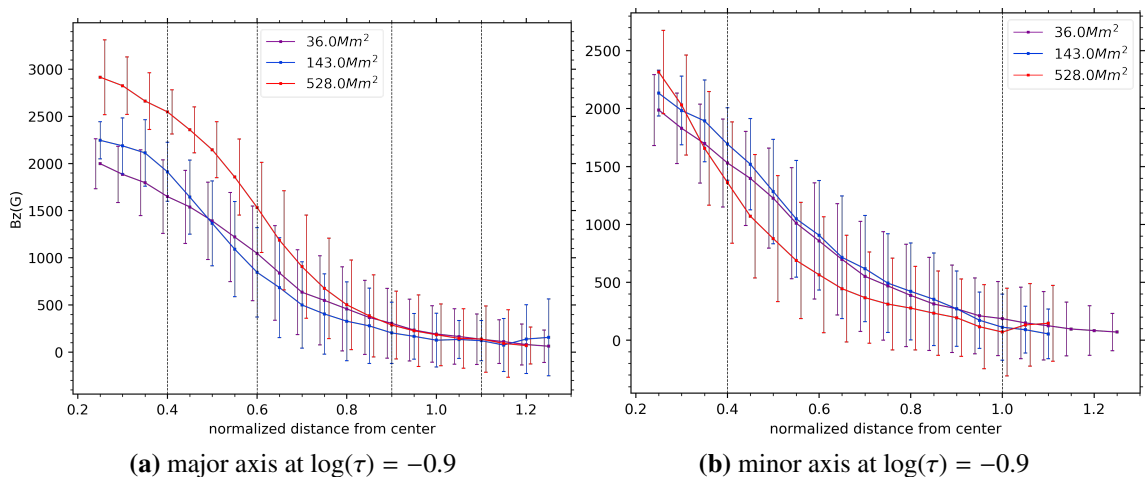


Figure 7.10.: The vertical component of the magnetic field strength across the penumbra for the central node $\log(\tau) = -0.9$, (a,b) along the major and minor axis, respectively. The normalisation of the distance is done separately for the major and minor axis (see Sect. 7.2), with 1 on the x-axis representing the average outer penumbral boundary along the long axis and the short axis. The different colours of the profiles are for sunspots with different areas (see plot legend).

dinates) of the magnetic field is slightly larger for larger spots in the penumbra (see left panels of figure 7.11). However, the inclination seems to vary significantly on large spatial scales across the sunspot, leading to strong differences between the azimuthal averages shown in figure 7.11 and the averages along the major or minor axis (see figure 7.12).

The azimuthally averaged temperature rises monotonically from the umbra to the outer penumbra (see figure 7.11). In the umbra and the inner penumbra, the temperature decreases with spot size (Brandt et al. 1992, Beck and Chapman 1993, Chapman et al.

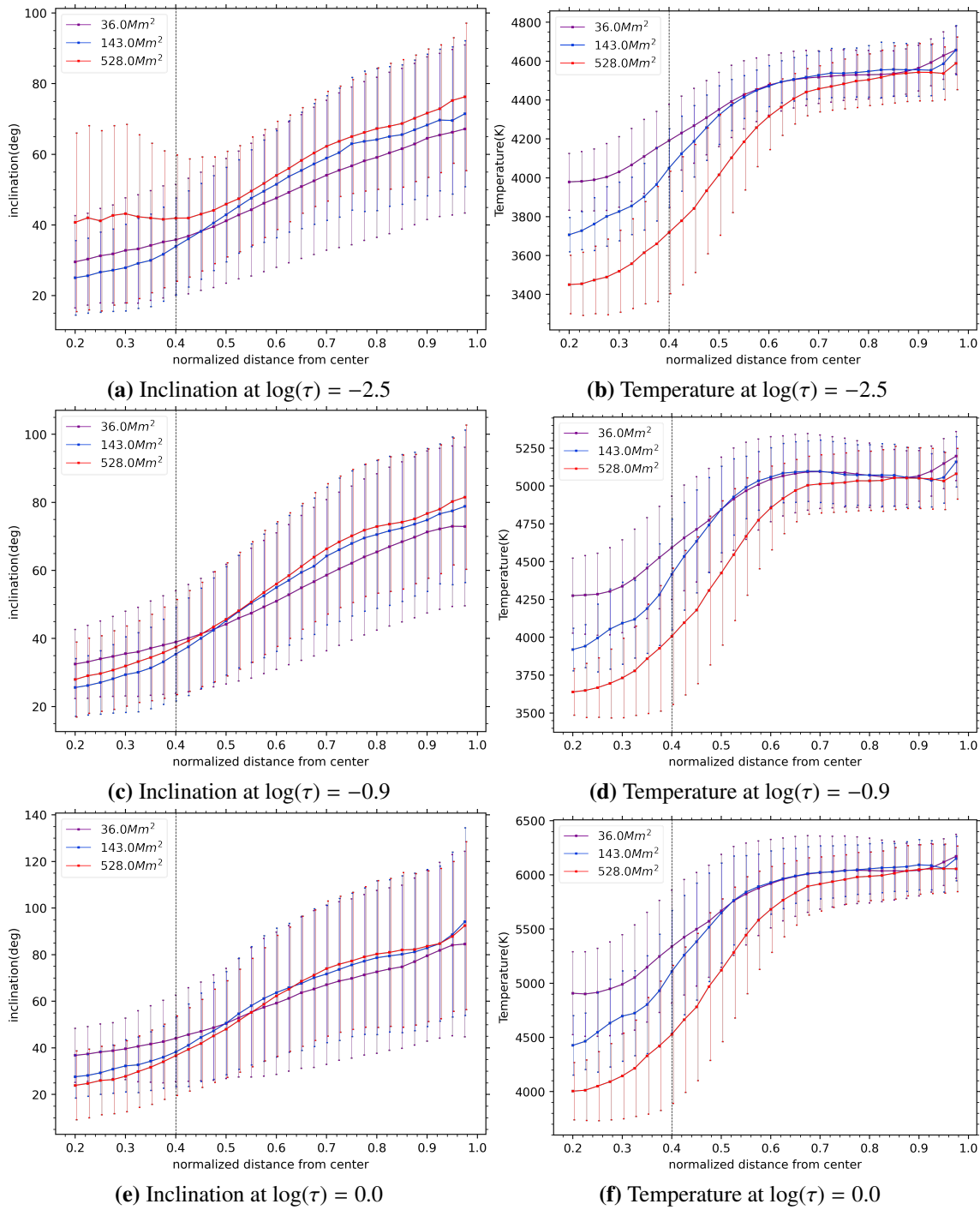


Figure 7.11.: Inclination of the magnetic field strength {a,c,e} and Temperature {b,d,f} across the penumbra for the three nodes $\log(\tau) = -2.5, -0.9, 0.0$, respectively. The distance on the normalised scale is from the centre of the spot to the outer penumbra boundary. The error bars at each distance point are the standard deviation of the different spots from the mean.

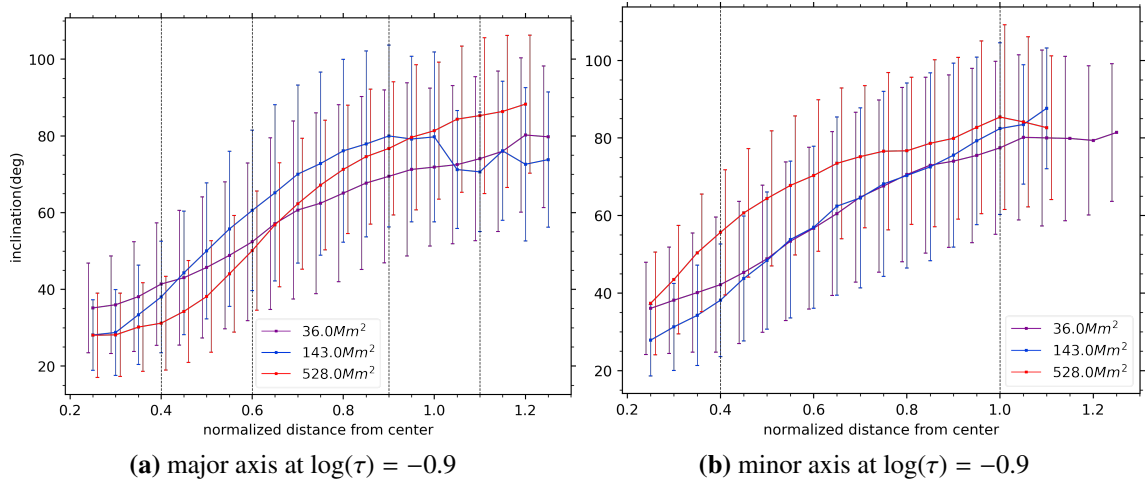


Figure 7.12.: The inclination of the magnetic field strength across the penumbra for the central node $\log(\tau) = -0.9$, (a,b) along the major and minor axis, respectively. The distance is normalised using the average distance of the outer penumbral boundary from the centre, separately for the major and minor axis. Thus the 1 on the x-axis represents the average outer penumbral boundary. The different colours of the profiles are for different sunspot areas.

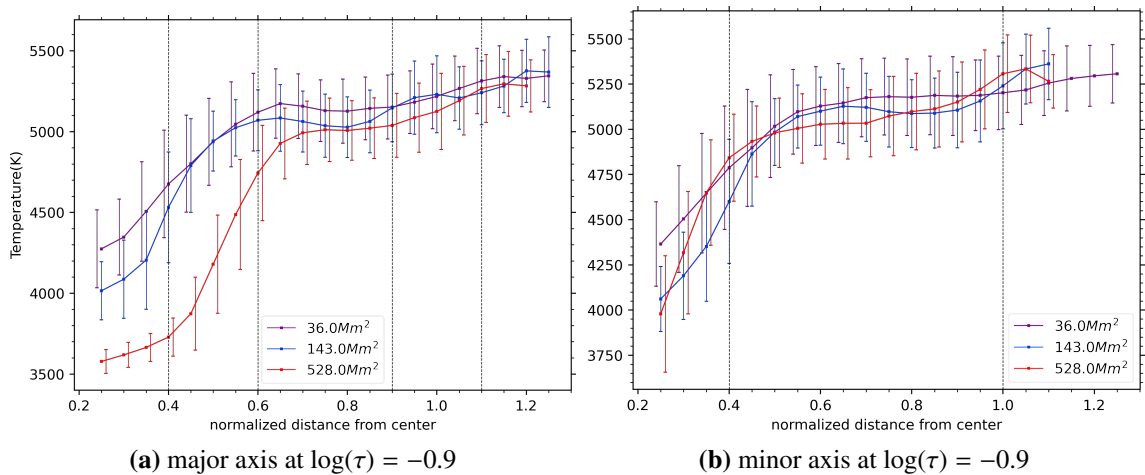


Figure 7.13.: Temperature across the penumbra for the central node $\log(\tau) = -0.9$, (a,b) along the major and minor axis, respectively. The distance is normalised using the average distance of the outer penumbral boundary from the centre, separately for the major and minor axis. Thus the 1 on the x-axis represents the average outer penumbral boundary. The different colours of the profiles are for different sunspot areas.

1994). In the outer penumbra, the temperature does not depend strongly on the size of the sunspots. As we look along the major axis, as in figure 7.13a, we see a huge difference between the temperature of the large spots (shown in red) and spots of other sizes, between the normalised distance of 0.4 to 0.6. While for the minor axis, no such difference is seen in figure 7.13b. This again suggests that the temperature varies on large spatial scales across the sunspots.

7.3.4. Flow Profile Across the Penumbra

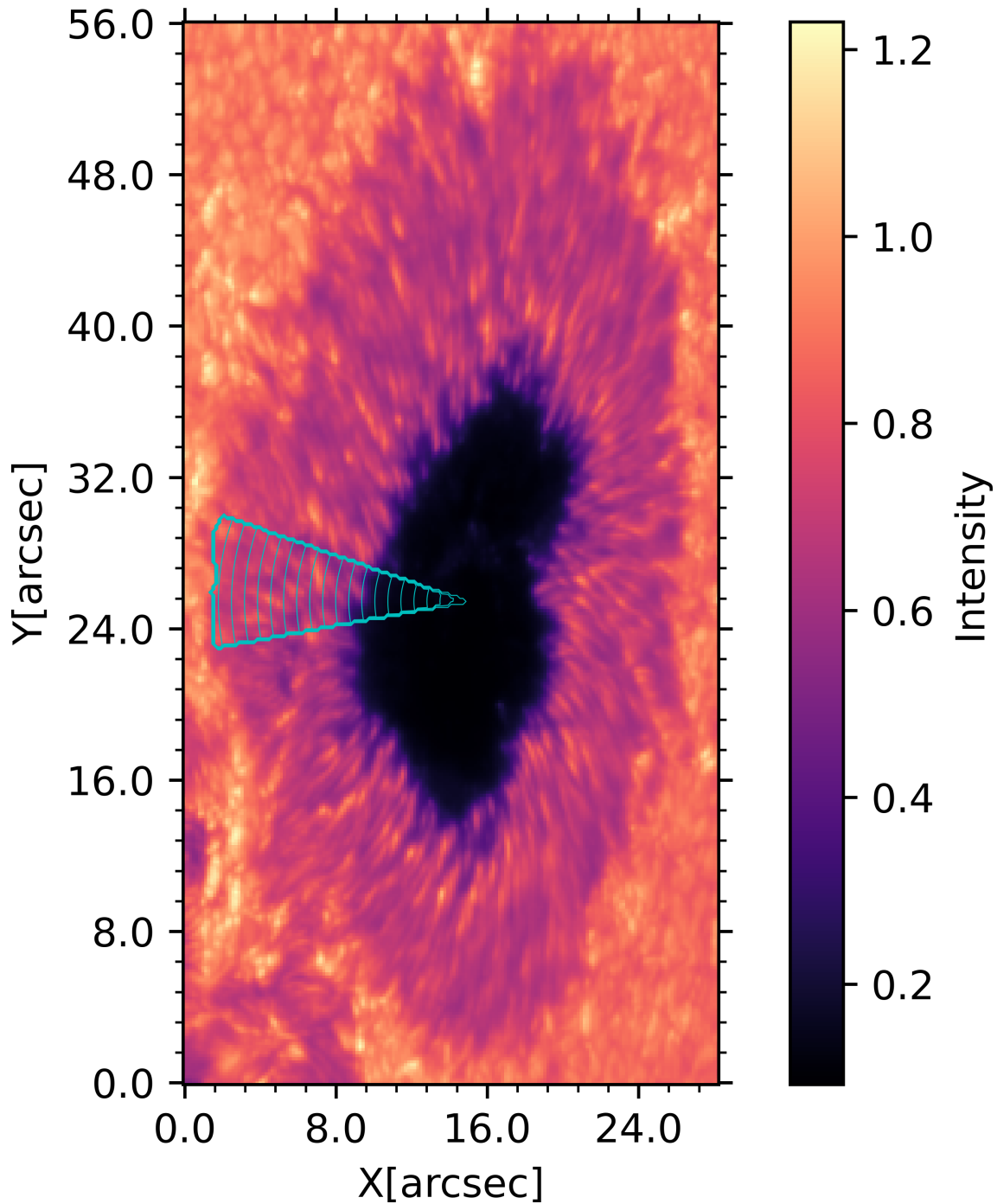


Figure 7.14.: Example image showing contours, and the region used for averaged plots.

In this section, we derive averaged profiles of the Evershed flow for spots of different sizes. Since the Evershed flow is mostly horizontal, we restrict the analysis to sunspots far away from disk center (heliocentric angle $\theta > 50^\circ$). We considered 7 sunspots, of which three have similar sizes. Hence, we averaged the results for these three spots. The averaging for the variation with distance plots was done along the contours as in the previous section, with a small modification, that only a small cone of 30° towards the

center of the disk was chosen (see Figure 7.14).

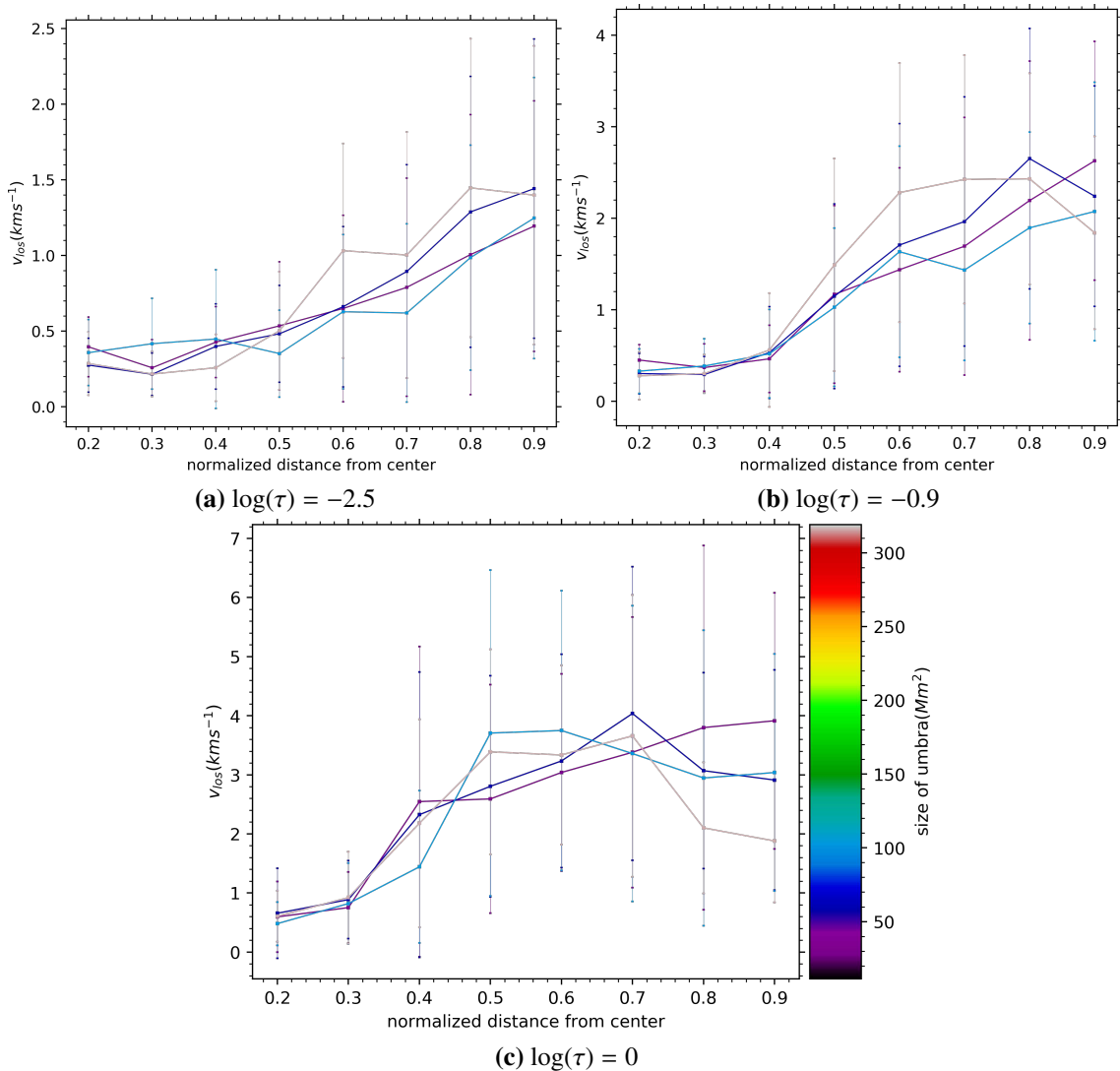


Figure 7.15.: Line of sight velocity with respect to distance from centre of the umbra, {a,b,c} at the nodes $\log(\tau) = -2.5, -0.9, 0.0$ respectively, for spots of different sizes. The colour legend gives the size of the umbra for the spots considered.

Figure 7.15, shows the resulting flow profiles at the three nodes, for spots of different sizes, as shown in the colour legend. For all the spots, the flow speed decreases rapidly from the deepest to the top node. The decrease in the LOS velocity at the lowest node in the outer parts of the penumbra shows an indication of downflows there (Westendorp Plaza et al. 1997). There is still a significant Evershed flow close to the outer boundary of the penumbra. In particular in the topmost node, the flow displays no indication of a saturation, indicating that in the upper layers the Evershed flow continues in the canopy (cf. Solanki et al. 1994). Interestingly, no clear difference is visible between spots of different sizes.

7.4. Discussion

We can confirm previous results that the azimuthally averaged B_z assumes a constant value at the UP boundary. Our result for the mean B_z (1820 G at $\log(\tau) = -0.9$) is in good agreement with the findings of Jurčák et al. (2018) (1867 G) and Lindner et al. (2020) (1787 G). We observe a dependence on optical depth, though. The mean B_z at the top node increases with spot size. This is because the magnetic field of the penumbral filaments is inclined, which means that it only reaches the upper photospheric layers slightly further outwards. Hence, when evaluating the mean B_z at $\log(\tau) = -2.5$, there is a stronger contribution from the umbra and from spines. These exhibit stronger magnetic fields in larger spots. For the same reason, the averaged temperature at the top node decreases with spot size. The umbrae of large spots are cooler. In the lower layers, the temperature increases with spot size, though. Here, the azimuthal averages are more affected by penumbral filaments. A possible explanation could be: In large spots, the penumbral filaments are cooler, and so, they contribute more to the azimuthal average. Since the penumbral filaments are much hotter than the surrounding spines, the mean temperature increases with spot size in the lower photosphere. Alternatively, it has to do with using a constant brightness threshold for separating the umbra from the penumbra. Due to the cooler filaments, the umbra-penumbra boundary is set deeper in the penumbra in larger spots. There the area covered by spines is lower than the area just next to the umbra. That could lead to a brighter penumbra. These explanations will have to be tested in future studies.

At the outer penumbral boundary, the averaged magnetic field decreases with spot area while the inclination increases. This is at odds with the results of Jurčák (2011), who found both quantities to increase with spot size. The reason for this discrepancy is currently unclear. Presumably, the averages of the observables depend on how exactly the outer boundary of the penumbra is defined. Depending on how the boundary is defined, surrounding granulation might falsely be assigned to the penumbra or parts of the penumbra could not be taken into account. For large spots, the mean B_z at the outer penumbral boundary becomes negative at $\log(\tau) = 1$. This is due to the polarity reversal in the tails of penumbral filaments (Tiwari et al. 2013).

As discussed above, the azimuthally averaged profiles of the vector magnetic field and of the temperature exhibit the expected dependencies on the spot size in the umbra and in the penumbra. However, there is no clear dependence of the radial profile on spot size in the outer penumbra. A possible explanation for this is that the outer penumbra is dominated by penumbral filaments, with no strong contribution from spines. Individual penumbral filaments look very similar, even between spots of different sizes (Tiwari et al. 2013, Löptien et al. 2021). We note that these azimuthal averages are probably strongly affected by the corrugation of layers of constant optical depth and by unresolved patches of opposite polarity (Joshi et al. 2017). In addition, there are strong differences between the azimuthally averaged profiles and the averages along the major or minor axes. This could indicate that the physical parameters in sunspots vary not only between penumbral filaments and spines but also on larger spatial scales in the azimuthal direction. However, to obtain clarity on this question, a larger set of sunspots will have to be considered, in particular taking care that there is no difference in the distribution over the solar disk

between spots of different sizes, as that can easily bias the results.

The Evershed flow does not exhibit any significant differences between spots of different sizes at all optical depths. This is probably again due to the uniform properties of penumbral filaments since the Evershed flow constitutes the flow along individual penumbral filaments. It is somewhat surprising, however, that the Evershed flow increases by the same amount over the same *relative* distance from the inner edge of the penumbra in spots of very different sizes. Since the penumbrae of larger spots are broader, this would imply that the gas is accelerated much more slowly over distance. However, these results need to be tested and confirmed with more spots, particularly with spots of different sizes located at the same distance from the disk centre. That would again avoid biases.

Summary

The thesis focuses on two main topics. (1) The characterisation and subsequent calibration of non-linearities of CMOS sensors to increase the polarimetric accuracy. (2) A study of penumbral properties of sunspots.

During the work on CMOS sensors, we realised how sensor non-linearities play an essential part in the data analysis for polarimetry and the importance of correcting these abnormalities, as seen in section 3.4.

We could confirm that the scene-dependent non-linear response of CMOS sensors is an actual effect that we can check for using a slanted edge target (see section 6.1.1). Furthermore, the scene dependence effect is different for the set of odd and even rows, which can be explained by the fact that a different set of electronics is dedicated to reading the two sets of rows. We tested three cameras using the slanted edge target and found that all three show a dependence of pixel count on the illumination scene for constant illumination of the test region. Only CAM3 had these abnormalities lying in the range of below 1% in the operation count regime, which was deemed sufficient for its use case (section 6.3).

Using a parallel bar target aligned along the columns, for a camera with a column parallel readout, see section 6.1.1.2, we checked for the effect of the position of the illumination in a row for the same row average and siblings. We found this effect to be an order less than the deviations in the pixel count due to its dependence on the row average and siblings, for CAM1. CAM2 showed a more pronounced directionality along the rows, which was seen as deviations in the shielded pixels due to sensor illumination, see section 6.2.

During the calibration process, we found that deductive targets do not allow us to cover the entire parameter space formed by the three relevant parameters for fitting (light level, row average and siblings, see section 5.1). The critical limitation of the deductive targets is that they do not allow a row average much higher than the test pixel value under homogeneous illumination, see section 5.2. Under the assumption of homogeneous illumination and all rows(odd and even separately) behaving similarly, we can still vary the row average and the allowed number of siblings independently for constant illumination, see section 5.2.4.

To overcome the shortcomings mentioned above, we designed a setup that can probe the thus formed parameter space for the individual parameters, see section 5.3. The setup uses three independent illumination sources to project different scenes onto the sensor. The calibration data acquired using the setup allowed us to correct the sensor non-linearities to a level required for solar polarimetry (deviations from a linear response below 1%, under all illumination scenes), as seen in section 6.1.2.2.

The setup still has some scope for improvements with the goal of gathering the data required to calibrate the entire sensor area, not just a region of interest, as done in this thesis. The desirable modifications include:

- cross-calibration of the three illumination sources, to allow for the calibration of the entire sensor.
- use of a narrow band light source for a better parallel bar target test, (see section 5.2.3).
- better thermal stability setup, as running the cameras in a thermally stable environment for a long time is important. This was a critical problem as many of the data runs had to be discarded due to a change in the operating temperature of the camera.
- improvements in the control software for the setup, leading towards a higher level of automation of the data acquisition.
- more flexible optical configuration that can be adjusted to different camera models.

Finally, the importance of the developed setup lies in the fact that even if we develop new sensors (for scientific use cases) which do not have pixel cross-talk, we would need this setup to check for the level of the scene-dependent effects. Furthermore, we would still need to calibrate them.

Moving onto the second project, we looked at the general properties of simple sunspots, focusing on the penumbra. We used the inverted polarimetric data from the spectropolarimeter (SP) onboard the Hinode spacecraft to study the height-dependent physical properties of sunspots. The spot segmentation into umbra and penumbra was done using an intensity threshold of $0.5 I_c$ for the umbra and $0.9 I_c$ for the penumbra, see chapter 7. In order to look at the radial dependence of the physical quantities, we defined distance contours from the centre of the spot to its outer boundary and took the azimuthal average of the physical quantities along these contours.

It has been claimed that the umbra-penumbra boundary occurs at a fixed threshold of the vertical magnetic field, independent of the size of the sunspot. We found that the magnetic field strength at the umbra boundary increases with the umbral area and decreases with the height. At the same time, the slope of the magnetic field with the umbral area increases with the height. The vertical component of the magnetic field remains almost constant with the umbral area at the central node of inversion, while it shows an increase with the umbral area at the top most node. This is explained in terms of the increased contribution from the umbra for larger spots. The inclination increases with the umbral area, indicating that smaller spots have more vertical fields, and the field is more vertical at the lower nodes. The temperature increases with the umbral area at the bottom node but not in the higher atmospheric layers. Hence, the averaged observables at the umbra-penumbra boundary show no consistent dependence on the spot size at the different optical depths. This must be considered for models describing the transition from the umbra to the penumbra.

At the outer penumbra boundary, the vertical component of the magnetic field decreases with the spot size, while the inclination shows an increase with the size. The lowermost node has the highest inclination, meaning it is more horizontal than the top nodes. The temperature decreases with the height of inversion but remains almost constant with the spot size.

The magnetic field strength and the vertical component of the magnetic field consistently decrease radially for spots of all sizes and at all inversion nodes, while the magnetic field inclination and the temperature increase radially for all spots. The azimuthally averaged radial profiles for the magnetic field strength and temperature show the expected dependence on the umbral area in the inner penumbra, larger spots having a higher magnetic field, and lower temperature. The radial temperature profiles show a steep increase near the umbra-penumbra boundary, become almost constant in the middle penumbra, and increase near the spot boundary. Interestingly, there is almost no dependence of the observables on spot size in the outer penumbra.

We did not see a significant difference in the Evershed flow with the size of the spot. This is explained as a result of the uniform properties of the penumbral filaments. We were able to confirm downflows at the lowermost inversion node at the outer penumbral boundary.

The next step would be to do the same study with a larger number of sunspots. Here, one should compare spots located at a similar position on the disk to reduce the influence of centre-to-limb effects. This is particularly important for the Evershed flow, which depends strongly on the viewing angle.

A Data Storage Requirements

Here we show some typical calculations for the data storage limits that we might run into while storing this data.

- Image size $n \times m$
- Number of bits used for data, storing pixel value, q bits
- Moreover, let us say we take $2k$ images for each light level.

The size of one image is $n \times m \times q$ bits without compression. For $2k \times 2k$, 10 bit images, the total storage space required for $2k$ images would be ~ 75 Gbits or ~ 10 GB.

For histogramming the same data, we need to stack the 2000 images to make an array of pixel histograms, each containing the information about the distribution of counts across the images for the pixel. Let us say the standard deviation of the values in the pixel for one light level be p bits, this is the number of bins required for the per-pixel histogram. We can safely use a 16-bit integer to handle the number of images used for histogramming. Even in the unlikely case of a pixel having just a constant digital value across all these 2000 frames, we would still be able to store this number.

With $p = 100$ (which is an overestimation), for $2k$ images of $2k \times 2k$, we can get away with $2k \times 2k \times 100 \times 16$ bits ~ 6 Gbits or ~ 0.75 GB.

The critical point is that this number would remain constant, even for an increasing number of images being taken per light level, unless we run out of those 16-bits.

In the simple case of the light level being the only parameter for calibration, this histogram can store all the required data. We would require such histograms for each light level and sample that parameter space as densely as possible. Let us say we have a 10-bit sensor, representing the allowable range of digital values. Furthermore we sample the light level space using 50 points. The data storage requirements are,

- Raw image data = $10\text{GB} \times 50 = 500$ GB
- Histogram = $0.75\text{GB} \times 50 = 37.5$ GB

One of the disadvantage of histogramming is that any information about frame to frame variation with respect to time is lost.

However once made, we can easily do any kind of statistical analysis on the data. At least in the simple case of studying just the light level dependence, the whole data set can be loaded at ones to the RAM, for visualising it. In conjugation with frame averaged time profiles, histogramming allows for long term storage of the data, allowing for different fitting techniques as the need arises. More details on how to make histograms or computational techniques can be found in *Numerical Recipes: The Art of Scientific Computing* (Press et al. 2007).

B Controls and Experiment Time Requirements

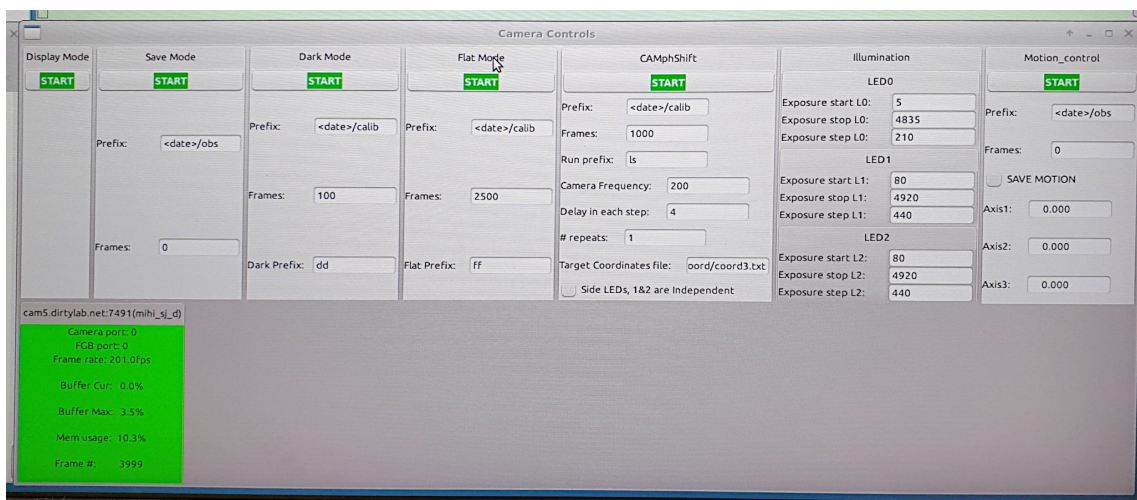


Figure B.1.: Main control panel for the Calibration setup

The main control system was designed and made by Dr. Michiel van Noort. Only the CAMphshift and Illumination panels and some parts of Motion control were added by me, on the structure already established. The contents of the two main blocks of our interest are,

CAMphshift

Prefix for directory structure to save data.

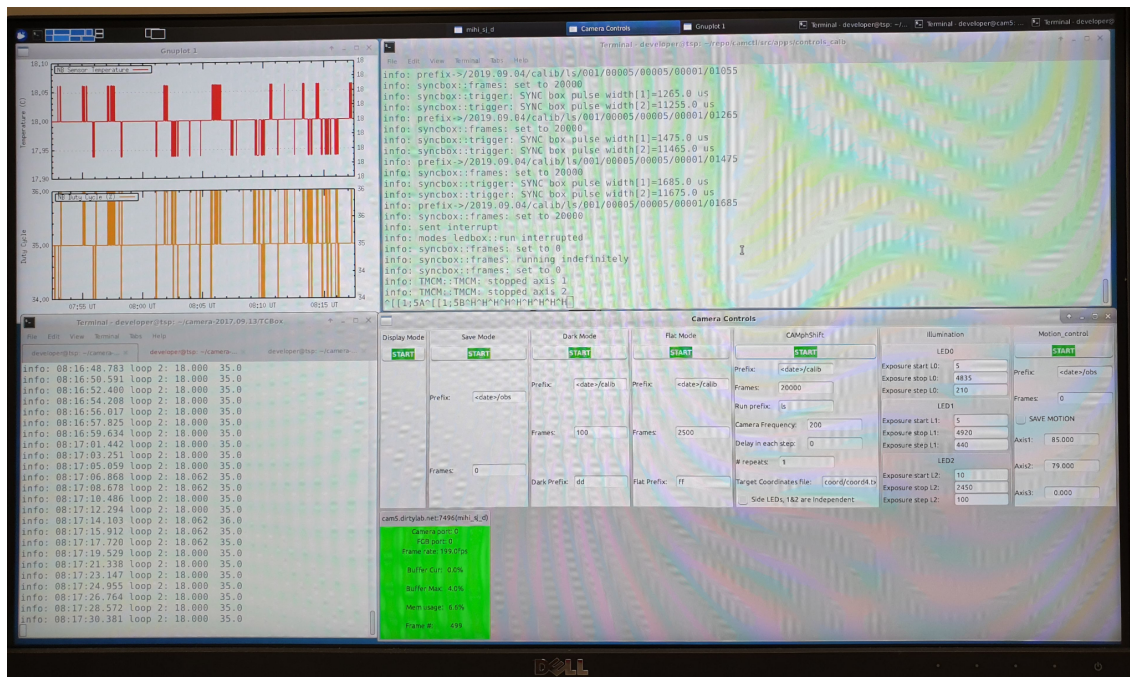
Frames number of frames to take for each light level.

Camera Frequency desired frame rate of the camera.

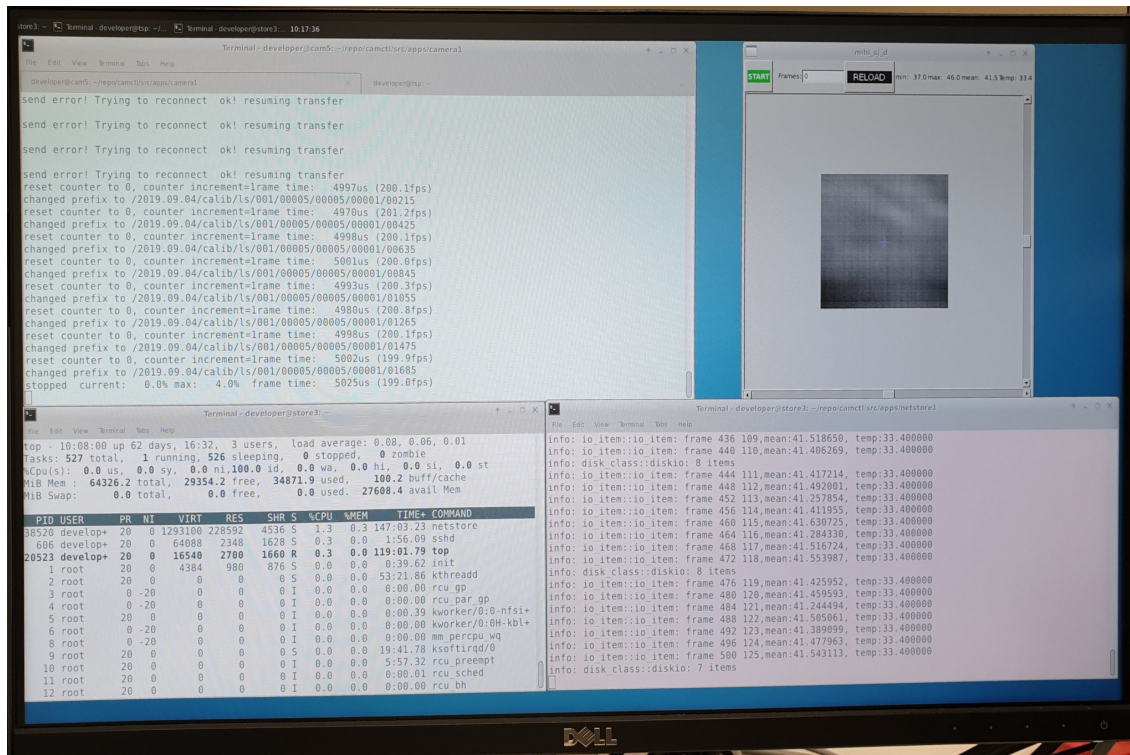
Delay time to wait before we start to take frames for a different state or light level.

Repeat number of times to repeat the whole measurement routine.

Target Coordinate File file to load the positions of the movable spheres.



(a) Panel 1



(b) Panel 2

Figure B.2.: Panel showing the setup running. Top left corner showing the temperature of the camera, and the sub-image in the bottom panel showing the preview. All other panels are for keeping track of all the setup elements, and their working condition.

Side LEDs independent check to independently vary both LEDs, across the values listed in Illumination panel. By default, the values for LED1 are taken for LED2 as well, and both work in sync, see figure 5.12 on page 42.

Illumination Panel

LED0 illumination levels, in terms of phase shift for the calibration region.

LED1 illumination levels, in terms of phase shift for control region 1.

LED2 illumination levels, in terms of phase shift for control region 2, as shown in figure 6.7.

Motion control

Axis position of each Integrating sphere, only the first two axes are used, for the two spheres. Mainly for moving the integrating spheres during trial and error. During the automatic phase of the setup the integrtaing sphere position are taken from the target coordinate file, which also locks the default positions of the spheres so that they do not accidentally collide during the experiment.

Once a start is pressed in a panel, all the other panels become inactive till a stop is pressed. The setup runs through all the vales for LED1 for one value of LED0. This is repeated for all specified values of LED0 for one target configurations. And as the outer most loop all the target configurations are covered. Pressing a stop just stops the writing of the data to the disk, or its processing, the camera keeps on running at the specified frame rate, and it is critical to do that for thermal stability.

Time required for one calibration run

Lets say the camera is running at 200 Hz and the number of actual frames taken per illumination scene is 10000, then the time required to take these frames is 50 *seconds*. Adding a waiting time of 2 *minutes* due to the time needed for saving histograms, the actual time needed for accumulation of data per illumination scene is 3 *minutes* on average.

If do a test for 10 illumination levels in the calibration region, and 10 illumination levels in the control region of the sensor, with 10 differnt positions of the integrating spheres. The total number of illuminations scenes projected onto the sensor is $10 \times 10 \times 10 \times = 1000$, which means that we need $1000 \times 3 \text{ minutes} = 50 \text{ hours}$ or 2 *days* for the entire test. We certainly need more data points (approximately 10 times more) for each parameter for a better sampling of the parameter space, which means that the time required for the test will be still longer.

C Sunspots

List of selected spots for Umbral area dependence				
NOAA	Observation Date	Distance from disk center [°]	Spot area [Mm ²]	Umbral area [Mm ²]
10921	2006.11.05	22	170.30	37.55
10923	2006.11.11	34	1144.86	345.83
10923	2006.11.12	31	1596.69	393.89
10923	2006.11.13	15	1965.40	473.98
10923	2006.11.14	8	1976.74	499.88
10923	2006.11.15	13	2080.69	511.00
10923	2006.11.16	30	1794.45	421.93
10926	2006.12.03	24	88.84	11.71
10933	2007.01.06	9	630.07	129.76
10933	2007.01.07	24	515.27	115.10
10933	2007.01.08	30	388.25	108.26
10940	2007.01.31	20	459.31	138.85
10944	2007.02.28	2	218.69	49.78
10944	2007.03.01	11	148.60	49.28
10944	2007.03.02	16	142.98	46.59
10953	2007.05.02	12	880.77	172.90
10953	2007.05.03	24	617.67	130.16
10953	2007.05.04	37	586.67	96.61
10956	2007.05.18	15	38.48	0.88
10956	2007.05.19	4	10.45	1.88
10956	2007.05.20	12	70.92	12.35
10960	2007.06.10	34	88.68	28.89
10978	2007.12.13	17	8.40	1.06
11039	2009.12.28	34	18.76	0.42
11039	2010.01.01	29	26.33	8.60
11039	2010.01.01	29	25.77	2.26
11041	2010.01.26	20	67.17	15.14
11106	2010.09.16	27	114.17	23.23
11117	2010.10.27	25	22.05	2.19
11117	2010.10.28	35	74.74	18.20
11360	2011.11.28	21	56.66	12.00
11361	2011.11.30	18	73.89	18.62
11361	2011.12.03	34	68.71	22.12
11419	2012.02.18	37	42.55	5.32
11536	2012.07.31	34	36.06	13.49
11560	2012.09.01	9	28.46	2.23
11560	2012.09.03	22	29.23	1.26

Table C.1.: The table lists the spots used in our study.

Bibliography

- H. Balthasar and W. Schmidt. Polarimetry and spectroscopy of a simple sunspot. 2: On the height and temperature dependence of the magnetic field. *Astronomy & Astrophysics*, 279(1):243–250, Nov. 1993.
- P. Barthol, A. Gandorfer, S. K. Solanki, M. Schüssler, B. Chares, W. Curdt, W. Deutsch, A. Feller, D. Germerott, B. Grauf, K. Heerlein, J. Hirzberger, M. Kolleck, R. Meller, R. Müller, T. L. Riethmüller, G. Tomasch, M. Knölker, B. W. Lites, G. Card, D. Elmore, J. Fox, A. Lecinski, P. Nelson, R. Summers, A. Watt, V. Martínez Pillet, J. A. Bonet, W. Schmidt, T. Berkefeld, A. M. Title, V. Domingo, J. L. Gasent Blesa, J. C. Del Toro Iniesta, A. López Jiménez, A. Álvarez-Herrero, L. Sabau-Graziati, C. Widani, P. Haberler, K. Härtel, D. Kampf, T. Levin, I. Pérez Grande, A. Sanz-Andrés, and E. Schmidt. The Sunrise Mission. *Solar Physics*, 268(1):1–34, Jan. 2011. doi: 10.1007/s11207-010-9662-9.
- J. G. Beck and G. A. Chapman. A study of the contrast of sunspots from photometric images. *Solar Physics*, 146:49–60, July 1993. doi: 10.1007/BF00662169.
- B. P. Beecken and E. R. Fossum. Determination of the conversion gain and the accuracy of its measurement for detector elements and arrays. *Appl. Opt.*, 35(19):3471–3477, Jul 1996. doi: 10.1364/AO.35.003471. URL <http://opg.optica.org/ao/abstract.cfm?URI=ao-35-19-3471>.
- N. Bello González, O. V. Okunev, I. Domínguez Cerdeña, F. Kneer, and K. G. Puschmann. Polarimetry of sunspot penumbrae with high spatial resolution. *Astronomy & Astrophysics*, 434(1):317–327, Apr. 2005. doi: 10.1051/0004-6361:20042001.
- L. R. Bellot Rubio, H. Balthasar, M. Collados, and R. Schlichenmaier. Field-aligned overshed flows in the photosphere of a sunspot penumbra. *A&A*, 403(3):L47–L50, 2003. doi: 10.1051/0004-6361:20030576. URL <https://doi.org/10.1051/0004-6361:20030576>.
- L. R. Bellot Rubio, H. Balthasar, and M. Collados. Two magnetic components in sunspot penumbrae. *Astronomy & Astrophysics*, 427:319–334, Nov. 2004. doi: 10.1051/0004-6361:20041277.
- L. R. Bellot Rubio, K. Langhans, and R. Schlichenmaier. Multi-line spectroscopy of dark-cored penumbral filaments. *Astronomy & Astrophysics*, 443(1):L7–L10, Nov. 2005. doi: 10.1051/0004-6361:200500179.
- L. R. Bellot Rubio, S. Tsuneta, K. Ichimoto, Y. Katsukawa, B. W. Lites, S. Nagata, T. Shimizu, R. A. Shine, Y. Suematsu, T. D. Tarbell, A. M. Title, and J. C. del Toro Iniesta. Vector Spectropolarimetry of Dark-cored Penumbral Filaments with Hinode. *Astrophysical Journal Letters*, 668(1):L91–L94, Oct. 2007. doi: 10.1086/522604.

- M. Benko, S. J. González Manrique, H. Balthasar, P. Gömöry, C. Kuckein, and J. Jurcák. Properties of the inner penumbral boundary and temporal evolution of a decaying sunspot. *A&A*, 620:A191, 2018. doi: 10.1051/0004-6361/201834296. URL <https://doi.org/10.1051/0004-6361/201834296>.
- N. Bezawada, D. Ives, and D. Atkinson. Conversion gain non-linearity and its correction in hybridised near infrared detectors. *Proceedings of SPIE - The International Society for Optical Engineering*, 6690, 09 2007. doi: 10.1117/12.732454.
- L. Bharti, B. Beeck, and M. Schüssler. Properties of simulated sunspot umbral dots. *Astronomy & Astrophysics*, 510:A12, Jan. 2010a. doi: 10.1051/0004-6361/200913328.
- L. Bharti, S. K. Solanki, and J. Hirzberger. Evidence for Convection in Sunspot Penumbrae. *Astrophysical Journal Letters*, 722(2):L194–L198, Oct. 2010b. doi: 10.1088/2041-8205/722/2/L194.
- T. J. Bogdan, P. A. Gilman, I. Lerche, and R. Howard. Distribution of Sunspot Umbral Areas: 1917–1982. *Astrophysical Journal*, 327:451, Apr. 1988. doi: 10.1086/166206.
- S. E. Bohndiek, A. Blue, A. T. Clark, M. L. Prydderch, R. Turchetta, G. J. Royle, and R. D. Speller. Comparison of methods for estimating the conversion gain of cmos active pixel sensors. *IEEE Sensors Journal*, 8(10):1734–1744, 2008. doi: 10.1109/JSEN.2008.2004296.
- K. Boone, G. Aldering, Y. Copin, S. Dixon, R. S. Domagalski, E. Gangler, E. Pecontal, and S. Perlmutter. A binary offset effect in CCD readout and its impact on astronomical data. *Publications of the Astronomical Society of the Pacific*, 130(988):064504, may 2018. doi: 10.1088/1538-3873/aab0fe. URL <https://doi.org/10.1088/1538-3873/aab0fe>.
- M. Born and E. Wolf. *Principles of Optics: 60th Anniversary Edition*. Cambridge University Press, 7 edition, 2019. doi: 10.1017/9781108769914.
- J. M. Borrero and K. Ichimoto. Magnetic Structure of Sunspots. *Living Reviews in Solar Physics*, 8(1):4, Sept. 2011. doi: 10.12942/lrsp-2011-4.
- J. M. Borrero, S. K. Solanki, L. R. Bellot Rubio, A. Lagg, and S. K. Mathew. On the fine structure of sunspot penumbrae. I. A quantitative comparison of two semiempirical models with implications for the Evershed effect. *Astronomy & Astrophysics*, 422: 1093–1104, Aug. 2004. doi: 10.1051/0004-6361:20041001.
- J. M. Borrero, A. Lagg, S. K. Solanki, and M. Collados. On the fine structure of sunspot penumbrae. II. The nature of the Evershed flow. *Astronomy & Astrophysics*, 436(1): 333–345, June 2005. doi: 10.1051/0004-6361:20042553.
- P. N. Brandt, W. Schmidt, and M. Steinegger. Photometry of Sunspots Observed at Tenerife. In R. F. Donnelly, editor, *Solar Electromagnetic Radiation Study for Solar Cycle 22*, page 130, July 1992.

- B. E. Burke, J. A. Gregory, M. Cooper, A. Loomis, D. Young, T. A. Lind, P. C. Doherty, P. J. Daniels, D. J. Landers, J. S. Ciampi, K. F. Johnson, and P. O'Brien. Ccd imager development for astronomy. 2007.
- G. A. Chapman, A. M. Cookson, and J. J. Dobias. Observations of changes in the bolometric contrast of sunspots. *Astrophysical Journal*, 432:403–408, Sept. 1994. doi: 10.1086/174578.
- A. R. Choudhuri. The Dynamics of Magnetically Trapped Fluids. I. Implications for Umbral Dots and Penumbral Grains. *Astrophysical Journal*, 302:809, Mar. 1986. doi: 10.1086/164042.
- R. E. Danielson. The Structure of Sunspot Umbras. I. Observations. *Astrophysical Journal*, 139:45, Jan. 1964. doi: 10.1086/147738.
- J. C. del Toro Iniesta. *Introduction to Spectropolarimetry*. Cambridge University Press, 2003. doi: 10.1017/CBO9780511536250.
- J. C. del Toro Iniesta, L. R. Bellot Rubio, and M. Collados. Cold, Supersonic Evershed Downflows in a Sunspot. *Astrophysical Journal Letters*, 549(1):L139–L142, Mar. 2001. doi: 10.1086/319137.
- C. Dominguez-Tagle, M. Collados, R. Lopez, J. J. Vaz Cedillo, M. A. Esteves, O. Grassin, N. Vega, A. Mato, J. Quintero, H. Rodriguez, S. Regalado, and F. Gonzalez. First light of the Integral Field Unit of GRIS on the GREGOR solar telescope. *arXiv e-prints*, art. arXiv:2206.14294, June 2022.
- J. Evershed. Radial movement in sun-spots. *Monthly Notices of the RAS*, 69:454, Mar. 1909. doi: 10.1093/mnras/69.5.454.
- A. Feller, A. Gandorfer, F. A. Iglesias, A. Lagg, T. L. Riethmüller, S. K. Solanki, Y. Katsukawa, and M. Kubo. The SUNRISE UV Spectropolarimeter and imager for SUNRISE III. In *Society of Photo-Optical Instrumentation Engineers (SPIE) Conference Series*, volume 11447 of *Society of Photo-Optical Instrumentation Engineers (SPIE) Conference Series*, page 11447AK, Dec. 2020. doi: 10.1117/12.2562666.
- E. Fossum. Cmos image sensors: electronic camera-on-a-chip. *IEEE Transactions on Electron Devices*, 44(10):1689–1698, 1997. doi: 10.1109/16.628824.
- A. I. Francisco and A. J. Feller. Instrumentation for solar spectropolarimetry: state of the art and prospects. *Optical Engineering*, 58(8):1 – 21, 2019. doi: 10.1117/1.OE.58.8.082417. URL <https://doi.org/10.1117/1.OE.58.8.082417>.
- C. Frutiger, S. K. Solanki, M. Fligge, and J. H. M. J. Bruls. Properties of the solar granulation obtained from the inversion of low spatial resolution spectra. *A&A*, 358: 1109–1121, June 2000.
- A. Gamal and H. Eltoukhy. Cmos image sensors. *IEEE Circuits and Devices Magazine*, 21:6–20, 2005.

- A. Gamal, B. A. Fowler, H. Min, and X. Liu. Modeling and estimation of FPN components in CMOS image sensors. In M. M. Blouke, editor, *Solid State Sensor Arrays: Development and Applications II*, volume 3301, pages 168 – 177. International Society for Optics and Photonics, SPIE, 1998. doi: 10.1117/12.304560. URL <https://doi.org/10.1117/12.304560>.
- A. Gandorfer, B. Grauf, P. Barthol, T. L. Riethmüller, S. K. Solanki, B. Chares, W. Deutsch, S. Ebert, A. Feller, D. Germerott, K. Heerlein, J. Heinrichs, D. Hirche, J. Hirzberger, M. Kolleck, R. Meller, R. Müller, R. Schäfer, G. Tomasch, M. Knölker, V. Martínez Pillet, J. A. Bonet, W. Schmidt, T. Berkefeld, B. Feger, F. Heidecke, D. Soltau, A. Tischenberg, A. Fischer, A. Title, H. Anwand, and E. Schmidt. The Filter Imager SuFI and the Image Stabilization and Light Distribution System ISLiD of the Sunrise Balloon-Borne Observatory: Instrument Description. *Solar Physics*, 268(1):35–55, Jan. 2011. doi: 10.1007/s11207-010-9636-y.
- M. K. Georgoulis. A New Technique for a Routine Azimuth Disambiguation of Solar Vector Magnetograms. *The Astrophysical Journal Letters*, 629(1):L69–L72, Aug. 2005. doi: 10.1086/444376.
- J. Herrmann, W. Pomrehn, M. Verhoeven, J. Leconte, M. Wány, F. Dierks, and A. Theuwissen. Standard for characterization and presentation of specification data for image sensors and cameras. 07 2022.
- T. Hewagama, D. Deming, D. E. Jennings, V. Osherovich, G. Wiedemann, D. Zipoy, D. L. Mickey, and H. Garcia. Solar Magnetic Field Studies Using the 12 Micron Emission Lines. II. Stokes Profiles and Vector Field Samples in Sunspots. *Astrophysical Journal Suppl. Ser.*, 86:313, May 1993. doi: 10.1086/191781.
- I. Hwang, D. Kim, and M. Song. Design of a cmos image sensor based on a 10-bit two-step single-slope adc. *Journal of the Institute of Electronics and Information Engineers*, 50, 11 2013. doi: 10.5573/ieek.2013.50.11.064.
- Y. Hwang, S. Lee, and M. Song. Design of a cmos image sensor with a 10-bit two-step single-slope a/d converter and a hybrid correlated double sampling. In *2014 10th Conference on Ph.D. Research in Microelectronics and Electronics (PRIME)*, pages 1–4, 2014. doi: 10.1109/PRIME.2014.6872708.
- J. Janesick and M. Blouke. Scientific charge-coupled devices: past, present, and future. *Optics and Photonics News*, 6:16–20, 04 1995. doi: 10.1364/OPN.6.4.000016.
- J. Joshi, A. Lagg, J. Hirzberger, S. K. Solanki, and S. K. Tiwari. Vertical magnetic field gradient in the photospheric layers of sunspots. *A&A*, 599:A35, 2017. doi: 10.1051/0004-6361/201527060. URL <https://doi.org/10.1051/0004-6361/201527060>.
- J. Jurčák. Azimuthal variations of magnetic field strength and inclination on penumbral boundaries. *Astronomy & Astrophysics*, 531:A118, July 2011. doi: 10.1051/0004-6361/201015959.

- J. Jurčák, N. Bello González, R. Schlichenmaier, and R. Rezaei. A distinct magnetic property of the inner penumbral boundary - formation of a stable umbra-penumbra boundary in a sunspot. *A&A*, 580:L1, 2015. doi: 10.1051/0004-6361/201425501. URL <https://doi.org/10.1051/0004-6361/201425501>.
- J. Jurčák, R. Rezaei, N. Bello González, R. Schlichenmaier, and J. Vomlel. The magnetic nature of umbra-penumbra boundary in sunspots. *A&A*, 611:L4, 2018. doi: 10.1051/0004-6361/201732528. URL <https://doi.org/10.1051/0004-6361/201732528>.
- J. Jurčák, M. Schmassmann, M. Rempel, N. Bello González, and R. Schlichenmaier. A distinct magnetic property of the inner penumbral boundary. III. Analysis of simulated sunspots. *Astronomy & Astrophysics*, 638:A28, June 2020. doi: 10.1051/0004-6361/202037852.
- C. U. Keller. Recent Progress in Imaging Polarimetry. *Solar Physics*, 164(1-2):243–252, Mar. 1996. doi: 10.1007/BF00146637.
- R. Keppens and V. Martinez Pillet. The magnetic structure of pores and sunspots derived from Advanced Stokes Polarimeter data. *Astronomy & Astrophysics*, 316:229–242, Dec. 1996.
- C. Kiess, R. Rezaei, and W. Schmidt. Properties of sunspot umbrae observed in cycle 24. *A&A*, 565:A52, 2014. doi: 10.1051/0004-6361/201321119. URL <https://doi.org/10.1051/0004-6361/201321119>.
- G. Kopp and D. Rabin. A relation between magnetic field strength and temperature in sunspots. *Solar Physics*, 141:253–265, Oct. 1992. doi: 10.1007/BF00155178.
- K. Langhans, G. B. Scharmer, D. Kiselman, M. G. Löfdahl, and T. E. Berger. Inclination of magnetic fields and flows in sunspot penumbrae. *Astronomy & Astrophysics*, 436(3): 1087–1101, June 2005. doi: 10.1051/0004-6361:20052678.
- K. Langhans, G. B. Scharmer, D. Kiselman, and M. G. Löfdahl. Observations of dark-cored filaments in sunspot penumbrae. *Astronomy & Astrophysics*, 464(2):763–774, Mar. 2007. doi: 10.1051/0004-6361:20065215.
- J. Leñero-Bardallo, J. Fernández-Berni, and A. Rodríguez-Vázquez. Review of adcs for imaging. *Proceedings of SPIE - The International Society for Optical Engineering*, 9022, 02 2014. doi: 10.1117/12.2041682.
- K. Leka and A. Skumanich. The evolution of pores and the development of penumbrae. *The Astrophysical Journal*, 507(1):454–469, nov 1998. doi: 10.1086/306297. URL <https://doi.org/10.1086/306297>.
- E.-K. Lim, V. Yurchyshyn, P. Goode, and K.-S. Cho. Observation of a Non-radial Penumbra in a Flux Emerging Region under Chromospheric Canopy Fields. *Astrophysical Journal Letters*, 769(1):L18, May 2013. doi: 10.1088/2041-8205/769/1/L18.

- P. Lindner, R. Schlichenmaier, and N. Bello González. Characterization of the umbra-penumbra boundary by the vertical component of the magnetic field – Analysis of ground-based data from the GREGOR Infrared Spectrograph. *arXiv e-prints*, art. arXiv:2004.09956, Apr. 2020.
- B. W. Lites and A. Skumanich. Stokes Profile Analysis and Vector Magnetic Fields. V. The Magnetic Field Structure of Large Sunspots Observed with Stokes II. *Astrophysical Journal*, 348:747, Jan. 1990. doi: 10.1086/168284.
- B. W. Lites, D. F. Elmore, P. Seagraves, and A. P. Skumanich. Stokes Profile Analysis and Vector Magnetic Fields. VI. Fine Scale Structure of a Sunspot. *Astrophysical Journal*, 418:928, Dec. 1993. doi: 10.1086/173450.
- W. Livingston. Sunspots Observed to Physically Weaken in 2000-2001. *Solar Physics*, 207:41–45, May 2002. doi: 10.1023/A:1015555000456.
- B. Löptien, A. Lagg, M. van Noort, and S. K. Solanki. No universal connection between the vertical magnetic field and the umbra-penumbra boundary in sunspots. *Astronomy & Astrophysics*, 639:A106, July 2020. doi: 10.1051/0004-6361/202037974.
- B. Löptien, A. Lagg, M. van Noort, and S. K. Solanki. Connecting the wilson depression to the magnetic field of sunspots. *Astronomy & Astrophysics*, 635:A202, Mar 2020. ISSN 1432-0746. doi: 10.1051/0004-6361/201936975. URL <http://dx.doi.org/10.1051/0004-6361/201936975>.
- B. Löptien, A. Lagg, M. van Noort, and S. K. Solanki. Similarities of magnetoconvection in the umbra and in the penumbra of sunspots. *Astronomy & Astrophysics*, 655:A61, Nov. 2021. doi: 10.1051/0004-6361/202141440.
- S. Mathew, V. Martínez-Pillet, S. Solanki, and N. Krivova. Properties of sunspots in cycle 23: I. dependence of brightness on sunspot size and cycle phase. *Astronomy and Astrophysics*, 465, 01 2007. doi: 10.1051/0004-6361:20066356.
- S. K. Mathew, A. Lagg, S. K. Solanki, M. Collados, J. M. Borrero, S. Berdyugina, N. Krupp, J. Woch, and C. Frutiger. Three dimensional structure of a regular sunspot from the inversion of IR Stokes profiles. *Astronomy & Astrophysics*, 410:695–710, Nov. 2003. doi: 10.1051/0004-6361:20031282.
- M. R. McPherson, H. Lin, and J. R. Kuhn. Infrared Array Measurements of Sunspot Magnetic Fields. *Solar Physics*, 139(2):255–266, June 1992. doi: 10.1007/BF00159152.
- E. N. Parker. Sunspots and the physics of magnetic flux tubes. IX. Umbral dots and longitudinal overstability. *Astrophysical Journal*, 234:333–347, Nov. 1979. doi: 10.1086/157501.
- W. H. Press, S. A. Teukolsky, W. T. Vetterling, and B. P. Flannery. *Numerical Recipes: The Art of Scientific Computing*. Cambridge University Press, 3 edition, 2007.
- M. Rempel. Penumbra Fine Structure and Driving Mechanisms of Large-scale Flows in Simulated Sunspots. *Astrophysical Journal*, 729:5, Mar. 2011. doi: 10.1088/0004-637X/729/1/5.

- M. Rempel and M. C. M. Cheung. Numerical Simulations of Active Region Scale Flux Emergence: From Spot Formation to Decay. *Astrophysical Journal*, 785:90, Apr. 2014. doi: 10.1088/0004-637X/785/2/90.
- M. Rempel, M. Schüssler, and M. Knölker. Radiative Magnetohydrodynamic Simulation of Sunspot Structure. *Astrophysical Journal*, 691:640–649, Jan. 2009. doi: 10.1088/0004-637X/691/1/640.
- R. Rezaei, C. Beck, and W. Schmidt. Variation in sunspot properties between 1999 and 2011 as observed with the Tenerife Infrared Polarimeter. *Astronomy & Astrophysics*, 541:A60, May 2012. doi: 10.1051/0004-6361/201118635.
- R. Rezaei, C. Beck, A. Lagg, J. M. Borrero, W. Schmidt, and M. Collados. Variation in sunspot properties between 1999 and 2014. *Astronomy & Astrophysics*, 578:A43, June 2015. doi: 10.1051/0004-6361/201425557.
- T. L. Riethmüller and S. K. Solanki. The potential of many-line inversions of photospheric spectropolarimetric data in the visible and near uv. *Astronomy & Astrophysics*, 2019.
- T. Rimmele. On the Relation between Umbral Dots, Dark-cored Filaments, and Light Bridges. *Astrophysical Journal*, 672(1):684–695, Jan. 2008. doi: 10.1086/523702.
- A. M. Rucklidge, H. U. Schmidt, and N. O. Weiss. The abrupt development of penumbrae in sunspots. *Monthly Notices of the RAS*, 273(2):491–498, Mar. 1995. doi: 10.1093/mnras/273.2.491.
- I. Ruedi, S. K. Solanki, C. U. Keller, and C. Frutiger. Infrared lines as probes of solar magnetic features. XIV. Ti i and the cool components of sunspots. *Astronomy & Astrophysics*, 338:1089–1101, Oct. 1998.
- M. Sánchez Cuberes, K. G. Puschmann, and E. Wiehr. Spectropolarimetry of a sunspot at disk centre. *Astronomy & Astrophysics*, 440(1):345–356, Sept. 2005. doi: 10.1051/0004-6361:20042042.
- S. Saranathan, M. van Noort, and S. K. Solanki. Correction of atmospheric stray light in restored slit spectra. *Astronomy & Astrophysics*, 653:A17, Sept. 2021. doi: 10.1051/0004-6361/201937100.
- T. A. Schad. On the Collective Magnetic Field Strength and Vector Structure of Dark Umbral Cores Measured by the Hinode Spectropolarimeter. *Solar Physics*, 289:1477–1498, May 2014. doi: 10.1007/s11207-013-0412-7.
- G. B. Scharmer, B. V. Gudiksen, D. Kiselman, M. G. Löfdahl, and L. H. M. Rouppe van der Voort. Dark cores in sunspot penumbral filaments. *Nature*, 420(6912):151–153, Nov. 2002. doi: 10.1038/nature01173.
- G. B. Scharmer, Å. Nordlund, and T. Heinemann. Convection and the Origin of Evershed Flows in Sunspot Penumbrae. *Astrophysical Journal Letters*, 677:L149, Apr. 2008. doi: 10.1086/587982.

- R. Schlichenmaier, N. Bello González, R. Rezaei, and T. Waldmann. The role of emerging bipoles in the formation of a sunspot penumbra. *Astronomische Nachrichten*, 331(6):563–566, 2010. doi: <https://doi.org/10.1002/asna.201011372>. URL <https://onlinelibrary.wiley.com/doi/abs/10.1002/asna.201011372>.
- M. Schmassmann, R. Schlichenmaier, and N. Bello González. Magnetic properties of a long-lived sunspot - vertical magnetic field at the umbral boundary. *A&A*, 620:A104, 2018. doi: [10.1051/0004-6361/201833441](https://doi.org/10.1051/0004-6361/201833441). URL <https://doi.org/10.1051/0004-6361/201833441>.
- M. Schüssler and A. Vögler. Magnetoconvection in a Sunspot Umbra. *Astrophysical Journal Letters*, 641(1):L73–L76, Apr. 2006. doi: [10.1086/503772](https://doi.org/10.1086/503772).
- M. F. Snoeij, A. J. Theuwissen, J. H. Huijsing, and K. A. A. Makinwa. Power and area efficient column-parallel adc architectures for cmos image sensors. In *SENSORS, 2007 IEEE*, pages 523–526, 2007a. doi: [10.1109/ICSENS.2007.4388451](https://doi.org/10.1109/ICSENS.2007.4388451).
- M. F. Snoeij, A. J. P. Theuwissen, K. A. A. Makinwa, and J. H. Huijsing. Multiple-ramp column-parallel adc architectures for cmos image sensors. *IEEE Journal of Solid-State Circuits*, 42(12):2968–2977, 2007b. doi: [10.1109/JSSC.2007.908720](https://doi.org/10.1109/JSSC.2007.908720).
- S. K. Solanki. *The Photospheric Layers of Solar Magnetic Flux Tubes*. PhD thesis, Max-Planck-Institute for Solar System Research, Lindau, Oct. 1987.
- S. K. Solanki. Sunspots: An overview. *Astronomy & Astrophysics Review*, 11(2-3): 153–286, Jan. 2003. doi: [10.1007/s00159-003-0018-4](https://doi.org/10.1007/s00159-003-0018-4).
- S. K. Solanki and C. A. P. Montavon. Uncombed fields as the source of the broad-band circular polarization of sunspots. *Astronomy & Astrophysics*, 275:283, Aug. 1993.
- S. K. Solanki, I. Ruedi, and W. Livingston. Infrared lines as probes of solar magnetic features. V - The magnetic structure of a simple sunspot and its canopy. *Astronomy & Astrophysics*, 263(1-2):339–350, Sept. 1992.
- S. K. Solanki, C. A. P. Montavon, and W. Livingston. Infrared lines as probes of solar magnetic features. 7: On the nature of the Evershed effect in sunspots. *Astronomy & Astrophysics*, 283(1):221–231, Mar. 1994.
- S. K. Solanki, P. Barthol, S. Danilovic, A. Feller, A. Gandorfer, J. Hirzberger, T. L. Riethmüller, M. Schüssler, J. A. Bonet, V. Martínez Pillet, J. C. del Toro Iniesta, V. Domingo, J. Palacios, M. Knölker, N. Bello González, T. Berkefeld, M. Franz, W. Schmidt, and A. M. Title. SUNRISE: Instrument, Mission, Data, and First Results. *Astrophysical Journal Letters*, 723(2):L127–L133, Nov. 2010. doi: [10.1088/2041-8205/723/2/L127](https://doi.org/10.1088/2041-8205/723/2/L127).
- S. K. Solanki, T. L. Riethmüller, P. Barthol, S. Danilovic, W. Deutsch, H. P. Doerr, A. Feller, A. Gandorfer, D. Germerott, L. Gizon, B. Grauf, K. Heerlein, J. Hirzberger, M. Kolleck, A. Lagg, R. Meller, G. Tomasch, M. van Noort, J. Blanco Rodríguez, J. L. Gasent Blesa, M. Balaguer Jiménez, J. C. Del Toro Iniesta, A. C. López Jiménez, D. Orozco Suarez, T. Berkefeld, C. Halbgewachs, W. Schmidt, A. Álvarez-Herrero, L. Sabau-Graziati, I. Pérez Grande, V. Martínez Pillet, G. Card, R. Centeno, M. Knölker,

- and A. Lecinski. The Second Flight of the Sunrise Balloon-borne Solar Observatory: Overview of Instrument Updates, the Flight, the Data, and First Results. *Astrophysical Journal Suppl. Ser.*, 229(1):2, Mar. 2017. doi: 10.3847/1538-4365/229/1/2.
- M. Soman, K. Stefanov, D. Weatherill, A. Holland, J. Gow, and M. Leese. Non-linear responsivity characterisation of a cmos active pixel sensor for high resolution imaging of the jovian system. *Journal of Instrumentation*, 10:C02012–C02012, 02 2015. doi: 10.1088/1748-0221/10/02/C02012.
- A. M. Title, Z. A. Frank, R. A. Shine, T. D. Tarbell, K. P. Topka, G. Scharmer, and W. Schmidt. On the magnetic and velocity field geometry of simple sunspots. *Astrophysical Journal*, 403:780–796, Feb. 1993. doi: 10.1086/172249.
- S. K. Tiwari, M. van Noort, A. Lagg, and S. K. Solanki. Structure of sunspot penumbral filaments: a remarkable uniformity of properties. *A&A*, 557:A25, 2013. doi: 10.1051/0004-6361/201321391. URL <https://doi.org/10.1051/0004-6361/201321391>.
- S. K. Tiwari, M. van Noort, S. K. Solanki, and A. Lagg. Depth-dependent global properties of a sunspot observed by hinode using the solar optical telescope/spectropolarimeter. *A&A*, 583:A119, 2015. doi: 10.1051/0004-6361/201526224. URL <https://doi.org/10.1051/0004-6361/201526224>.
- M. van Noort. Spatially coupled inversion of spectro-polarimetric image data - i. method and first results. *A&A*, 548:A5, 2012. doi: 10.1051/0004-6361/201220220. URL <https://doi.org/10.1051/0004-6361/201220220>.
- M. van Noort, L. Voort, and M. Löfdahl. Solar image restoration by use of multi-frame blind de-convolution with multiple objects and phase diversity. *Solar Physics*, 228: 191–215, 05 2005. doi: 10.1007/s11207-005-5782-z.
- F. Wang. *Linearity Research of A CMOS Image Sensor*. PhD thesis, Delft University of Technology, 2018.
- F. Wang and A. J. Theuwissen. Linearity analysis of a cmos image sensor. In *Electronic Imaging*, Electronic Imaging, pages 84–90. Society for Imaging Science and Technology, 2017. doi: 10.2352/issn.2470-1173.2017.11.imse-191. 2017 IS&T International Symposium on Electronic Imaging ; Conference date: 31-01-2017 Through 02-02-2017.
- F. T. Watson, M. J. Penn, and W. Livingston. A Multi-instrument Analysis of Sunspot Umbrae. *Astrophysical Journal*, 787:22, May 2014. doi: 10.1088/0004-637X/787/1/22.
- C. Westendorp Plaza, J. C. del Toro Iniesta, B. Ruiz Cobo, V. Martínez Pillet, B. W. Lites, and A. Skumanich. Evidence for a downward mass flux in the penumbral region of a sunspot. *Nature*, 389:47, Sept. 1997. doi: 10.1038/37933.
- C. Westendorp Plaza, J. C. del Toro Iniesta, B. Ruiz Cobo, and V. Martínez Pillet. Optical Tomography of a Sunspot. III. Velocity Stratification and the Evershed Effect. *Astrophysical Journal*, 547(2):1148–1158, Feb. 2001a. doi: 10.1086/318377.

- C. Westendorp Plaza, J. C. del Toro Iniesta, B. Ruiz Cobo, V. Martínez Pillet, B. W. Lites, and A. Skumanich. Optical Tomography of a Sunspot. II. Vector Magnetic Field and Temperature Stratification. *Astrophysical Journal*, 547(2):1130–1147, Feb. 2001b. doi: 10.1086/318376.
- E. Wiehr. The origin of the Evershed asymmetry. *Astronomy & Astrophysics*, 298:L17, June 1995.
- V. Zakharov, J. Hirzberger, T. L. Riethmüller, S. K. Solanki, and P. Kobel. Evidence of convective rolls in a sunspot penumbra. *Astronomy & Astrophysics*, 488(2):L17–L20, Sept. 2008. doi: 10.1051/0004-6361:200810266.
- F. Zeuner, R. Manso Sainz, A. Feller, M. van Noort, S. K. Solanki, F. A. Iglesias, K. Reardon, and V. Martínez Pillet. Solar Disk Center Shows Scattering Polarization in the Sr I 4607 Å Line. *Astrophysical Journal Letters*, 893(2):L44, Apr. 2020. doi: 10.3847/2041-8213/ab86b8.

Index

- ADC, 21, 22, 26, 28, 29
 - Analogue to Digital Converter, 20
 - Non-linearity, 25
- Additive targets, 30–32, 61
- APS, 21
 - Active Pixel Sensors, 21
- Banding, 55, 76
- Calibration region, 30–35, 41, 43, 48, 61, 109
- Camera non-linearity, 12, 15
- Camera non-uniformity, 12
- CCDs, 22, 25
 - Charge-Coupled Devices, 19
- CMOS, 22, 36, 48
- Colour sensors, 49
- Control region, 30, 33–35, 41, 43, 48, 109
- Cross-talk, 1, 2, 29, 38
- Deductive targets, 30, 31, 33, 34, 41, 61
- Evershed flow, 81, 82
- Exposure time, 22, 43
 - Integration time, 20
- Filtergraphs, 12
- Fixed Pattern noise, 21, 26, 28
- Flat illumination, 26, 36
- Gain non-linearity, 25
- Gradient illumination, 38
- Independent Illumination Setup, 41
- Integral Field Solutions, 13
- Integrating sphere, 43, 109
- Light level non-linearity, 14
- Light level scale, Intensity scale, 48
- Mask, 33, 36, 38
- Monochrome sensors, 49
- Penumbra, 4, 81–84
- Penumbral filaments, 6, 81
- Photon noise, shot noise, 15, 23, 24, 27
- Photons, 43, 44
- Pixel cross-talk, 24, 25, 41
- Pixel non-linearity, 12, 14, 24
- Pixel reset noise, 27
- Polarimetry, 2, 15
- Polarization, 1, 9, 11
- PPS
 - Passive Pixel Sensors, 19, 20
- Preliminary setup, 41
- Quantisation noise, 23, 27
- row-average, 30–35, 37–39, 41
- Scene-dependent effect, 25, 26, 30, 38, 39, 41
- Shielded pixels, 36, 38, 41
- Shutter, 22
 - Global, 22
 - Physical/Mechanical, 20, 22
 - Rolling, 22, 38
- Siblings, 29–35, 37, 38, 41
 - Number of simultaneous conversions, 26, 41
- Spectrometry, 15
- Spectrographs, 12
- Spines, 5, 81
- Stokes vector, 9–11
- Sunspot, 1, 4, 81, 82, 84
- Thermal flicker, 27, 41
- Timing jitter, 47
- Triangular target, 36–38
- Umbra, 4, 81, 83, 86
- Uniform illumination, 37

Acknowledgements

I want to acknowledge the support of the International Max Planck Research School for Solar System Science (IMPRS) and the Max Planck Institute for Solar System Research (MPS) during my PhD, allowing me to work on a few exciting projects.

Without the support of Prof. Karl-Heinz Glaßmeier, it would not have been easy to enrol in a University. Hence I am thankful that he was willing to accept me as his student and guide me through all the complex tasks of the University. He helped me with the thesis and completed the additional requirements of the University by giving me the reading material and conducting exams for the course work needed.

Most of this work on cameras has been the brainchild of Dr. Michiel van Noort and only presented here by me. This suffices to say that I would have been lost without his critical support. Guiding me through my day-to-day tasks would have been difficult for anyone; however, Dr. Tino Riethmüller was always willing to help as he was my primary supervisor. During all this time, Dr. Hans-Peter Doerr was a personal tour guide for the whole process. Whenever I had problems of any kind, I would trouble him. Dr. Michiel van Noort and Dr. Tino Riethmüller must have felt some relief after introducing me to him.

Dr. Alex Feller was more than happy to allow and support me in working on the cameras for the SUNRISE 3 project.

Prof. Sami K.Solanki was always concerned about me completing my thesis and making progress in it. He provided me with a secondary project when my first one came to stand still and helped me keep a constant pace by checking up on me regularly. Dr. Björn Loeptien was my primary contact for this project. I guess Prof. Sami Solanki would have been more worried about my progress without him.

Only with the help of all the people above could I complete my thesis; they read through it, corrected it multiple times, and helped me whenever I was stuck. I am glad that they were there to help me.

Curriculum vitae

Personal information

Name: Kamal Sant

Year of birth: 1994

Email: santspacekamal@gmail.com

Projects and Work Experience

Aug 2017-Sep 2022: Non-linearity calibration of CMOS Imaging sensors, with Dr. Michiel van Noort,(MPS, Goettingen) (vannort@mps.mpg.de, +49 551 384 979 423)

May-Nov 2016: Photonic Crystal Biosensors, with Prof. Thomas F. Krauss (University of York, UK), (thomas.krauss@york.ac.uk)

Jan-May 2016: Linear and Non-linear Spectroscopic techniques, with Prof. Achanta Venu Gopal (TIFR, India)

Aug-Dec 2015: Introduction to Path Integral techniques and studying Scattering processes with Dr. Ameeya Bhagwat (UM-DAE CEBS, India), (ameeyabhagwat@gmail.com)

Education

2017-2022: PhD Student at the MPI for Solar System Research and Technische Universität Braunschweig

2012-2017: Master of Science (Five Year Integrated Degree Course in Physics) at the University of Mumbai-Department of Atomic Energy, Centre for Excellence in Basic Sciences (UM-DAE CEBS),

Master Thesis: The Chirped Grating Biosensor | Advisor: Prof. Thomas Krauss (York University)

Conferences and Workshops Attended

2019: 9th Solar Polarization Workshop at MPI for Solar System Research

2018: GREGOR Meeting

2017: Rocks and Stars at Max Planck Institute for Solar System Research

2016: PECS 12 at York (Poster)